Non-uniformity Correction and Calibration of Hyperspectral Image Data

by

Juan Enrique Castorena-Martinez

A Thesis submitted to the Faculty of Graduate Studies of

The University of Manitoba

in partial fulfilment of the requirements of the degree of

Master of Science

Department of Biosystems Engineering

University of Manitoba

Winnipeg, Manitoba, Canada

THE UNIVERSITY OF MANITOBA

FACULTY OF GRADUATE STUDIES

*****

COPYRIGHT PERMISSION

Non-uniformity Correction and Calibration of Hyperspectral Image Data

By

Juan Enrique Castorena-Martinez

A Thesis/Practicum submitted to the Faculty of Graduate Studies of The University of Manitoba in partial fulfillment of the requirement of the degree

Of

Master of Science

Abstract

Near infrared (NIR) hyperspectral imaging (HSI) is a powerful non-destructive tool for the chemical analysis of heterogeneous samples. The advantages of the technique over others rely on its speed and cost. However, one of the main disadvantages of NIR HSI is that, the technique suffers from problems related to the instrumentation. In general, the imaging instrumentation is affected by the spatial nonuniform response in the focal plane array (FPA), the spectral variance, the time drift and the dark current noise. Another problem is that the camera needs to be calibrated into units that are more meaningful to the analyst.

The scope of this research is limited to signal processing techniques for the correction and calibration of reflectance NIR HSI systems consisting electronically tunable wavelength filters. The thesis presents a method where parameter estimates for the response and calibration of the system are obtained using a linear model. The parameters of the model are calculated using a calibration reference method that considers the time drift in the system. Sensors are classified using the *k*-means algorithm into sensitive and insensitive. The results show that the parameters of the linear response and calibration model considering time drift are accurate estimates of the actual response and calibration functions. The performance of the method was assessed using the root mean squared error on a per sensor and wavelength basis. The method used is better than those previously developed in the literature for this type of systems.

Acknowledgments

The author is especially thankful to the University of Manitoba for providing a valuable fellowship for the financial support of the researcher. The author is also especially thankful to Dr. Jason Morrison and Dr. Jitendra Paliwal for providing extra assistance for funding, and for providing valuable time and technical assistance in the development of the research.

Special appreciations to Dr. Gabriel Thomas for providing valuable advice, and to Dr. Mark Hewko for suggesting significant improvements on writing this thesis, to Dr. Flores-Tapia for providing technical tips for the research, to Chandra Singh, Mahesh Sivakumar and Wenbo Wang for providing information regarding the system, and finally to Nathan Kesler for providing the document template.

Dedication

To mom and dad

Contents

List of Figures

List of Symbols

u	Continuous Cartesian coordinate in horizontal direction
v	Continuous Cartesian coordinate in vertical direction
λ	Wavelength in nm.
b	Wavelength band
$L_\lambda(u,v)$	Scene radiance at the object plane
N	Optics *f-number*
$\tau_o(\lambda)$	Optics transmittance of the lens
π	Pi (3.1416)
$E_\lambda(u,v)$	Irradiance at the focal plane array
λ_{min}	Filter parameter: center wavelength – FWHM/2
λ_{max}	Filter parameter: center wavelength + FWHM/2
α_{min}	Lower boundary for spatial extent of the PSF in the horizontal direction
α_{max}	Upper boundary for spatial extent of the PSF in the horizontal direction
β_{min}	Lower boundary for the spatial extent of the PSF in the vertical direction
β_{max}	Upper boundary for the spatial extent of the PSF in the vertical direction
$*$	Two dimensional spatial convolution
$R_b(\lambda)$	Spectral response of the optics and filter
$r_\lambda(u,v)$	Detector or sensor responsivity

$PSF_{net}(u,v)$	Overall point spread function
$PSF_{opt}(u,v)$	Point spread function introduced by the system optics
$PSF_{det}(u,v)$	Point spread function introduced by detectors or sensors
p	Width of the optics PSF in the horizontal direction
q	Width of the optics PSF in the vertical direction
e^x	Exponential function
rect()	Rectangle function
ps	Detector or sensor size
t_0	Acquisition starting time
t_e	Exposure time or integration time
t	Time instance
τ	Time integrated interval instance
$I_\lambda(u,v)$	Illumination source output radiance
$\eta^t(u,v)$	Dark current noise
g_b	Electronics gain
$offset_b$	Electronics offset
int[]	Conversion to nearest integer function
i	Discrete spatial coordinate in horizontal direction
j	Discrete spatial coordinate in vertical direction
k	Discrete wavelength band
y_{ijk}^{τ}	System output in A/D counts
$\boldsymbol{y_{ijk}}$	System output vector in A/D counts
x_{ijk}	Input in percent reflectance

$\boldsymbol{x_{ijk}}$	Input vector in percent reflectance
$gain_{ijk}$	First order system response parameter (Forward relationship)
$bias_{ijk}^{\tau}$	Offset system response parameter (Forward relationship)
E{}	Expected value
$\boldsymbol{e_{ijk}}$	Vector of errors or residuals between observations and fitted values
$\widehat{gain}_{ijk}$	First order system response model parameter estimate (Fwd relationship)
$\widehat{bias}_{ijk}$	Offset system response model parameter estimate (Forward relationship)
$\hat{a}_{ijk}$	First order coefficient estimate for calibration model (Inverse relationship)
$\hat{b}_{ijk}$	Offset coefficient estimate for calibration model (Inverse relationship)
$\hat{c}_{ijk}$	Quadratic coefficient estimate for calibration model (Inv. relationship)
s	Reference standard nominal reflectance factor
l	Index for measurement sample or repetition
x_{ijk}^{s}	Input reflectance of standard s in percent reflectance
y_{ijk}^{s}	Output reflectance of standard s in A/D counts
SSE	Sum of squared errors or residuals
PRESS	Prediction sum of squared errors
MSE	Mean squared sum of squared errors
MSR	Mean regression sum of squares
$\boldsymbol{\omega}$	Pattern vector of slope coefficients

Chapter 1

Introduction

Near infrared (NIR) hyperspectral imaging (HSI) has established itself as a powerful tool for the chemical analysis of heterogeneous samples. The technique has gained widespread acceptance in a variety of applications such as food and agrochemical quality and safety inspection (Wang and Paliwal 2007), pharmaceutics and medicine (Ciurczak and Drennen 2002), textile production, combustion research, etc. The NIR HSI technique offers many benefits such as increased speed, cost and applicability over conventional techniques. Moreover, the technique enables the non-invasive analysis of multiple chemical constituents simultaneously. Unfortunately, the technique is not free from problems; some of the typical issues in the technique are related to the instrumentation. In general, the imaging instrumentation is affected by the spatial non-uniform response of the focal plane array (FPA) including defective sensors and sensors limited by the aperture, the spectral variance, the time drift and the dark current noise. Another problem is that the output of the instrumentation is in terms of A/D counts. This measure needs to be calibrated into units more meaningful to the analyst.

1.1 Basics of NIR HSI

The fundamental concept behind the NIR HSI technique dates back to the early discovery of vibrational spectroscopy that each molecular species provides a unique vibrational spectral fingerprint. Later on, this concept was developed by recognizing that smaller shifts within the expected group frequency represents detailed information about the chemical structure and environment of a molecule within the group. Currently, there are an extensive number of library sources containing the characteristic spectral fingerprints for many compounds. For example, the ASTER spectral library v1.2 provides a collection of over 2300 spectra of a wide variety of materials covering the wavelength range 0.4 – 15.4 μm (Baldridge et al. 2008).

The characteristic molecular signatures occurring in the NIR spectral region gained interest due to the development of both low cost instrumentation with high signal to noise ratio (SNR) and chemometrics. The NIR light spectrum covers the wavelength interval of 750 to 2500 nm in the electromagnetic spectrum. The energy of light in this region consists of overtones and combination bands of the fundamental molecular absorptions that occur in the mid-infrared region (Mark and Workman 2003). The molecular bonds with predominant overtone vibrations in this region include methyl C-H, methylene C-H, methoxy C-H, aromatic C-H, O-H, carbonyl associated C-H, N-H from primary, secondary and tertiary amines and N-H from amine salts stretching vibrations. These bonds form the basis for many important components such as proteins, carbohydrates, fats, water, etc.

A typical sampling method used to capture the spectral content of materials is HSI or spectroscopic imaging which combines both conventional imaging and spectroscopy. The technique is used to convert radiance (reflected and/or emitted) into a HS cube of digital images at contiguous spectral bands. Each of these images represents the spatial distribution of radiance at a wavelength band. While HSI information can be used to extract the chemical content of a sample (Geladi 2003); the technique has been widely used for remote sensing. Fortunately, reduction of instrument size has made this technique available for laboratory use.

The advent of chemometrics enhanced the capability to extract the chemical constituents of a sample based on a sample's spectra. Typically, chemical extraction can be a problem because the data collected is correlated with the instrument response and the physical and chemical characteristics of the sample. Chemometrics uses multivariate methods of data analysis to extract the sample's main chemical constituents (Mark and Workman 2007). In general, the technique is based on using mathematics, statistics and computer science for finding correlations between the raw spectra and known molecular fingerprints for sample characterization.

1.2 NIR HSI instrumentation

In general, the instrumentation used to capture the chemical information of an object is composed of an illumination source, filter, optics and a focal plane array (FPA) of sensors. There are a wide variety of component options one can choose depending on the ap-

plication requirements. This section presents a brief description of the main components of a NIR HSI system and some typical system configurations.

The illumination source serves as a source of NIR electromagnetic radiation. The purpose for using an illumination source in the system is to increase the overtone vibration of the molecules in the object under study. Typically, every object at room temperature emits light in the NIR region. However, the emission is so low that it would require extremely powerful sensors for detecting the reflected light. Sensors of this kind are not feasible because of cost and availability. Thus, to increase the emission of NIR light caused by molecular vibration overtones, the illumination source is often used as an excitation source. Typical NIR illumination sources are divided into two categories, broadband (thermal) sources and narrow band (non-thermal) sources (Osborne et al. 1993). Broadband sources are commonly used in HSI systems. These sources produce radiation spanning a continuous spectral region. Tungsten halogen lamps are the most commonly used broadband illumination sources because of their extended lifetime and stability. (McClure 2001). Narrow band sources, on the other hand, emit radiation within a narrow spectral band. The advantages of these sources include increased power efficiency and specific emission wavelengths. Typical sources in this category are light emitting diodes, laser diodes and lasers.

The filters in the system are used to separate polychromatic light into a set of narrow bands. The two main methods used to separate polychromatic light are optical interference filters and electronically tunable filters. Optical interference filters separate light based on specific transmission characteristics of the material and design. These are installed in a filter wheel to produce light at multiple predefined wavelengths. Common fil-

ters of this type are Fabry-Perot dielectric filters (O'Shea 1985). The advantages of interference filters lie in their low cost and simple design. However, they are limited by the wavelength selection wheel method. In contrast, the electronic tunable filters control the spectral transmission by applying a voltage, current or an acoustic signal (Gat 2000). The most common filters of this type are liquid crystal tunable filters (LCTFs) and acousto-optical tunable filters (AOTFs). An AOTF consists of a crystal in which broadband light is isolated into monochromatic light using radio frequency (RF) acoustic waves. In other words, a wavelength is selected as a function of the frequency RF wave applied to the crystal. In contrast, LCTF is built using a stack of polarizers and tunable retardation liquid crystal plates. The spectral resolution or pass band of the filter is typically in the order of several nanometers. This is sufficient for most reflectance/transmittance analysis and even Raman measurements (Gat 2000). Some of the advantages of LCTF over its counterparts is that it is compact, digitally controlled, has no moving parts and allows instant access to random wavelengths. These features establish it as a powerful device for the quantitative and qualitative analysis of samples.

The goal of the lens is to converge or diverge the transmitted light. The optical characteristics of a lens can be modified by altering the material, surface coating and design (Pedrotti et al. 2007). Silica glass has very high homogeneity and 90 percent or better transmission in the visible and NIR bands making it ideal for lenses suited for these spectral ranges (Wilson 2005). Silica glass lenses designed for visible light are often used for NIR imaging by applying surface coatings to minimize reflection of the visible light. This process often reduces the transmission of NIR light at longer wavelength bands. Thus, a lens designed for visible light should contain as few surface coating layers as possible

when used in the NIR region. The design of the lens deals with the shape and number of pieces. Often, a combination of three or more pieces is used to minimize various image aberrations (Ren 2000). However, the optimal combination for one wavelength does not guarantee the same performance at other wavelengths. In general, the image quality produced by specialized NIR lenses is better than standard and high quality lenses designed for visible light (Alexay 2008).

A detector or sensor of the photodetector is a device that measures the light energy incident at the detector surface to convert it into electrical energy. Detectors are available for the full electromagnetic spectrum. However, each detector is designed specifically to detect certain portions of the spectrum. Indium-Gallium-Arsenide (InGaAs) is a preferable choice of material for detecting NIR light ranging from 1000 to 1700 nm (Olsen and Ban 1987). This is because of the characteristic property of this material alloy to absorb light in this spectral range and its low dark current noise. Another factor that has made InGaAs the detector of choice for NIR imaging is the maturity of the fabrication technology. The detector materials used for the shorter 700 to 1000 nm wavelengths are silicon based materials (Rogalski 2003). The bulk of devices in the silicon market are charge-coupled devices (CCDs). CCD technology has achieved the largest size formats with numbers approaching 10^8 sensors (Norton 2003). Lead sulphide (PbS) materials are common for the longer 1000 to 1700 nm wavelengths. The advantages of this material are mainly its cost.

Detectors are typically configured into arrays when imaging applications are intended. These are more often known as focal plane array (FPA) or staring arrays. The most common configurations are: 320 × 240, 640 × 480 and 640 × 512 detector arrays.

However, for CCDs configurations of up to 1024 × 1024, 2048 × 2048 and 4080 × 4080 have been achieved.

Currently, two approaches exist to obtain HSI data: a time resolved spatial data acquisition or a time resolved wavelength data acquisition. In time resolved spatial data acquisition, a full spectrum is obtained from a subspace of the object. The whole object space can be obtained using a point-by-point spectral scan in a spatial grid pattern (i.e. as with Raman imaging) or a line-by-line scan (i.e., pushbroom method). In the latter method, narrow line scans are imaged into a row of detectors within the FPA. Information across the whole object space can be readily obtained by moving the sample, spectrograph or camera using a controlled motor. The collection of spectral lines generates a data cube containing information about the full wavelength range and object space. For time resolved wavelength acquisition, an entire spatial image of both dimensions is collected sequentially at single wavelengths. The collection of images of successive wavelengths generates a data cube. With this method images at specific discrete wavelength bands can be obtained using a filter. Common filters for this acquisition approach are interference filters such as AOTF and LCTF.

1.3 Instrumentation problems

This thesis addresses some of the issues encountered by NIR HSI sampling instrumentation. The main problems related to the instrumentation arise due to the spatial non-uniform response of the system (Schulz and Caldwell 1995), the spectral variance (Geladi et al. 2004) and the time drift in the sensors within the FPA. Also, some sensors within

the FPA can be defective showing saturation or no response at all. Identification of these types of sensors and differences between sensor response (i.e. sensors limited by the aperture) as a function of location and spectra is desirable for proper sample analysis. These problems together with the fact that the raw data obtained from the system does not look as real spectra need to be resolved before using the data for chemical analysis (Mark and Workman 2003).

Geladi et al. (2004) proposed three models for the calibration and correction of some of the problems in NIR HSI systems. These are one-point, linear and quadratic calibrations. The parameters of the models are obtained using HS images of reflectance standards of known properties. The three techniques take into account the spatial and spectral non-uniformities in the system by considering each sensor and wavelength as independent. In other words, a model is determined for each sensor and wavelength. The first problem with these techniques is that the models are not validated. Moreover, there is no time drift considered in the study. These issues reduce the reliability on the accuracy of the parameter estimates obtained for each model. Furthermore, Geladi's procedures do not take into account the effects produced by defective sensors or sensors limited by the optics in the system.

The main objective of this thesis is to develop a methodology for the calibration and correction of laboratory NIR HSI systems. This objective is subdivided into four parts. The first part deals with obtaining a model with proper validation to describe the characteristic response of the system at each spatial location and spectral wavelength. The second part is to identify the features of the defective sensors and/or sensors limited by the aperture. The third sub-objective deals with the classification of sensors based upon their

response. Finally, the calibration of the system is achieved based on the inverse of the system response. This calibration is applied only to sensors that are neither defective nor limited by the aperture of the system.

The problems in the system are treated using signal processing. The methodology consists in obtaining a linear model for the response and calibration of each sensor within the system and wavelength. Parameter estimates of the model are obtained using relationships between the characteristics of a known input and the output of the imaging system. The criterion used to obtain the estimates is the minimum sum of squared errors (SSE). The object under the lens of the camera is a set of calibration standards of known and varying radiance, and uniform physical characteristics. A reference data set containing repeated measurements of the different reflectance standards is used instead of a single reference as described in Geladi et al. (2004) to account for the time drift and noise in the system.

The classification of sensors into sensitive or insensitive regions is based on the parameters of the system response. A feature vector is constructed using the slope coefficients and classified accordingly based on the patterns of each region. The algorithm used to perform the classification is the k-means classifier with $k=2$.

Model validation is assessed in the results and analysis section using a comparison between the SSE and the prediction error sum of squares (PRESS) as described in Kutner et al. (2005). Moreover, a hierarchical F test is included in the discussion section to check whether a higher order term polynomial provides significant refinement to the model. Finally, the performance of our method is compared with others developed in the literature using the validated root mean squared error (RMSE) per sensor and wavelength, and the

average RMSE over all spatial locations classified as sensitive as a function of wavelength.

Subsequent chapters in this thesis are organized as follows: a literature review chapter, materials and methods, results and analysis, discussion and finally a conclusion chapter. In the literature review the main problems encountered in the instrumentation are reviewed. Also, mathematical model approximations of the actual response and calibration of the system are described. In materials and methods, details about the system, configuration and setup are given. Furthermore, a methodology for the calibration and correction of the system is briefly described. In the results and analysis chapter, a characterization for the system response and calibration is designed and the resulting errors from the implementation are shown. Using the parameters of this model as descriptors, a classification of sensors based upon their response is obtained to correct for any insensitivities. In the discussion, the performance and significance of our procedure is compared with those available in the literature. Finally, the conclusion summarizes the objectives accomplished in this thesis and gives suggestions for future research.

Chapter 2

Literature Review

Hyperspectral imaging is a technique used to convert radiance (reflected and/or emitted) into a HS cube of digital images at contiguous spectral bands. Here, each image represents the spatial distribution of radiance at a wavelength band. An example of a common HS image cube of I pixel rows, J pixel columns and K wavelengths is shown in figure 1. Typical HSI cubes are available in formats of $256 \times 320 \times K$, $512 \times 614 \times K$ and $640 \times 480 \times K$. Here, K is the number of sampled wavelength bands which varies depending on the spectral resolution of the system, the bandwidth and intended application. Typically, this K value is in the range of tens to hundreds of wavelengths.

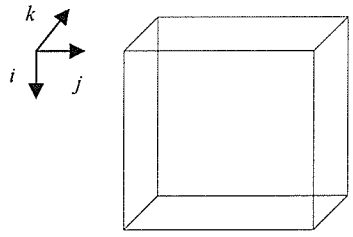

Figure 1: Hyperspectral image of I rows, J columns and K wavelengths

2.1 HSI Systems

In general, the process by which an HSI system using the wavelength tuning with filters method convert radiation into a cube of digital images can be modeled by the generic system shown in figure 2. The configured order of some of the components can be varied depending on the intended application and component specifications with no significant effect. For example, the spectral filter component can be moved after the imaging optics without changing the overall response of the system.

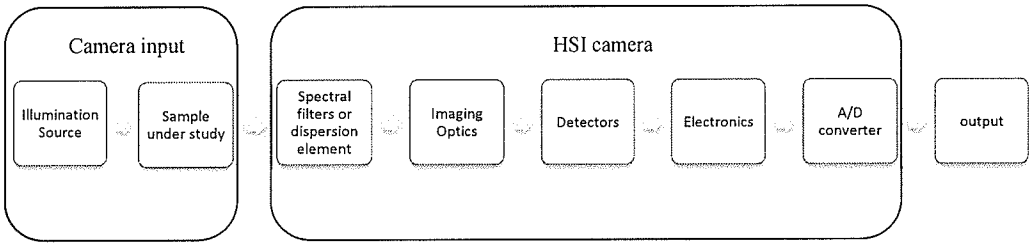

Figure 2: A generic hyperspectral imaging system

The components in figure 2 contain problems that affect the performance of the system. For example, the output of the illumination source is light that varies in spatial location, wavelength, and time. This problem results in spatial and spectral non-uniformity as well as time drift of the overall system. The spectral filters or dispersion elements and the physical characteristics of the imaging optics may present problems. For example, these components can introduce geometric distortions and blurring of the imaged scene (Gat 2000 and Ren 2003). The sensors in the camera are also, not free from problems. Typically, the response of a sensor in a FPA varies with spatial location (Schulz and Caldwell 1995), spectral band (Geladi et al. 2004) and time. Time variation of the detector's response is caused by thermal noise and the quantum efficiency of the detector. Generally,

the problems in the detector exist because of fabrication variation, detector design and the quantum nature of current carriers in semiconductor materials (Rogalski 2003).

2.2 System Response

The system response is a mathematical representation of the relation between an input and output of the system. This relationship is used to approximate the unknown effects introduced by the bulk of components conforming the system (Proakis and Manolakis 2007). The only way to interact with the system is by using its input and output terminals (i.e., the system is assumed to be a black box by the user). For HSI systems this input and output relationship needs to be established as a function of spectral wavelength, spatial location and in some situations time.

Before getting into the system response equations a few important definitions about the system parameters need to be defined. We begin with definitions for the parameters in the imaging optics block in figure 2. The most important parameters of the optics are the diameter of the aperture D and the focal length f. The aperture of the system is the physical opening that determines the cone angle of a bundle of rays that come to a focus in the image plane. In other words, the aperture limits the amount of light that reaches the image plane. The focal length is a measure of the strength to which light is focused or diffused. A system with a shorter focal length contains fewer capabilities of focusing light. The two parameters are shown in figure 3.

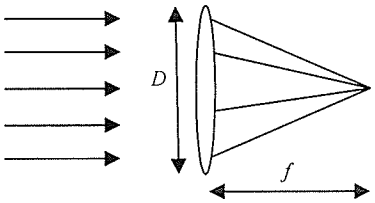

Figure 3: Optical lens: Aperture and focal length

For HSI systems the spectral transmittance of the optics is also important. The optical transmittance determines the portion of rays that makes it through the imaging optics as a function of wavelength. Another important definition is the bandwidth. The bandwidth of a system is defined as the difference between the upper and lower cutoff wavelengths. Here, a wavelength corresponds to the distance between repeating units of a propagating light wave of a given frequency.

All the equations in the following subsections are obtained from Schowengerdt (1997). The author explains the response for a remote sensing HSI system. However, the equations explained by the author also apply to the laboratory based NIR HSI systems. The reason is that the components used in the instrumentation for remote sensing imaging are of similar characteristics as the components used in laboratory NIR HSI systems. The only modification added here is to account for the spatial non-uniform response of sensors within the FPA. The equations can also be found in Perry and Dereniak (1993) with different variable notation for infrared imaging systems. In Perry and Dereniak's study, the infrared (IR) source, sensor constants and spatial non-uniformities in the FPA imager are considered.

2.2.1 Spectral Response

The spectral response describes the sensitivity of the system to radiation of different wavelengths. For systems using the components described in figure 2, this response depends on the spectral filter transmittance, the detector spectral sensitivity and on the spectral response of the optics in the system. To model the spectral response of the system first, Slater (1980) related the irradiance on a detector located on the optical axis at the image plane to the scene radiance $L_\lambda(u,v)$ at the object plane by the camera equation

$$E_\lambda(u,v) = \frac{\pi\tau_o(\lambda)}{4N^2} L_\lambda(u,v) \qquad (1)$$

where N is the optics *f-number* given by the focal length divided by the aperture stop diameter and $\tau_o(\lambda)$ is the optics transmittance without considering the spectral filters. The optical transmittance is often high for most optical systems and spectrally flat. The u and v coordinates in equation 1 remain unchanged for simplicity, assuming a magnification of unity between the object and the image plane. Therefore, the spectral input and output relationship of the system in band b is defined as

$$S_b(u,v) = \int_{\lambda_{min}}^{\lambda_{max}} R_b(\lambda) r_\lambda(u,v) E_\lambda(u,v) d\lambda \quad (2)$$

In equation 2 the input and output is related by the spectral response $R_b(\lambda)$ of the optics and the filter multiplied by the spectral responsivity $r_\lambda(u,v)$ of the detector. Here, the responsivity of the detector is included as a function of the spatial coordinate u and v. This term is added to account for the spatial non-uniform responsivity in the sensors within the FPA (Perry and Dereniak 1993). The limits in the integration depend on the full width half maximum (FWHM) pass-band of the filter and on band b. The FWHM pass-band is given by the two extreme values of wavelength at which the transmittance of

the filter is equal to half of its maximum value. We refer to band b as the integrated wavelength over the limits in equation 2.

2.2.2 Spatial Response

The spatial response describes the sensitivity of the system to incoming radiation from different directions. For NIR HSI systems using the wavelength tuning with filters method, the spatial response depends on the characteristic focusing of the optics at band b, the reflective properties of the scene at the specified band, and the detectors' spatial responses at the given band. In general, the system affects the spatial characteristics of the scene radiance being imaged with geometric distortions and blurring. This effect can be modeled using the two-dimensional spatial convolution given by

$$e_b(u,v) = \int_{\alpha_{min}}^{\alpha_{max}} \int_{\beta_{min}}^{\beta_{max}} S_b(\alpha,\beta)\, PSF_{net}(u-\alpha, v-\beta) d\beta d\alpha \quad (3)$$

Here, the limits of the integration define the spatial extent of the point spread function (PSF) about the coordinates u and v. The PSF is the response of an imaging system to a point source of light. The PSF in equation 3 determines the spatial response of the entire system (Gonzales 2001). Assuming system linearity, the net PSF is obtained with the two-dimensional spatial convolution, denoted by *, between the optics and detector PSF's as given by:

$$PSF_{net}(u,v) = PSF_{opt}(u,v) * PSF_{det}(u,v) \quad (4)$$

where $PSF_{opt}(u,v)$ and $PSF_{det}(u,v)$ are often given by equations

$$PSF_{opt}(u,v) = \frac{1}{2\pi pq} \cdot e^{\frac{-u^2}{2p^2}} \cdot e^{\frac{-v^2}{2q^2}} \quad (5)$$

$$PSF_{det}(u,v) = rect(\frac{u}{ps}) \cdot rect(\frac{v}{ps}) \quad (6)$$

The optical *PSF* in equation 5 is modeled by a two-dimensional Gaussian function in which the parameters p and q determine the width of the optics *PSF* in the horizontal and vertical directions, respectively. These parameters determine the amount of blurring introduced by the optical system. This blurring depends on many factors, including optical diffraction, aberrations and mechanical assembly quality of the optical system (Ren 2003). In equation 6, the function *rect()* is the rectangle function and the variable *ps* is the value representing the size of the detector or sensor. Note *p*s can become a variable accordingly in equation 6 depending on the detector sizes in the u and v directions.

2.2.3 Time drift

Each of the sensors or detectors within the FPA component introduces noise to the final output HS image of the system. This noise is present even in the absence of light. This type of noise is referred to as dark current noise. The dark current in a sensor is a consequence of thermally agitated carriers and other carrier generation processes. The noise mechanisms that depend on temperature are diffusion and generation-recombination (Forrest 1981). Also, the tunnelling of carriers is another source of noise. However, this is not correlated with temperature.

The dark current noise varies from sensor to sensor location within the FPA (Rogalski 2003). Also, this noise varies depending on the time of acquisition and exposure time. These characteristics result in a time drift effect that affects the output of the system. This effect is illustrated by the equation:

$$w_b^{\tau}(u,v) = \int_{t_0}^{t_0+t_e} e_b(u,v)dt + \int_{t_0}^{t_0+t_e} \eta^t(u,v)dt \quad (7)$$

Here, the limits of the integral define the starting time of the acquisition t_0 and the exposure time setting t_e of the camera. The first term corresponds to the signal integrated over the exposure time. The second term in the right side of equation 7 is the integration over the time exposure of the spatially integrated dark current $\eta^t(u,v)$ at time instance t introduced by the detector.

2.2.4 Signal Amplification

The amplification employed by the system on the signal $w_b^\tau(u,v)$ in band b is determined at the sensor design stage to provide sufficient signal level to the analog to digital (A/D) converter for quantization, without incurring saturation. Here, saturation describes the limit to the amount of current that can flow through the system electronics. The purpose of signal amplification is to increase the resolution of the A/D converter. A high resolution is desired in the system to increase contrast in the image output. The resolution of the A/D converter is given as overall voltage or current range divided by the number of A/D levels of the A/D converter.

For imaging systems, the amplification function is performed at the electronics component stage in figure 2. This amplification is determined by setting a gain and offset value to each band b to yield a full digital level range and band replicate out of the A/D converter. The amplification of the system is given for band b by

$$a_b^\tau(u,v) = g_b w_b^\tau(u,v) + offset_b \quad (8)$$

where g_b and $offset_b$ represent the gain and offset applied by the electronics component at band b, respectively.

2.2.5 Sampling and Quantization

The amplified signal is then sampled and digitized by the A/D converter. Common A/D converters are linear quantizers that convert the analog signal level to the nearest integer. The function performed by this component is given as

$$y_{ijk}^{\tau} = int[\, a_b^{\tau}(u, v)\,] \quad (9)$$

Here, the function *int[]* converts the signal level into the nearest integer. Note here that continuous spatial coordinates u, v, spectral band b and time τ have been sampled and discretized to coordinates i, j, k and τ. The output $y_{ijk}^{\tau}$is a digital number at discrete spatial coordinates $i, j,$ wavelength band k and time instance τ.

2.2.6 Co-additions

Some HSI systems use co-added images to increase the signal to noise ratio (SNR). The signal to noise ratio is defined as the ratio of the signal power to the noise power corrupting the signal. A high SNR is desired to increase the detecting ability of the system (Shaw and Mantsch 1999). This is because the performance of the system is degraded with a low SNR. For example, in low SNR values (i.e., close to one), the signal becomes unidentifiable from noise.

Co-additions are helpful especially at some bands b where the sensitivity of the detectors is low. The function of co-adding a total of N_c images is given by the summation

$$y_{ijk}^{\tau} = \sum_{c=1}^{N_c} y_{ijk}^{c\tau} \quad (10)$$

Here, the input $y_{ijk}^{c\tau}$ and output y_{ijk}^{τ} preserve the same notation for simplicity.

2.2.7 Response model rearrangement

Equation 9 represents the digital output of the system after integration over the exposure time of the scene radiance input $L_\lambda(u, v)$ that arrives at the camera. The scene radiance is dependent upon the output radiance of the illumination source and the physical and chemical characteristics of the sample under study for laboratory based systems. For both a chemical analyst and the system's generic user, it is more useful to express equation 9 in terms of the sample or input object. This relationship can be established by defining the input scene radiance as

$$L_\lambda(u, v) = I_\lambda(u, v) * x_\lambda(u, v) \quad (11)$$

where the operator * denotes the two-dimensional convolution between the illumination source signal $I_\lambda(u, v)$and the response of the sample $x_\lambda(u, v)$ in spatial coordinates u and v and wavelength λ. Here, the response of the sample characterizes its physical and chemical characteristics through its reflectivity and/or emmitance. Equation 11 can be introduced into equation 1 to establish the relationship between the output and input object instead of in the output and scene radiance. In the former relationship, the illumination source is considered as part of the system response.

2.2.8 Simplified Model

Equation 9 contains four integrations, one over the system spectral response λ in equation 2, two over the system spatial response in equation 3 and one over the exposure time in equation 7. Also, one summation is used in equation 10 to co-add images for increase of the detector's effective sensitivity. In practice simplifications to equation 9 or 10 are used

to estimate the overall response of the system. The first simplification made is through notation by letting

$$gain_\lambda(u,v) = g_b \cdot R_b(\lambda) \cdot r_\lambda(u,v) \cdot \frac{\pi\tau_o(\lambda)}{4N^2} \cdot (I_\lambda(u,v) * PSF_{net}(u,v)) \quad (12)$$

and

$$bias_b^\tau(u,v) = g_b \int_{t_0}^{t_0+t_e} \eta^t(u,v)d\tau + offset_b \quad (13)$$

this results in the simplified notation equation

$$y_{ijk}^\tau = int[\iint\iint x_\lambda(\alpha,\beta) gain_\lambda(u-\alpha, v-\beta)\, d\lambda d\beta d\alpha dt + bias_b^\tau(u,v)] \quad (14)$$

Here the $gain_\lambda(u,v)$ represents the amplified spectral and spatial response of the overall system. Note that the gain coefficient does not depend on time. The $bias_b^\tau(u,v)$ represents the summation of two terms: an amplified and time integrated dark current noise plus an offset at time instance τ.

The following simplifications of equation 14 are based on Schowengerdt (1997) and Perry and Dereniak (1993). The spectral response of the system can be simplified by assuming $R_b(\lambda)$, $r_\lambda(u,v)$, $\tau_o(\lambda)$ and $I_\lambda(u,v)$ are average constants over the effective spectral band b at their corresponding spatial location. In a similar fashion a simplification can be made on the spatial response of the system assuming that PSF_{net} and the illumination source $I_\lambda(u,v)$ are constant over the limits of the space integrations. The integration over time can be simplified by assuming independence of the illumination source output and sensor responsivity on time. Finally, the non-linear operation *int[]* introduced by the A/D converter can be ignored for high signal levels because the quantization error is a small percentage of the total signal. These simplifications result in the band, space and time integrated discrete sampled equation

$$y_{ijk}^{\tau} = gain_{ijk} \cdot x_{ijk} + bias_{ijk}^{\tau} \quad (15)$$

Here, the $gain_{ijk}$ represents the time independent gain and the $bias_{ijk}^{\tau}$ represents the time dependent bias at sensor location i and j and wavelength k. Both coefficients represent parameters for the system response function.

2.2.9 Response model estimation

The linear model just mentioned is commonly used by the infrared community for correction of the non-uniformity in FPAs (Perry and Dereniak 1993; Torres and Hayat, 2003). The systems used by them are different than ours in that they look into photons emitted by the temperature of objects. Also, their systems obtain a single image instead of HS images. However, the principles and concepts are the same.

The problem in obtaining the system response is based on the estimation accuracy of the model parameters. Common approaches are based on obtaining estimates using information from the output images given an input. The problem of estimation arises, because the noise in the system corrupts the output image. This results in model parameter estimates corrupted by the noise in the system.

To account for these noise sources different methods have been proposed in the infrared community. These can be categorized into calibration based (Perry and Dereniak 1993) and scene based techniques (Torres and Hayat 2003). For HSI involving data cubes of large size, scene based techniques are not feasible because of memory and time complexity constraints. The only method available in the literature for laboratory HSI was developed by Geladi et al. (2004). This method is based on calibration techniques. In Ge-

ladi's study the model parameters are obtained through the inverse relationship of the system response more often known as system calibration.

2.3 System Calibration

2.3.1 Model

In equation 15, the space, band and time integrated reflectance of the input object is transformed by the system to an A/D count level. This forward relationship is useful for the system engineer to determine the overall performance of the system. However, an inverse relationship is often used in practice by the user of the data to determine the characteristics of the sample based on the data obtained (Brown 1993). In the following section, different calibration techniques based on this inverse relationship are explained. These techniques use different assumptions to simplify the system's response model.

2.3.2 Techniques

To our knowledge the only published research paper developed for calibration and correction of laboratory NIR HSI systems using the time resolved wavelength data acquisition method was developed by Geladi et al. (2004). The method is based in using calibration standards of homogeneous reflectance along their surface and over the NIR region. This is to obtain reference output values at each spatial location and spectral band given a known input. These reference values are then used to obtain coefficient estimates of cali-

bration curves. In their research, Geladi et al. (2004) studied one point, linear and quadratic calibrations.

The two point calibration technique maps the digital output of a sensor to a reflectance percentage using two references of known reflectance. These references are: an acquisition with the lights off and covered lens to obtain a dark current reference, and an acquisition imaging a white reflectance standard (i.e., 99 percent). The model used by the two point calibration is given by

$$x_{ijk} = 99 \cdot \frac{y_{ijk}}{y_{ijk}^{99} - y_{ijk}^{0}} - \frac{y_{ijk}^{0}}{y_{ijk}^{99} - y_{ijk}^{0}} \quad (16)$$

where i, j and k are indices for row, column and wavelength respectively, x_{ijk} is the calibrated value in percent reflectance, y_{ijk} is the system measurement to be calibrated in digital level units, y_{ijk}^{99} is the 99 percent reference measurement and y_{ijk}^{0} is the dark current measurement in digital level units. The calibration can be adjusted to any other two reflectance standards. The only requirement is two standards of distinct reflectance and the corresponding equation adjustment. The biggest problem with two point is that it assumes that the measurement of the two reference standards completely represent the time drift in the system.

Linear and quadratic calibrations consist in using mean square (MS) regression estimate to obtain the best line or quadratic curve fit of a set of reference points. Geladi et al. (2004) used four references are used namely 2, 50, 75 and 99 percent reflectance standards. The reference standard set is imaged to obtain a corresponding system output set. This information is then used to find coefficient estimates of the models. Two coefficients, the slope $\hat{a}_{ijk}$ and the offset $\hat{b}_{ijk}$ are obtained for linear model. For the quadratic

calibration model three coefficient estimates are obtained. These are a curvature $\hat{c}_{ijk}$, a slope $\hat{a}_{ijk}$ and an offset $\hat{b}_{ijk}$. Each of the coefficients is obtained for each sensor index *i*, *j* and *k*.

To obtain accurate model parameter estimates, the coefficients that minimize the MS errors given by

$$e_{ijk} = E\{[\boldsymbol{x_{ijk}} - (\hat{a}_{ijk}\boldsymbol{y_{ijk}} + \hat{b}_{ijk})]^2\} \quad (17)$$

$$e_{ijk} = E\{[\boldsymbol{x_{ijk}} - (\hat{c}_{ijk}\boldsymbol{y_{ijk}}\boldsymbol{y_{ijk}} + \hat{a}_{ijk}\boldsymbol{y_{ijk}} + \hat{b}_{ijk})]^2\} \quad (18)$$

for the linear and quadratic models, respectively, are selected as the calibration model estimates. Here, $\boldsymbol{x_{ijk}}$ is the vector with elements x^s_{ijk} indicating the real percent reflectance of index standard *s*, $\boldsymbol{y_{ijk}}$ is the vector with elements y^s_{ijk} of the measurement of index standard *s* and *E{}* is the expected value. The obtained coefficients can now be used to calibrate hyperspectral images *Y* with elements y_{ijk} using any of the matrix linear or quadratic calibration functions

$$\boldsymbol{X} = \boldsymbol{AY} + \boldsymbol{B} \quad (19)$$

$$\boldsymbol{X} = \boldsymbol{CYY} + \boldsymbol{AY} + \boldsymbol{B} \quad (20)$$

accordingly. In this matrix form $\boldsymbol{A}$ is the matrix of slope coefficients with elements $\hat{a}_{ijk}$, $\boldsymbol{B}$ is the matrix of offset coefficients with elements $\hat{b}_{ijk}$, $\boldsymbol{C}$ is the matrix of the curvature coefficients with elements $\hat{c}_{ijk}$ and $\boldsymbol{X}$ with elements $x_{ijk}$is the calibration of $\boldsymbol{Y}$.

This thesis proposes that the problem in using only four measurements for calculating the coefficients in equation 17 and 18 for the linear and quadratic calibrations is that it assumes this data is sufficient to describe the noise sources and time drift. Moreover, quadratic calibration assumes that the responsivity and the illumination source are not linear in

nature. Rather, they have some curvature. In the case of using four reference measurements, quadratic coefficient estimation contains only one degree of freedom which is problematic for model validation.

In Geladi's study the quadratic calibration model is the best approximation to the true values from the linear and two point calibrations. This measure is assessed using the error between a prediction and a measurement. The problem with this measurement is that the improved fit may have been produced by the noise in the system. In this situation, the curvature might be providing refinement to the data fit by reducing the least squares criterion using noisy data. To assess this problem, more information about system noise and time drift is required.

Chapter 3

Materials and Methods

In this chapter, we explain in detail the NIR HSI system specifications, configuration and setup used throughout the experiments. The main components of the NIR HSI system under study include two halogen illumination sources, two LCTFs, a lens and the FPA. In general, the two illumination sources are used to increase the contrast (i.e. signal to noise ratio) in the sampled input. The NIR filters are used to band limit signals to the NIR spectral range and the lens to bring transmitted light into focus. Finally, the FPA together with the A/D converter in the system serves as the imaging device.

We also describe the procedure followed for the calibration and correction of the system. In general, a set of reference standards is imaged to model the response and calibration functions of the system throughout the whole reflectance range. For this purpose, a total of four reference standards with nominal uniform diffuse reflectance of 2, 50, 75 and 99 percent were used. Each of these standards is imaged in twelve consecutive acquisitions to address the problem of time drift affecting the performance of the system. The data acquired is then projected into linear curves to model the response and calibration functions. The parameters obtained from the linear response projections are later used for

the classification of each sensor within the FPA based on its characteristic response using the k-means classifier.

3.1 System Specifications

The NIR HSI system considered in this study is composed of two incandescent illumination sources, a LCTF, a silica-glass lens and an infrared camera with an InGaAs FPA. These components are commonly used in these systems because of their good performance in the NIR region and low cost (Gat 2000; Alexay 2008 and Olsen and Ban 1987). The illumination sources used in this camera are halogen incandescent lamps (model M40189) from Bencher USA operating at 300 watts. These sources contain halogen bulbs that emit light in the visible to near infrared light (400 to 2500 nm wavelengths). The lens used in the camera is model L25F0.95 from Electrophysics. The lens is characterized by a maximum aperture ratio of F0.9 and a focal length of 25 mm. This lens is equipped with antireflective coatings made of MgF_2 material. The electronic filters are two automatic LCTF obtained from VariSpec. Both filters are characterized by a physical aperture of 20 mm and a full width half maximum (FWHM) transmission bandwidth of 10 nm. One of the filters operates in the short NIR region: 650 to 1100 nm and the second operates in the long NIR region: 850 to 1800 nm. The InGaAs FPA used in the camera is from Goodrich Sensors Unlimited, Inc. The FPA consists of 640 × 480 rows and columns of detectors respectively with each detector having dimensions of 27 × 27 μm. The FPA is designed to operate in the 900 to 1700 nm wavelength region at room temperature. This FPA is equipped with an integrated temperature circuitry that stabilizes it to 18° Cel-

sius. The camera is equipped with a power supply, cables and a PCI data acquisition board with 12-bit resolution. Finally, the camera is controlled using a desktop computer. The controlling computer is a Dell Optiplex GX280, with an Intel Pentium 4 processor with 3GHz and 1.00 GB of RAM.

3.2 System Configuration

The InGaAs camera, the filters and the two illumination sources are mounted on a copy-stand with the configuration shown in figure 4. In this configuration the lens of the camera is arranged in between the InGaAs FPA and filters as shown in the figure. Under this configuration, the limiting aperture of the camera is defined by the aperture of the filter. This is because the physical aperture of the filter (20 mm) is smaller than that of the lens (25 mm). The copy-stand provides light source mounts on each side of the camera. Each mount has the capacity to adjust the incident angle of the illumination source. The illumination sources are located at an angle of 45° with respect to the normal of the copy-stand platform. The copy-stand also contains three positions to mount the camera and adjust the tilt angle and for the vertical and horizontal distance from the camera to the copy-stand platform. A vertical distance from the platform to the aperture of the filter of 22 mm was maintained throughout the experiments. The horizontal distance is of 17 mm as measured from the camera mounting to the camera. Finally, the tilt angle of the camera measured as the angle between the normal of the platform and the normal of the camera aperture is of approximately 0°.

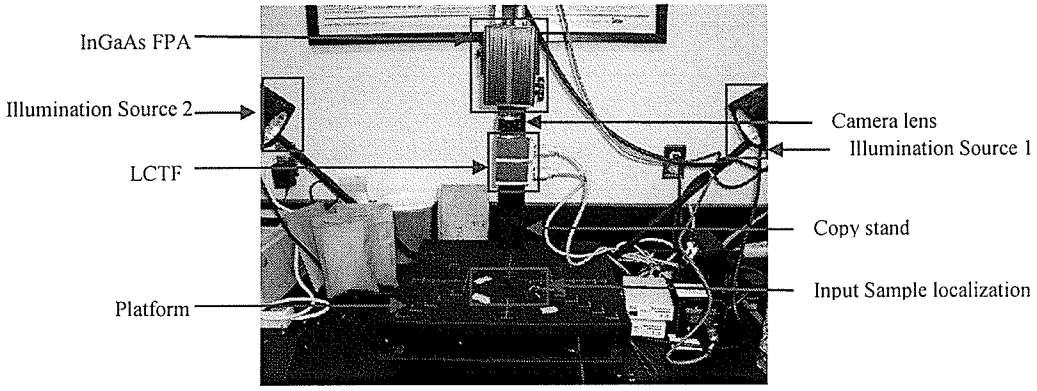

Figure 4: NIR HSI system configuration

3.3 System setup

The system is located in a closed laboratory with no windows and two doors. The temperature in the room was regulated from 20 to 26° Celsius for all experiments. The lights in the room were on unless the camera was in acquisition mode. The system under test is capable of obtaining images from 900 to 1700 nm wavelengths. However, some wavelengths especially near the edge of this range have sensitivity below a usable value. This is due to the decrease in light caused by the filtering of the LCTF and the low spectral response of the detector at those wavelengths. For this reason, the system was set to obtain images from 960 to 1670 nm (inclusive) in steps of 10 nm. This results in a total of 72 wavelength images for each HS data cube. For this system, the 960 and 1670 nm wavelengths give a sufficient contrast between the background noise in the system and a uniform two percent reflectance signal. This is under a multiple exposure of 64 ms and with ten co-additions. This exposure time and number of co-additions has been used throughout all data acquisitions obtained during this research. Preliminary testing indicated that smaller exposure times and/or co-additions result in smaller insufficient signal to noise

ratios at the limiting wavelengths reducing the operating wavelength range. The system was focused manually at the 1320 nm (center) wavelength using the pocket USAF optical test pattern developed by Edmund Optics. The test pattern was localized in the copy-stand platform below the camera as shown in figure 5.

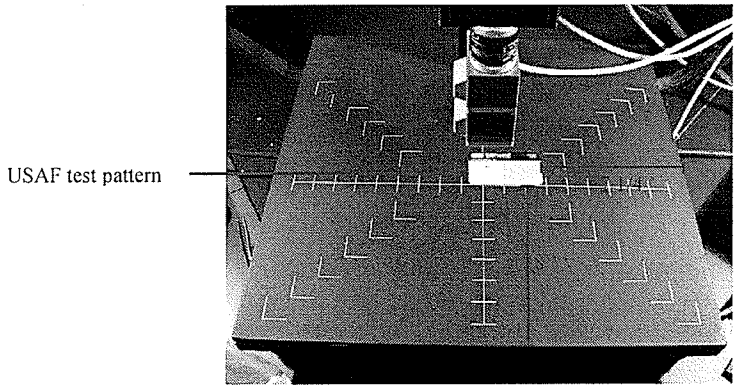

Figure 5: Focusing using the pocket USAF test pattern

After the test pattern was localized, the camera was set to video mode for alignment. To set the camera to this mode and to control all other settings a graphical user interface (GUI) developed in LabView in 2005 by the Institute for Biodiagnostics and Spectroscopy of the National research Council (NRC) was used. This interface provides an option referred to as ALIGN that sets the camera to video mode. Under this mode and with the illumination sources on, the test pattern was manually arranged to cover the entire FOV of the camera. After localization, the lens was manually focused until the instantaneous image shown in the interface shows the lowest visual amount of blurring. This focus was recorded using the markers on the lens. This focus was used throughout the whole data acquisition procedure.

3.4 Data

In this research, the purpose of acquiring data is to analyze the input and output relationship of the system. This relationship helps in understanding the behaviour of the system to establish a model for the system's response. To obtain accurate models for this response attention must be given to the spatial, spectral and time variation of the system. To analyse the spatial variance in the system, data obtained from imaging inputs covering the whole FOV was used. Analysis of the spectral variance was obtained by looking into the input and output relationship of the system across the whole usable wavelength range. To obtain information about the time variance in the system, a series of acquisitions were obtained for each reference input. In this study, a total of twelve HS images were obtained for each reference input being imaged. This is because the time variance in the system may vary depending on the input. The chemical characteristics of the inputs used for this study are: spatially homogenous and spectrally flat along the NIR region. Also, the inputs used vary in reflectance. The physical characteristics are: input references with a flat surface and of considerably large area.

3.5 Calibration standards specifications

The calibration reference standards used as inputs for system response estimation and calibration in this study are non-dispersive, isotropic, homogeneous reflective media from Labsphere. The company develops certified diffuse reflectance standards with known reflective factors and varying sizes. These reflectance standards are spectrally flat over the VIS-NIR spectrum. The reflective areas of the standards are of 50.8 mm in diameter and

of size 60.45 × 15.24 mm in diameter and height, respectively. To cover the dynamic range of the system, we used nominal reflectance factors of 2, 50, 75 and 99 percent. Although each reference standard is labelled with a reflectance factor, the true reflectance of the reference at each wavelength is slightly different.

The true value of each reference standard was obtained from a calibration certificate provided by the manufacturing company. The company obtained this real value from measuring the true reflectance at an 8^{o} hemispherical spectral reflectance for each of our standards at each wavelength we are using. This certificate is traceable to the U.S. National Institute of Standards and technology (NIST). The real reflectance was determined using a Perkin-Elmer Lambda 1900 double beam ratio recording spectrophotometer equipped with a Labsphere RSA-PE-19 integrating sphere accessory. The laboratory temperature at which the measurement was made was from 20 to 26° C. This temperature was approximately the same for the room in which we made our acquisitions.

3.6 Data acquisition

After turning the instrument on and before acquiring data, the system was left for a hundred minutes. This long time interval was left for filter initialization and temperature stabilization inside the camera. The stabilization time of the camera depends on its characteristics. For this system preliminary work showed that the stabilization time is approximately an hour. We note that in shorter acquisition times the noise levels in the system are still varying with time and affecting the performance of the camera. After a hundred minutes have passed, the lights in the room were turned off and the doors in the room

were closed to prevent light in from other rooms. At this point on time, the system was used to begin acquiring data.

To obtain the zero reflectance input or "dark current" noise reference, the two illumination sources were off. Furthermore, a plastic board painted black was used to fully cover the physical aperture of the camera during dark current acquisition. This reduces the amount of light entering through the aperture of the system. The GUI in LabView developed to control the camera contains an option (DARKCOUNT) to collect the dark current noise in the camera. Under this option the camera collects a single dark current image using the number of co-additions determined in the settings section. A single measurement of the dark current means that the system assumes a single frame of the dark current is representative for the dark current noise at all individual wavelengths. The validity of this assumption depends on the NIR emittance of the objects in the room, the plastic cover and of the camera. The time required for a dark current acquisition was less than one second.

To obtain images of the reflectance standards they were first localized within the copy-stand platform. To localize these, we used line magnets as reference guides on the metal platform of the copy-stand at the distances shown in figure 6. Each standard was localized in the same position from acquisition to acquisition using these reference guides and a label in the back of the reference standard. Following localization, the illumination sources were turned on, and the LabView GUI acquisition setting was set to ACQUIRE-DATA. Under this option the camera obtains HS images using the settings described in section 3.3. The time lapse for each HS acquisition was of 2.5 minutes approximately. Immediately after data acquisition the illumination sources were turned off. This was

done to minimize overheating of the illumination sources; to regulate the increase in temperature of the black copy-stand platform and of the input reference standards.

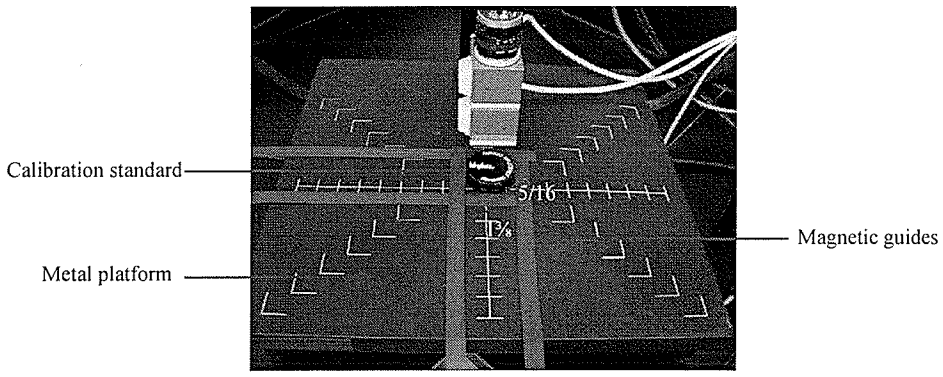

Figure 6: Calibration standard localization

To obtain the input and output relationship throughout the whole input range, the dark current and the 2, 50, 75 and 99 percent reflectance standards were imaged. The procedure followed to obtain this data, was imaging using the order of the sequence: dark current, 2, 50, 75, 99 percent. Each reference input in the sequence, was imaged during consecutive days.

To obtain information about the time drift of the system, a total of twelve acquisitions were obtained per reference input. These twelve acquisitions were obtained in a single day. The time in between each acquisition was of five minutes. The procedure was repeated for a total of five consecutive days to sample all five reference inputs. A total of sixty acquisitions or equivalently twelve samples ($n = 12$) for each reference standard and the dark current were obtained.

In addition to the data collected for calibration, a set of 38 dark current frame acquisitions were obtained. The purpose of this data set was to obtain information about the dark current behaviour of the camera. The camera settings used for acquisitions of this set

were as described in the system setup section 3.3. The acquisitions were obtained on a separate day from those previously described. Similar to the calibration set procedure for acquisitions, the lights in the room were all turned off and the same directions in the procedure for acquiring the dark current frames already described were followed. The difference of this set lies on the fact that the acquisitions were started immediately after the camera was turned on. The time lapse for acquisitions was of a total of 190 minutes with a dark current frame acquisition every 5 minutes.

3.7 Data processing

3.7.1 Analysis software

After data acquisition, the analysis, calibration and testing of the camera was performed in a computer using Matlab version 7.01. The serial output data obtained from the camera is in spc format. Under this format a heading including information about the system settings is included together with the HS image data. This data is arranged into a single vector string. To rearrange this file into HS data cubes, a small function written in Matlab is used. After data transformation, the data is analyzed using the statistics, pattern recognition and image processing toolboxes in Matlab.

3.7.2 System response

The analysis of the system's response was made using the collected data. This was achieved by looking into the characteristic spatial and spectral output and the noise given

a known reference input. To analyze the spatial characteristic response of the system we plotted the histogram of the HS image for each wavelength. The spectral response of the system was then determined by looking into the outputs of sensors as a function of wavelength throughout the whole range. The characteristic time variance in the system was analyzed by plotting sensor outputs of input reference standards as a function of time sliced at certain wavelengths. Finally, the output as a function input throughout the dynamic range was plotted for each sensor and wavelength (See section 4.5 for an example). The parameters in the determined model of the system's response were obtained using the minimum sum of squared errors criterion. To validate the model, the sum of squared errors (SSE) and the prediction sum of squared errors were obtained for each sensor and wavelength. These two criterions were compared using histograms for all wavelengths. The approach followed to validate the model is given in Kutner et al. (2005). This approach is described more in depth in the section 4.7. In summary, the model and the mean sum of squared errors (MSE) as an indicator of the predictive capability of the model are validated if the PRESS and SSE values are similar.

3.7.3 Sensor sensitivity classification

After obtaining the characteristic system response model, each sensor in the FPA has been classified according to its sensitivity. The purpose of the classification is to identify the sensor locations that are saturated, dead, severely corrupted by the optics. The term sensitive region refers to sensors not affected by saturation, dead or severely corrupted by the optics. Insensitive regions was defined as saturated or dead sensors and/or severely corrupted by the optics sensor locations.

The classification is based on first obtaining a feature vector that separates insensitive from sensitive sensors. The feature vector was based on the model used to estimate the system response in section 4.6. To obtain this feature vector, the differences between the sensor responses in each of the regions is analyzed. Based on this analysis, descriptors for the feature vector were chosen. After obtaining the feature vector, pattern vectors corresponding to all sensors were plotted using a scatter plot. A classification algorithm was selected based upon the characteristics of each group.

3.7.4 Calibration

The calibration of the system was performed only on the sensors classified as sensitive. A mask of the sensitive sensor locations was used to remove all other sensors. This mask was obtained using the classification of sensitive sensor locations described in section 3.7.3. The calibration method consisted in using the inverse relationship of the system response model. The coefficients in the model of the inverse relationship were obtained using the minimum squared error criterion. These coefficients were different than those obtained in the forward relationship. The reason is that the forward relationship minimizes the error with respect to A/D counts instead of percent reflectance.

The predictive capability of the model was assessed using the validated root mean sum of squared errors (RMSE). To obtain this indicator the residuals between the fitted values and measurements were obtained for each sensor and wavelength. A plot showing the spatial and spectral distribution of these errors is included (See figure 22). Also, an average over all spatial coordinates RMSE is calculated within the sensitive region. The result is plotted as a function of wavelength in figure 23. This figure aids in determining

the predictive capability of the system as a function of wavelength. The procedures are explained in more detail in the results and analysis section.

Chapter 4

Results and Analysis

This chapter begins by presenting essential details of the collected data including consistent patterns in the responsivity of pixels (i.e., sensors). The second section presents an analysis of the spatial response and the nonuniformity of the focal plane array. This is followed by a presentation of the spectral response, time drift and dynamic range of sensors in the sensitive and insensitive regions. After describing the sensor responses a model of the system's response is developed for each location and wavelength and subsequently verified. Finally the developed model is used to classify the type of sensor response and performance of the calibration of the sensor is discussed.

4.1 Hyperspectral Data Cubes

A total of 48 HS images and 12 dark current measurement frames were obtained using the methods described in Section 3.6. Each of the resulting HS data cubes is a matrix of size 477 × 640 × 72 corresponding to the number of rows, columns and wavelengths respectively. The measured 12 dark current matrices are each of size 477 × 640 and corre-

spond to the number of rows and columns respectively. The value in each entry of both the HS data cubes and the dark current matrices ranges from 0 to 40,950 A/D counts. This output range is the result of co-adding 10 images using an A/D converter having a 12-bit resolution. An example of the output obtained from imaging the 99 percent reflectance sliced at the 1360 nm band is shown in figure 7.

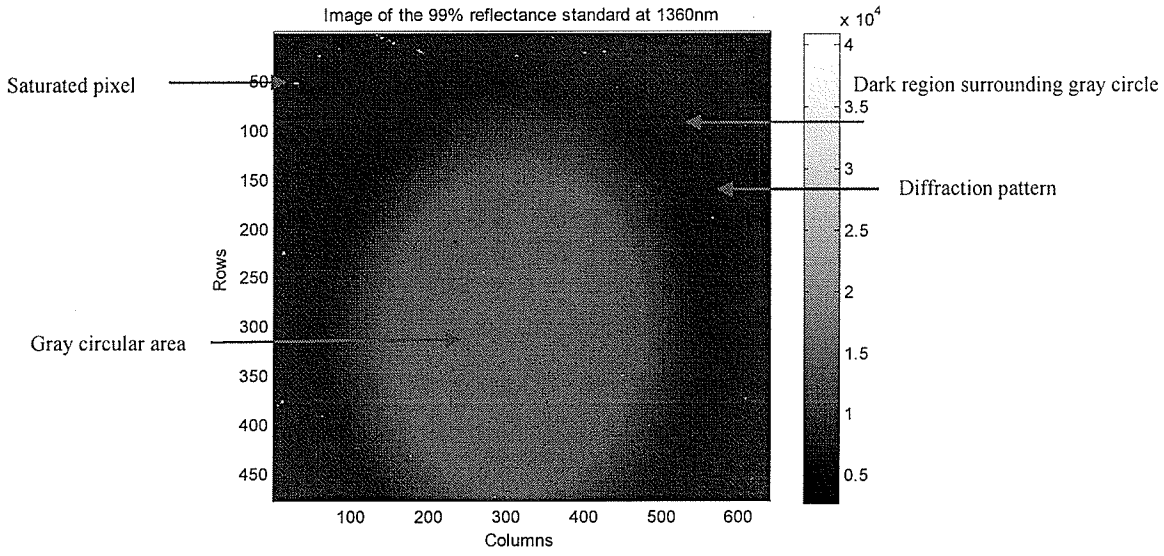

Figure 7: Image of the 99 percent reflectance standard at 1360 nm

Note that the output of the system varies depending on the sensor location. In general, the images obtained at all wavelengths contain the same white dots, black and gray patterns at the same spatial locations. Furthermore, the images obtained using the 2, 50 and the 75 percent reference standards have the same spatial patterns. The difference between images from different standards lies only in the measured A/D counts (i.e., magnitude). This difference depends on both the spectral response and the input reference being imaged. The white dots shown in figure 7 have the maximum A/D level and correspond to saturated sensors. The black areas surrounding the gray circle in the center correspond to

locations severely affected by the limiting aperture of the system, which in this case is the aperture of the LCTF. Notice that inside this black region there are two rings around the center gray circle. These two rings also change in A/D intensity as a function of the spectral responsivity and input reference being imaged. The two rings are caused by diffraction at the limiting aperture of the system. The gray circular pattern in the image corresponds to the input reference signal. Its shape is given by the shape of the limiting aperture of the system, which in this case is circular. Some dark pixels do appear inside the gray circular region. These pixels correspond to sensors that are insufficiently responsive or are dead.

4.2 Spatial response

Analyzing the image of the 99 percent reflectance standard at 1360 nm (see figure 7) yields one of the histograms given in figure 8. The histogram illustrates the intensity variations of an image at one frequency. This figure also includes the histograms resulting from imaging the dark current, the 2, 50 and the 75 percent references sampled at the 1360 nm wavelength.

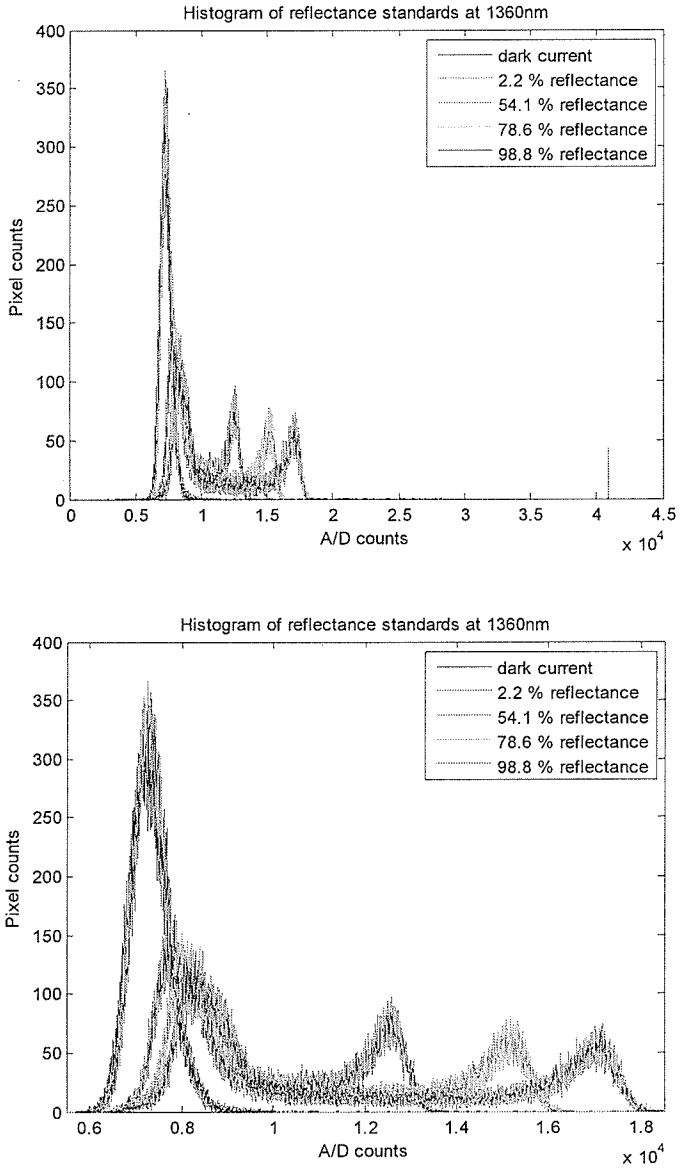

Figure 8: Spatial response variation a) Histogram, b) Zoomed histogram

In figure 8a, the image histograms of the five reference standards illustrate the variation in the spatial response of the system. This variation is introduced by the spatial non-uniformity of the sensors in the FPA, the optical system and the spatial inhomogeneous illumination in the light sources. The impulse located at approximately the maximum A/D level (40,950) in the horizontal axis of the histogram in figure 9a corresponds to the

very bright pixels shown in figure 7. These pixels represent the response of saturated sensors. The two percent reflectance graph shown in green in figure 8 is also similar to the dark current shown in blue. This similarity is emphasized in the enlarged histogram shown in figure 8b. The low variation between the dark current and the two percent reflectance standard occurs because the signal induced by the light entering the camera is considerably small in comparison to dark current signal.

In figure 8b, the histograms for the 50, 75 and 99 percent reference standards each contain two significant peaks. The left peak in the histogram varies little with input reflectance for the 50, 75 and 99 percent reflectance inputs. This variation indicates that the sensors corresponding to the left peak are receiving some signal level. This signal is caused by airy patterns created by the diffraction of light at the limiting circular aperture of the system. In general, this airy pattern consists of a series of concentric rings around the corresponding image of a uniformly illuminated circular aperture (airy disk) as illustrated in figure 7. It is expected that the left peaks in each histogram correspond to the dark areas in the images. The right most peaks in figure 8b corresponding to the 50, 75 and 99 percent reflectance show significant variation between them. It is expected that these peaks correspond to the input reflectance reference signal.

4.3 Spectral Response

Image histograms corresponding to other wavelength slices (See Appendix A figures A.1-16) have a similar shape to figure 8 and their corresponding images are also similar to figure 7. However, image histograms corresponding to other wavelengths differ in the

mean A/D level, which depends on the characteristic spectral response of the sensor and the spectral output of the illumination source. Figure 9a displays, the output of the system at a single sensor located inside the gray circular area (row and column 300) as a function of wavelength for all input references. Notice the differences for A/D values between input references are smaller at the minimum and maximum wavelengths than at the wavelengths in the center. This indicates a lower sensitivity at wavelengths near the limits (<1000 nm and >1650 nm) and a higher sensitivity at the middle wavelengths especially around the 1360 and the 1560 nm wavelengths. All other sensors corresponding to locations inside the gray circular region in figure 7 present a similar spectral response pattern (see Appendix A figures A.17-34).

Sensors corresponding to the locations outside the gray circular region are significantly lower in A/D counts level. Also, the difference in output between reference standards is significantly smaller. An example of the spectral variation of a sensor located in the dark region (row and column 100) is shown in figure 9b. Notice, the A/D counts corresponding to the 75 and 99 percent reflectance standards are above the dark current level at all wavelengths. This indicates that light is incident to these sensors. However, this output signal is affected by diffraction at the aperture of the system and other noise sources. The A/D count corresponding to the 2 percent reference at this sensor location is below the dark current at all wavelengths. Other sensor response types such as those corresponding to saturation look spectrally flat at the maximum A/D level for all reference inputs.

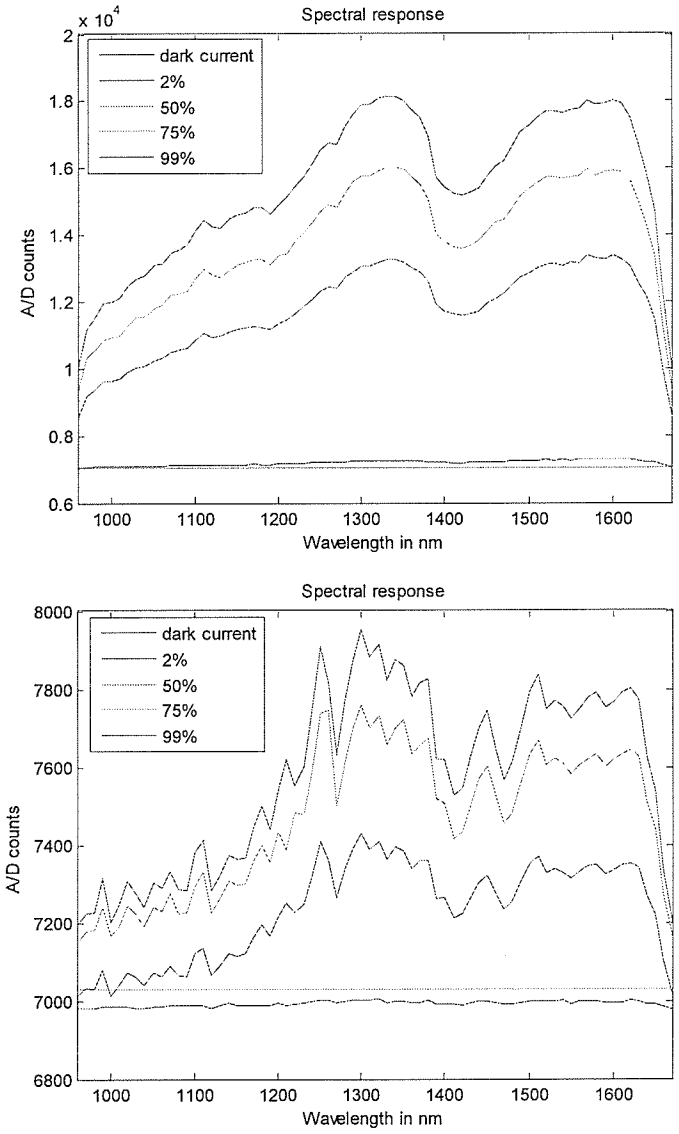

Figure 9: Spectral response variation at a single sensor, a) in sensitive region, b) in dark region

4.4 Time drift

The time drift pattern in the system is illustrated by showing the output of a single sensor as a function of time. The plot is shown in figure 10 for all reference reflectance inputs for the sensor located at row and column 300 sliced at the 1360 nm wavelength. The fig-

ure shows an output drift from measurement to measurement. This drift is as large as 229 A/D counts (i.e., 0.56 percent) for the 99 percent reflectance input and varies depending on the reference input. For example, the maximum observed difference for the 75 percent reference was 167 A/D counts (i.e., 0.41 percent), for the 50 percent reference was 224 A/D counts (i.e., 0.55 percent), for the 2 percent reference was 139 A/D counts (i.e., 0.34 percent) and finally, a maximum observed difference of 25 A/D counts (i.e., 0.06 percent) for the dark current input. These values are calculated from the difference between the maximum and minimum A/D counts in the output for the twelve measurements of each reference input (see legend in figure 10). The small percentage differences after 100 minutes indicate a lack of a non-zero trend.

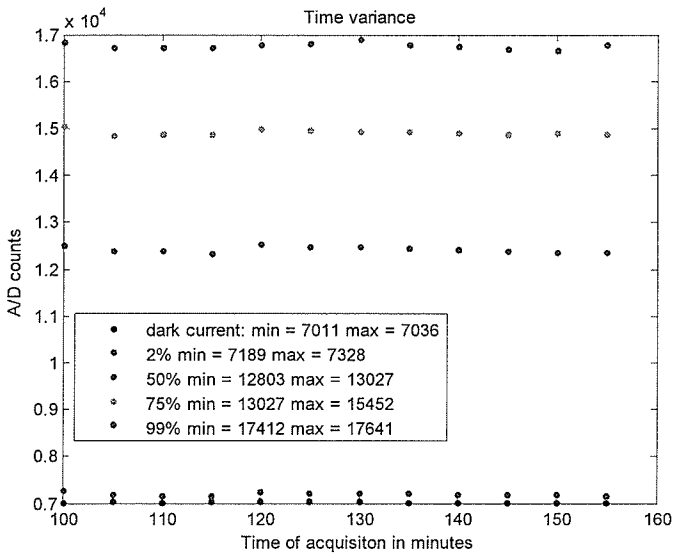

Figure 10: Time response variation at a single sensor

An example of the time drift occurring for acquisitions obtained before a hundred minutes is shown in figure 11. This figure is an example of the time variance in the dark current noise for the sensor located in row and column 300. The procedure followed to

obtain this data is described at the end of the data acquisition section 3.6. Most notable about this figure is the large change in output of the system right after the camera is turned on. It is also worth noting that the noise time variance of the sensor is minimal for acquisitions obtained after the camera has been on for some period of time. Figures 10 and 11 together indicate that the dark current temporal noise is significantly reduced by taking acquisitions after the noise has become stable. For this study, the time lapse for starting acquisitions was chosen to be one hundred minutes. This time lapse was chosen by visual inspection of the dark current behaviour. However, other time lapses can also be chosen depending on the particular stabilization time of the system, user preferences and intended applications.

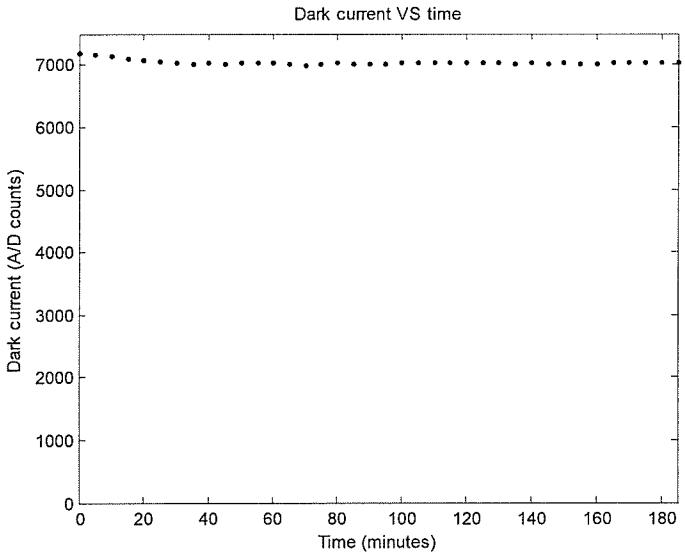

Figure 11: Time variation of noise at a sensor

In general, there is little to no drift occurring in the system after a hundred minutes and the overall characteristic spatial and spectral responses of the system generally remains unaffected. The figures shown for these responses are sufficient to illustrate the

spatial and spectral behaviour of the system (see Appendix A figures A.1-16 and A.17-34 for the intensity variations along space and the spectral variations for various sensors, respectively).

4.5 Dynamic range

The dynamic range of sensors is examined here by displaying the input vs. output relationship of the system. Figure 12 shows plots of the outputs for each acquisition of the corresponding input for two sensors at the 1360 nm wavelength. Figure 12a shows the dynamic range for a sensor located at row and column 300 and figure 12b for a sensor located at row and column 100. Note that these sensors are located inside and outside the gray circle in figure 7, respectively.

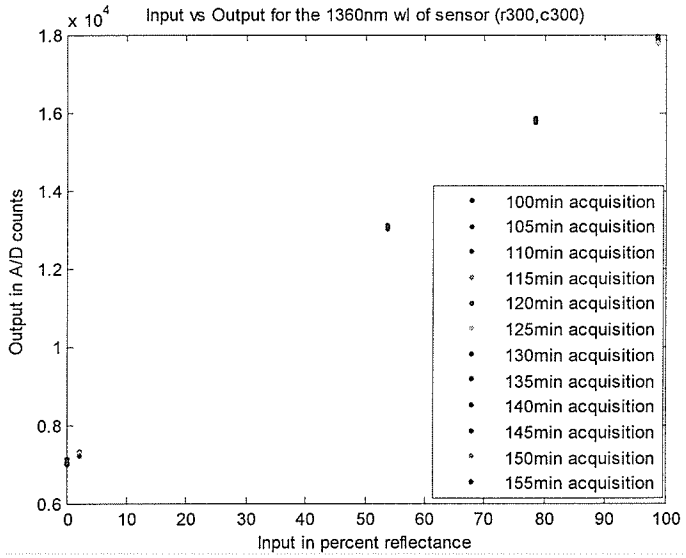

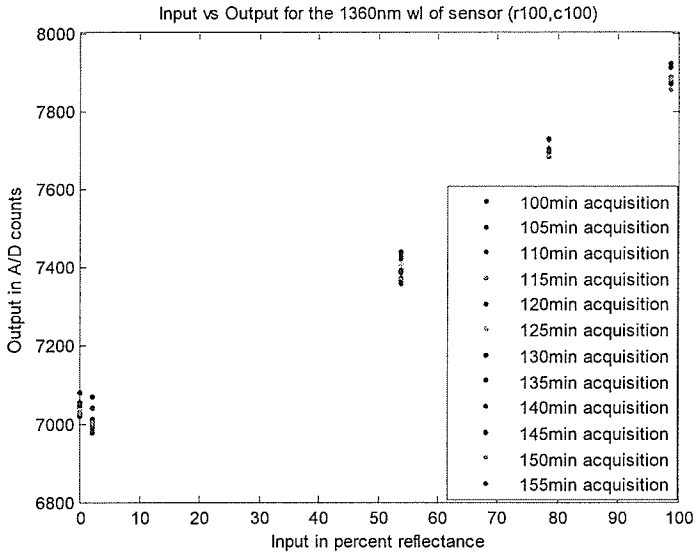

Figure 12: Output as a function of reference input: a) Sensitive region b) Dark region

Note that the response for both sensors is approximately linear. However, the nonlinearities occurring in the sensor of figure 12b are significantly higher when compared to those in figure 12a. These nonlinearities are caused by the lower signal to noise ratio at the regions where light is stopped by the aperture of the system. Also note that the A/D counts range in figure 12b is less than that of figure 12a.

In general, this behaviour is linear at most sensors in the focal plane array. However, some exceptions occur at regions significantly affected by the optics and/or the response of the sensor. Examples of these exceptions are given in figure 13 at the 1360 nm wavelength for acquisitions obtained at a hundred minutes after the camera was switched on.

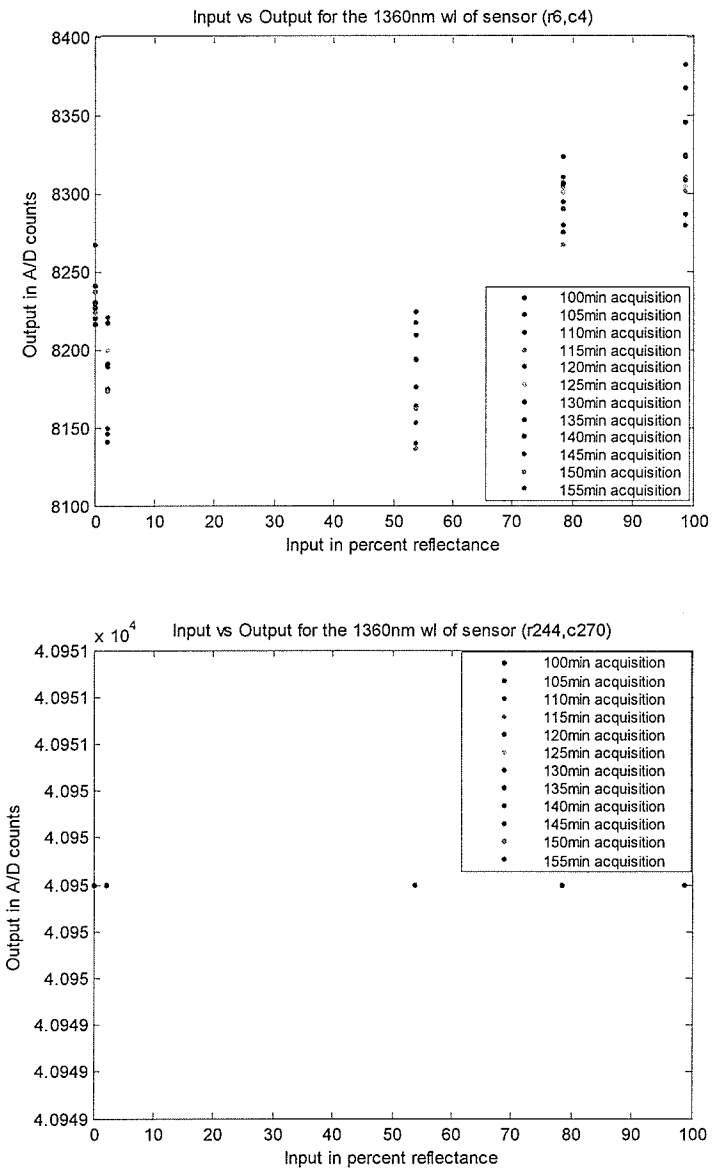

Figure 13: Examples of sensor exceptions from linear response: a) Corrupted by optics and/or sensor response b) Saturated sensor.

Figure 13a shows the sensor located at row 6 and column 4 that corresponds to a region significantly corrupted by the optics and/or the electronics. Note that the nonlinearity of the sensor looks higher than figure 12b. Figure 13b shows an example of a saturated sensor located at row 244 and column 270. Also, note that the response for this sensor is saturated for all measurements. In general, the responses of sensors located inside

the gray circular region appear similar to those shown in figure 12a. Similarly, the responses of sensors located outside the gray circular region appear similar to those in figure 12b. This generality can be confirmed with the aid of figures 8 and 9 and figures A.1-16 and A.17-34 included in appendix A (Note, that the real reflectance value is different than the nominal 2, 50, 75 and 99 percent reflectance factor values).

4.6 System Response Model

Given the characteristics of the system response we adopt the simplified linear response model for each sensor location and specific wavelength as explained in the literature review section. This linear model is given as in equation 15 by

$$y_{ijk}^{\tau} = gain_{ijk} \cdot x_{ijk} + bias_{ijk}^{\tau}$$

Here, $gain_{ijk}$ is the slope parameter estimate of the linear model. This slope parameter has units of A/D counts per percent reflectance and represents the gain of the sensor at the location specified by indices i for i = {1, 2...,477}, j for j = {1,2,..,640}, and wavelength k for k = {1, 2,...,72}. The $bias_{ijk}^{\tau}$ is the offset parameter estimate of the linear model. This offset parameter has units of A/D counts and represents the thermal noise or dark current in the sensor at the location and wavelength specified by the indices. The x_{ijk} represents the input reference response in percent reflectance and y_{ijk}^{τ} represents the corresponding output in A/D counts.

The slope and offset parameter estimates are obtained by minimizing the MS errors in terms of A/D counts for each sensor location and wavelength. This minimization is obtained by setting the problem in terms of matrices and using the Moore-Penrose pseudo-

inverse for the overdetermined case (Moore 1920; Penrose 1955). The solution to this problem is found by minimizing the squared norm

$$V(\boldsymbol{\varphi}_{ijk}) = \|\boldsymbol{y}_{ijk} - \boldsymbol{\Phi}_{ijk}\,\boldsymbol{\varphi}_{ijk}\|^2 \quad (21)$$

given $\boldsymbol{\Phi}_{ijk} \in R^{n \times m}$ and $\boldsymbol{y}_{ijk} \in R^n$. In this case, the vectors $\boldsymbol{y}_{ijk}$ and $\boldsymbol{\varphi}_{ijk}$ and the matrix $\boldsymbol{\Phi}_{ijk}$ involved in the norm are constructed by setting (Kutner et al. 2005)

$$\boldsymbol{\varphi}_{ijk} = \begin{bmatrix} \widehat{gain}_{ijk} \\ \widehat{bias}_{ijk} \end{bmatrix}, \qquad \boldsymbol{\Phi}_{ijk} = \begin{bmatrix} x^{dark\ current}{}_{ijk} & 1 \\ \vdots & \vdots \\ x^{99\%}{}_{ijk} & 1 \end{bmatrix}, \qquad \boldsymbol{y}_{ijk} = \begin{bmatrix} y^{0,dark\ current}{}_{ijk} \\ \vdots \\ y^{12,99\%}{}_{ijk} \end{bmatrix}$$

where $\widehat{gain}_{ijk}$ and $\widehat{bias}_{ijk}$ are estimates for the slope and offset coefficients respectively, $x^s{}_{ijk}$ represents the input reflectance in percent, s for s = {dark current, 2%, 50%, 75%, 99%} is a reference index and $y^{l,s}{}_{ijk}$ is the l^{th} measurement (for l = {1, 2...,12}) in A/D counts of reference standard s at indices i, j and k. In this case the squared norm is minimized by computing $\boldsymbol{\varphi}_{ijk} = (\boldsymbol{\Phi}_{ijk}{}^T\boldsymbol{\Phi}_{ijk})^{-1}\boldsymbol{\Phi}_{ijk}{}^T\boldsymbol{y}_{ijk} = \boldsymbol{\Phi}_{ijk}{}^+\boldsymbol{y}_{ijk}$ where $\boldsymbol{\Phi}_{ijk}{}^T$ is the transpose of $\boldsymbol{\Phi}_{ijk}$ and $\boldsymbol{\Phi}_{ijk}{}^+$ is referred to as the pseudoinverse of $\boldsymbol{\Phi}_{ijk}$. The built-in Matlab function for computing the pseudoinverse was used to ensure correctness of the result. Adding more measurements $y^{l,s}{}_{ijk}$ to compute $\boldsymbol{\varphi}_{ijk}$ in the least squares problem was used to address the issue of time drift in each sensor within the FPA. The result of the regression is split into two HS data cubes with dimensions equal to the HS images: one corresponding to the slope coefficients and one to the offset coefficients.

4.6.1 Slope coefficients

The histograms for the resulting slope coefficients are shown in figure 14 for wavelengths across the whole range in steps of 100 nm. The horizontal axis corresponds to the

slope value in terms of A/D counts per percent reflectance and the vertical axis corresponds to the number of sensors with the value specified in the horizontal axis.

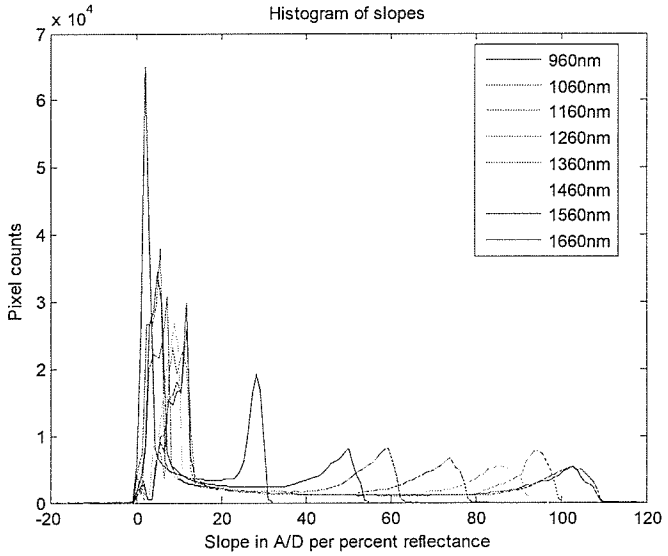

Figure 14: Histograms of slope coefficients

In figure 14, the slope values for each wavelength are mainly distributed into two groups: one close to the zero slopes and the second around a higher slope value that depends on the wavelength. At each wavelength, the group with slope values equal to and close to zero correspond (in the image) to saturated sensors and dark regions surrounding the gray centered circle (see figure 7). Specifically, the slope values equal to zero correspond to sensors under saturation or dead sensors. The other small peaks in the group close to and equal to zero correspond to each of the airy disks formed by diffraction at the aperture of the system. The further away from the center an airy disk is on the corresponding image the lower its peak will be in the histogram of slopes plot (see figures 15a and b).

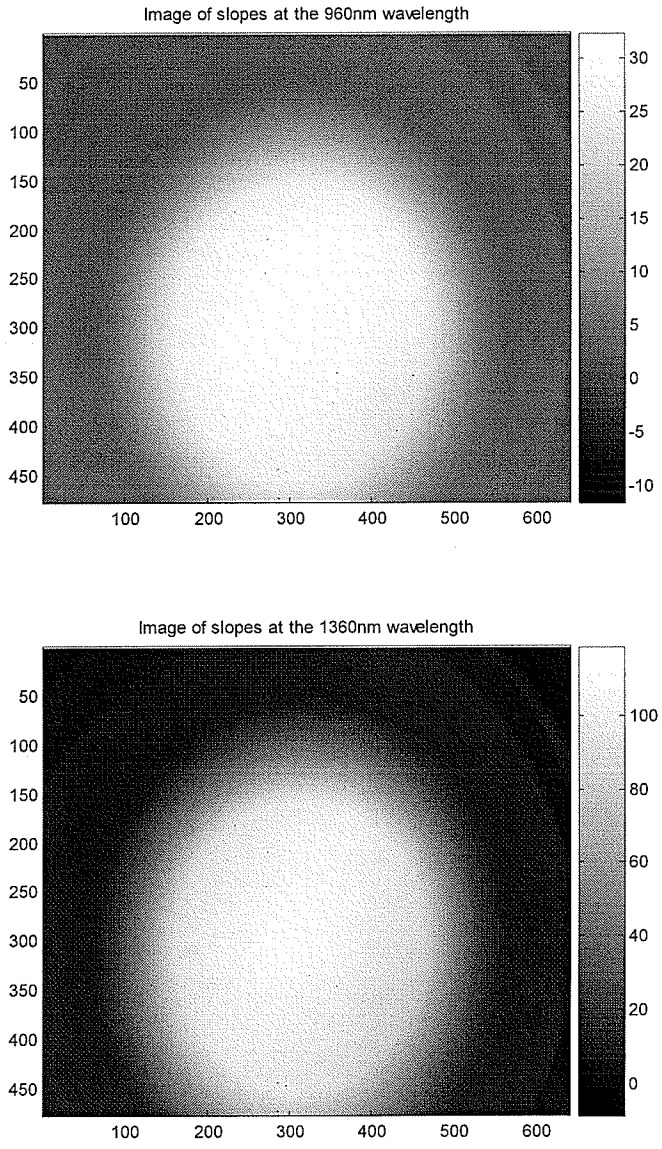

Figure 15: Image of slopes for each sensor a) 960 nm b) 1360 nm

Figures 15a and 15b show images of the slope parameters for the 960 and 1360 nm wavelengths, respectively. The bar in the right of each image indicates the gray scale and the corresponding value for each gray level. Note in the histograms shown in figure 14 that the value of the slopes on the left do not vary by much as a function of wavelength.

This and the low slope values in this group indicate a low sensitivity for the sensors in these regions.

The group distributed around a higher slope value at each wavelength in their corresponding right most peak of figure 14 corresponds to the gray centered circle. This high sensitivity is caused by the optics focusing more light near and into the optical axis of the image. Also, note in figure 14 that the slope values of the peaks change significantly as a function of wavelength. This confirms that the sensitivity of the sensor depends on the operating wavelength, for which the highest sensitivities for the sensor occur near the 1360 and the 1560 nm wavelengths (see figure 8).

The slope values connecting both groups in figure 14 correspond to rings surrounding the gray centered circle. The closer the slope value is to lower A/D counts per percent reflectance values, the further the ring is from the gray circle of figure 15.

4.6.2 Offset coefficients

A histogram of the results for the offset coefficients obtained from the linear model is shown in figure 16a for some wavelengths. The horizontal axis represents the offset value from the regression in units of A/D counts. The vertical axis represents the number of sensors at each wavelength with the value specified by the horizontal axis.

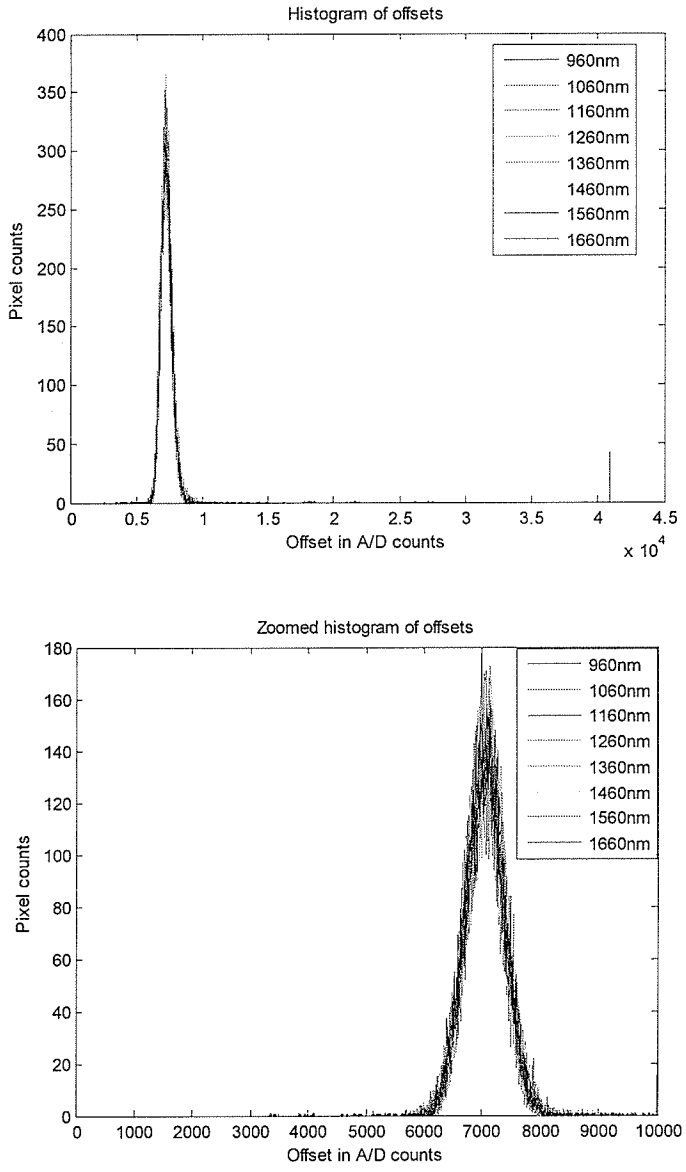

Figure 16: Histograms of offset coefficients a) Full output range b) Zoomed histogram

As shown in figure 16a, most of the data ranges between 5000 and 10,000 A/D counts. This is because the offset represents the dark current noise due to the sensor plus an offset introduced by the electronics. As previously shown in figure 7, the values of the dark current and this electronics offset have the same range, which is in agreement with our model. Also, note there is an impulse peak at the 40,950 A/D counts level in figure

16a. This peak corresponds to the number of saturated sensors shown as very white pixels in figure 7. The sensors corresponding to the offsets with values from 10,000 to less than 40,950 are responsive (i.e. slope value not equal to zero) and located along the whole FPA. Figure 16b shows the offset histogram zoomed from the 0 to the 10,000 A/D counts.

4.7 Model validation

This section validates the use of a linear model by determining the predictive ability of the linear regression using a comparison between the prediction sum of squared errors (PRESS) and the sum of squared errors (SSE) criterion. The importance of comparing these two measures comes from the fact that a PRESS value reasonably close to the SSE justifies model validity (Kutner et al. 2005). Here, the PRESS criterion represents the sum over all references of errors between a model prediction leaving out the reference to be predicted and an observation and the SSE corresponds to the sum of the squared residuals between the observations and the fitted values by the model.

The PRESS criterion is obtained independently for each sensor location i, j and wavelength k. The steps followed to obtain the PRESS criterion are as follows. First, five distinct sets of slope and offset linear model parameters are computed using the Moore-Penrose pseudoinverse as described at the beginning of section 4.6. For each of the five sets, the model parameters are obtained by leaving out all the acquired measurements corresponding to the reference to be predicted. Next, the prediction error corresponding to each of the references to be predicted is obtained by computing the errors between the

model prediction of the omitted reference and the true measurement. Then, the resulting estimation errors are squared and added over all of the twelve measurements. This is repeated for all references. Finally, the prediction squared errors corresponding to each of the five references are added over all references to obtain a single measure referred to as the PRESS criterion at each sensor location and wavelength.

For visualization, a plot of the SSE vs. PRESS criterions is shown in figure 17 for all the sensor locations at the 960 nm wavelength. Plots of other wavelengths are included in Appendix A figures A.35–42.

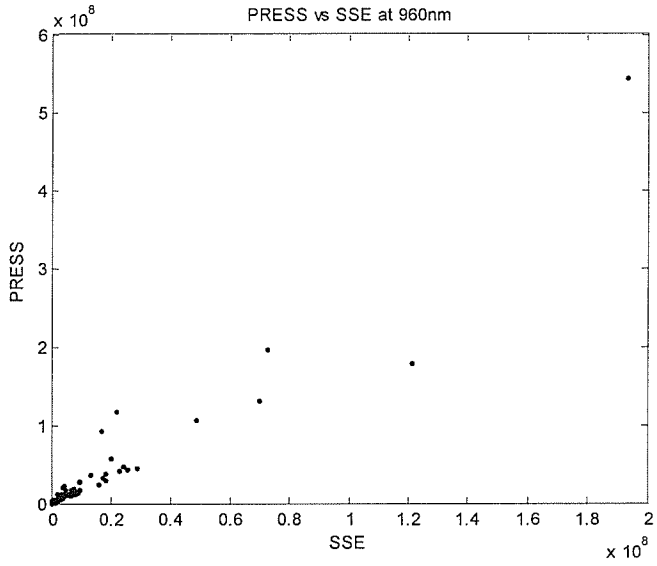

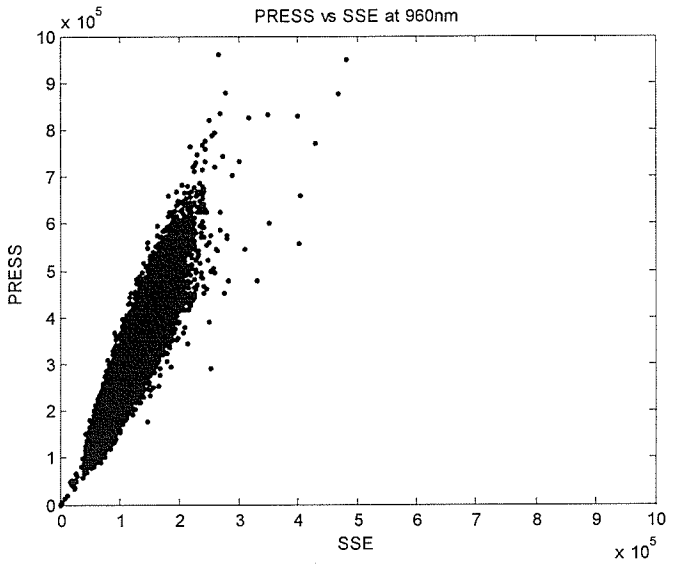

Figure 17: SSE vs. PRESS at the 960nm wavelength a) Full domain and range b) Zoomed plot

The comparison of SSE vs. PRESS is made through histograms of transformed PRESS and SSE criterions for each sensor and wavelength. The transformation applied to the PRESS and SSE criterions is for visualization purposes. The problem in showing raw PRESS and SSE is that the range of both is very large (i.e. 0 - 10^8) (see Appendix A figures A.43-50). The transformation consisted in square rooting and dividing by a scaling factor of sixty (i.e. the total number of acquisitions) for both SSE and PRESS measurements of each sensor and wavelength. This transformation enables a comparison of how close the PRESS and SSE values are. Examples of the results are shown in figure 18a and 18b for the 960 and 1360 nm wavelengths respectively. Histograms for other wavelengths are included in Appendix A (see figures A.51-58).

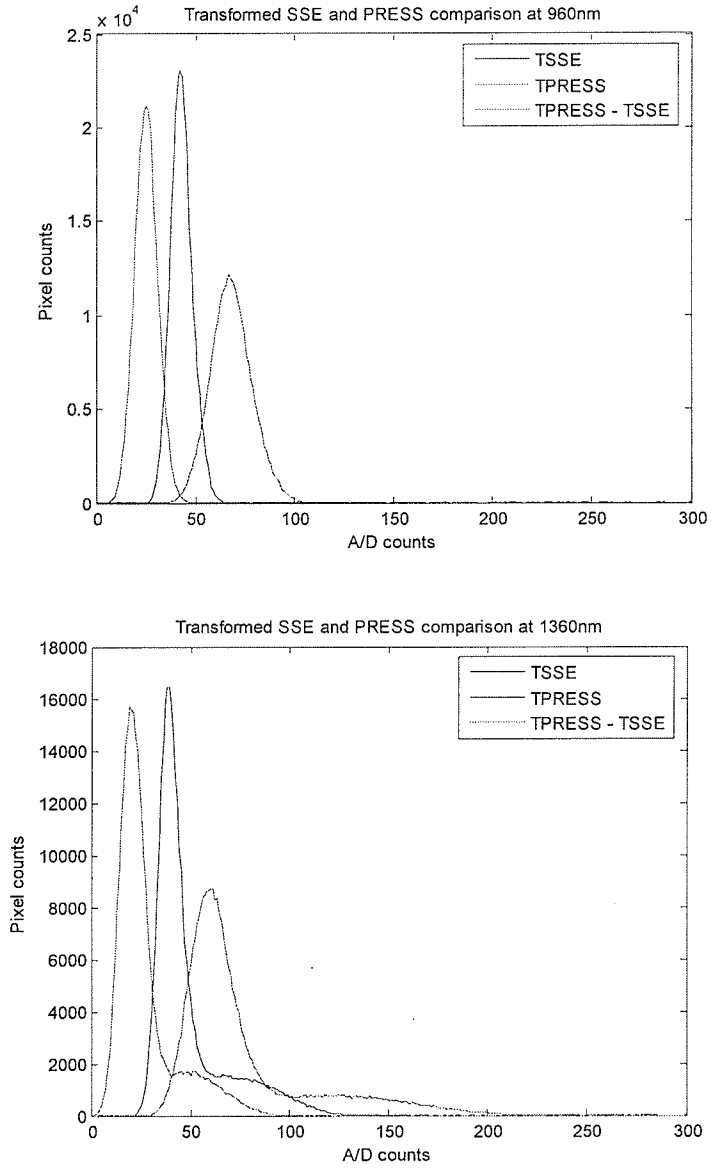

Figure 18: SSE and PRESS comparison a) 960nm b) 1360nm

Note in figures 18a and 18b, that the distribution of the two criterions in both figures have similar shape. Moreover, the resulting errors for both criterions are relatively close to each other considering the output range. The maximum observed difference that occurs at the 960 nm wavelength is of 48 A/D counts and of 97 A/D counts for the 1360 nm wavelength. Similar values are observed throughout all other wavelengths (see Appendix

A figures A.51-58). This small difference between the SSE and PRESS criterions supports the validity of the fitted linear model and of MSE as an indicator for the predictive capability of the model (Kutner et al. 2005).

4.8 Sensor response classification

As shown in previous sections, pixels are divisible into two main sensor groups with significant differences in their sensitivity. The first corresponds to a dark region surrounding the gray centered circle and the second corresponds to the gray centered circle. For this reason, the images obtained are classified into regions of data obtained from insensitive and sensitive sensor locations.

This section defines and classifies an insensitive sensor location to be a sensor location affected by saturation, dead sensors and/or very low sensitivity. The very low sensitivity of a location in this system might be caused by the limiting aperture of the system, limiting light and/or by the low responsivity of the sensor. Furthermore, the limiting aperture causes diffraction which causes undesired light rays incident into sensors creating airy disks in the resulting image. These airy disks are in general low in A/D intensity in comparison to the gray centered circle in the image. Here, regions with low sensitivity are defined as regions severely corrupted by the optics of the system. The sensitive sensor location is defined here as the sensor location not affected by saturation, dead sensors and/or with very low sensitivity across the whole wavelength range.

4.8.1 Feature vector

The feature vector used for the classification of sensitive and insensitive sensor locations is based on the parameter estimates of the model described in section 4.6 and shown in figures 14 and 16. Note that the information shown in figure 14 indicates that the slope value parameter could be used as a discriminator to separate sensors based on their sensitivity. Thus, the approach of this thesis is to use the slope coefficients obtained from the linear model as the feature vector to classify the sensor locations. This is because the characteristic slope values for each group are well separated from one another (see figure 14 as an example). The offset coefficients are not used in the feature vector. This is because these values are similar for every sensor in the FPA and wavelength, except for those under saturation (see figure 14). Therefore, only the slope values are used to classify the sensor locations in the FPA. The slopes at all wavelengths are used as the feature vector to ensure that each sensor location has a high sensitivity at all wavelengths and therefore correspond to the sensitive locations. This results in the feature vector given by

$$\boldsymbol{\omega} = \begin{bmatrix} \widehat{gain}_{ij1} \\ \vdots \\ \widehat{gain}_{ijK} \end{bmatrix}$$

Here, each component, $\widehat{gain}_{ijk}$, represents the estimated slope of a sensor location i and j at each wavelength k. A total of K ($K = 72$ slices) descriptors are used for each sensor location. In other words, the vector $\boldsymbol{\omega}$ represents the sensitivity in all spectra for each sensor location. This feature vector is used by a classification algorithm to discriminate sensors into sensitive and insensitive sensor locations.

4.8.2 Classification algorithm

The classification algorithm used in this study is the k-means using 2 clusters. The *k*-means algorithm separates data depending on some distance metric from the feature vector to the mean of each cluster (Jain 1999). A pattern vector is assigned to the group with the minimum distance from its corresponding mean. Here, the distance metric used is the Euclidean distance. The k-means algorithm is implemented in Matlab within the built-in function *kmeans()*. The result of using the classification is an image of dimensions 477 × 640 pixels where each element takes the values zero or one for insensitive and sensitive sensor locations respectively. The resulting image is shown in figure 19.

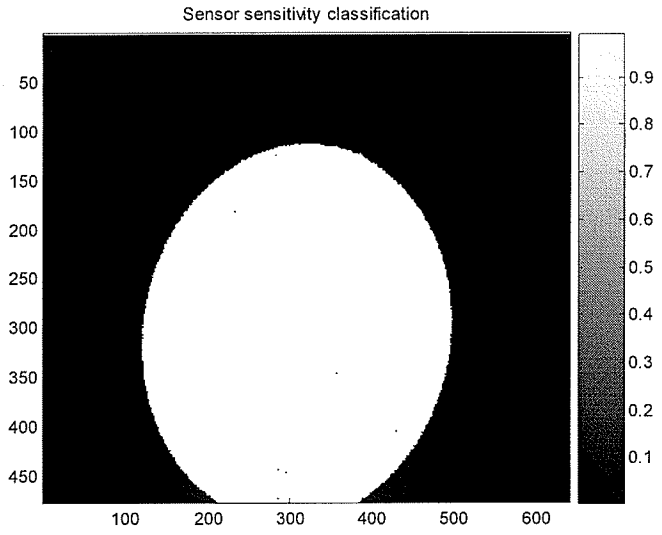

Figure 19: Sensor location sensitivity classification

In figure 19, the sensor locations under saturation, dead, with low responsivity and affected by diffraction are classified as part of insensitive sensor locations. Moreover, some sensor locations inside the white circle are classified as insensitive. These correspond to sensors that have a low responsivity or are dead. Outside the white circle there are no

sensor locations classified as sensitive. This results in a total of 193,871and 111,409 sensors in the insensitive and sensitive regions, respectively. Using this classification, the slope coefficients were separated accordingly using the image in figure 19 as a mask. The result of the slope values corresponding to each group is shown in the histograms in figures 20a and 20b for insensitive and sensitive sensor locations, respectively.

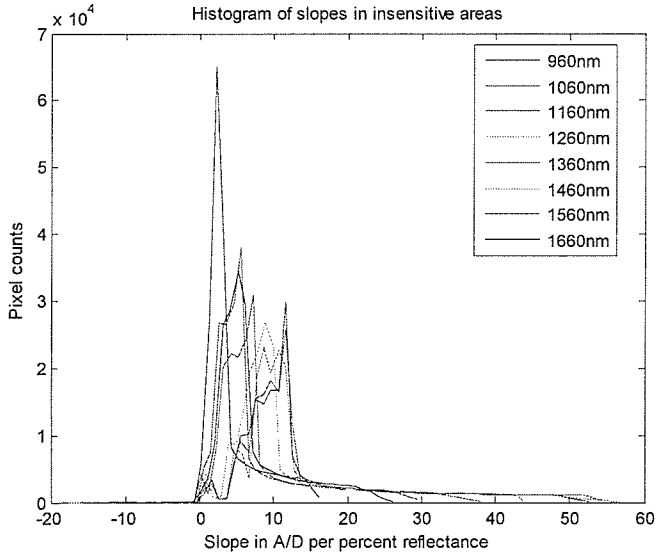

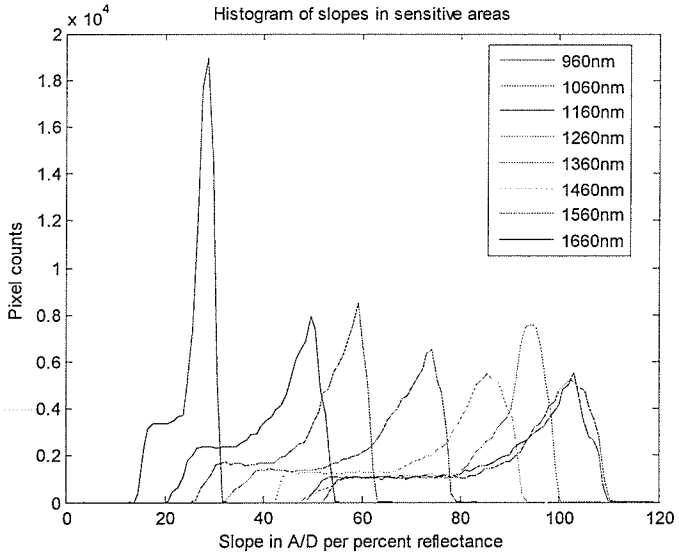

Figure 20: Histograms of sensor location sensitivity: a) Insensitive regions, b) Sensitive regions

The two mean centroids resulting from the classification are shown in figure 21 as a function of wavelength. These two curves represent the mean slope value at each wavelength for each group. Note, that the mean slopes in each group are well separated even at wavelengths with low sensitivity. The mean slope for insensitive sensor locations is low at all wavelengths.

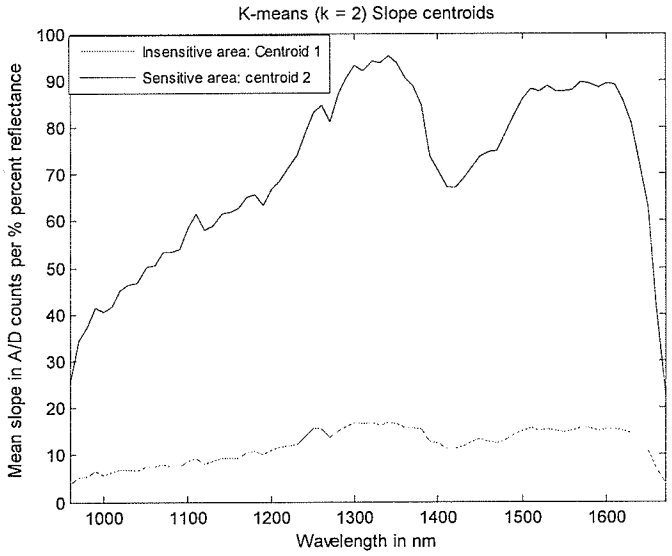

Figure 21: *k*-means centroids using $k = 2$

4.9 Calibration

The calibration of the NIR HSI system is performed using the inverse relationship of the system response. As mentioned in section 2.3.1, the response model is referred to as the forward relationship and defines a relationship between the input in percent reflectance and the output of the system in A/D counts. In the inverse relationship, the output in terms of percent reflectance and the input in A/D counts is used to estimate the reflec-

tance of the measured input. In this inverse relationship, a new set of linear coefficients must be obtained that differ from the obtained system response slope and offset coefficients. To determine the coefficients in the forward relationship the squared error in the coefficient estimation is minimized in terms of A/D counts whereas the inverse relationship minimizes the squared errors with respect to percent reflectance. Therefore, the inverse relationship gives better coefficient estimates for calibration.

The linear model used for the system response is used as the model for calibration. This calibration is applied only to the sensor locations classified as sensitive. The performance of the model was assessed using the validated RMSE. As mentioned earlier, the RMSE is an indicator of the predictive capability of the model. The resulting RMSE's for all sensor locations and wavelengths are shown in the histograms of figure 22.

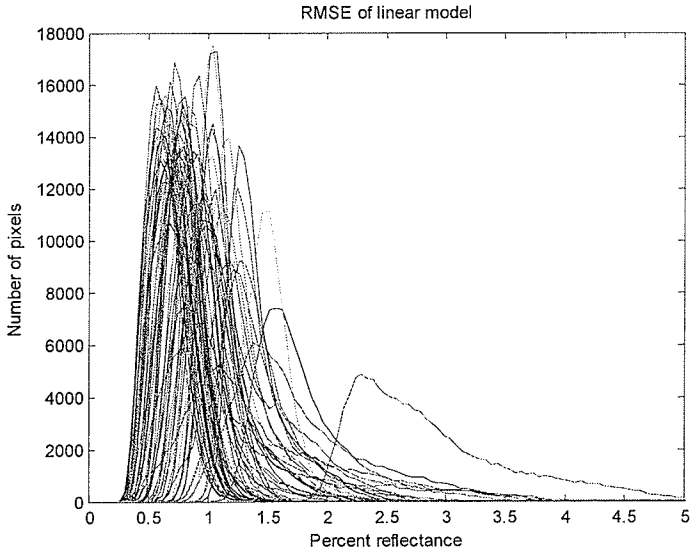

Figure 22: RMSE Histogram for each wavelength

Each curve represents a wavelength and each distribution represents the spatial distribution of the RMSEs. Note that the RMSE distribution appears to approximate a Gaus-

sian distribution for all wavelengths. Also note that there are some wavelengths with a higher prediction error. To illustrate this, figure 23 contains the mean RMSEs over all sensors in the sensitive region at each wavelength.

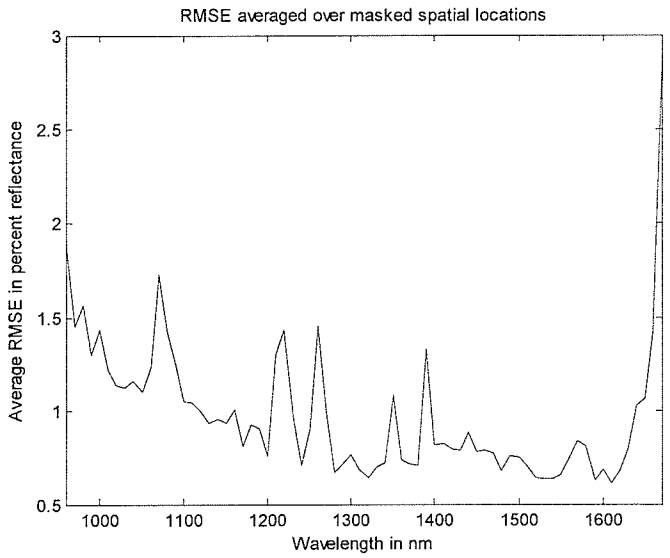

Figure 23: Mean RMSE as a function of wavelength

Note here that in most wavelengths, the mean root mean squared error is below one and half percent. The wavelengths with mean RMSE higher than one and a half are the 1670, 960, 1070 and the 980 nm wavelengths (arranged in descending order). This value is an estimate of the standard deviation of the system noise in terms of percent reflectance and an indicator of the goodness of fit of the linear model as the system response estimate.

At the end of this chapter we presented the results and performance of the linear model as the system response and calibration estimate. However, a few more comparisons and tests are required to indicate whether or not this model is the best estimate of the response and calibration function of the system. For this purpose, we evaluate the good-

ness of fit of models of higher degree (i.e., the quadratic model) as the system response estimate and compare it with that of the linear model in the next chapter. The comparison is made using a hierarchical test which uses the F statistic as described in the next chapter. This comparison is used to evaluate the significance of the quadratic term in the model. Also, we discuss some of the problems in validating the quadratic model using the available input references. Finally, we discuss and illustrate the importance of the building model data set in the performance of the linear model.

Chapter 5

Discussion

Typical problems related to the instrumentation of NIR HSI systems are described in the introduction and the literature review. The materials and methods chapter describes a procedure using calibrated references to understand and address those problems. The results and analysis chapter addresses the main problems encountered in NIR HSI systems. Finally, this section deals with the significance of the results by describing the effectiveness of the procedure on solving the issues typically found in NIR HSI systems. In addition, the procedure is compared with others developed in the literature.

In brief, the procedure developed in the realm of this thesis begins by acquiring data used to describe the system's dynamic range, and its variances spectrally, spatially and temporally. To achieve this, a set of five standards of distinct reflectance were imaged separately in twelve repeated acquisitions at specific times. The next step constructs a linear model based on the data acquired for each of the sensors within the FPA and operating wavelength of the system. The constructed models consider the response of each sensor individually on a wavelength-by-wavelength basis which allows for correction of the spatial and spectral nonuniformity (Geladi et al. 2004) and of the dark current varia-

tion of each sensor. The next step consists of using the slope parameter of the developed model as a descriptor of its sensitivity to classify their individual response. This interpretation can be understood by noting that the slope coefficient is the only parameter of the model changing as a function of input (figures 14 and 16). In other words, the slope parameter contains sufficient information to describe the responsivity of each individual sensor (e.g., defective: dead or saturated, low sensitivity, etc.). Additionally, this interpretation also allows a modelling of the characteristic dark current by means of the offset parameter from the linear model (described in section 2.2.8). This is confirmed with the histogram of sensor offsets (figure 16), which shows that the parameter does not change as a function of input nor wavelength.

A k-means classifier, with k=2, was also implemented for classification of sensors across the whole FPA based upon their sensitivity. This allows for the identification of the sensors significantly affected by the aperture of the system, defective: dead or saturated, and in general sensors presenting a small slope (i.e., low sensitivity). Finally a linear calibration function was determined and implemented only on the sensors classified as sensitive as described in section 4.9. Note that the calibration function was not obtained using the inverse of the forward relationship (i.e., the response function) rather; it was obtained by minimizing the squared error of percent reflectance. This calibration procedure addresses the problem of data in units that are not meaningful to the chemical analyst.

Two main observations described by Geladi et al. (2004) differ from the procedure of calibration and correction proposed in this thesis. The first observation is that the number of reference standards needs to be increased to improve the response and calibration ap-

proximation of the model. Unfortunately, increasing the number of reference standards is limited by their high cost. In general, fabrication of reference standards for the NIR region requires sophisticated processes to preserve the purity of the reflective material, thus, increasing the cost of manufacturing. Also, the number of references required for accurate estimation of the noise drift statistics is significantly high if only one measurement per reference is obtained. The second observation is that the response of the sensor is slightly nonlinear thus requiring a higher order model to obtain a more accurate response approximation. The following section is dedicated to discussing and evaluating the refinement provided by a second order term in the model using a hierarchical F test.

The end of the discussion chapter focuses on assessing the performance of the proposed linear calibration using the complete (i.e., the 60 HS measurements) reference data set in comparison to the model obtained using a single HS measurement for each of the references. The performance is assessed using the previously validated RMSE as the measure.

5.1 Second Order Regression Model

5.1.1 Diagnostics

This section uses the results of this thesis to discuss the first observation of Geladi et al. (2004) that the quadratic model better approximates the true response function of the system. Their main suggestion is that the response of the sensors is slightly nonlinear. However a few problems are associated with using a quadratic term in the model. Data diag-

nostics are presented in this section to determine whether or not the second order term is significant in improving the model's approximation. The suggested second order model is given by

$$DN_{ijk} = c_{ijk}PSFs^2 + g_{ijk}PSFs_{ijk} + bias_{ijk} \quad (22)$$

Here, the variable c_{ijk} corresponds to the quadratic effect coefficient at sensor location i, j and wavelength k. The other parameters and variables represent the gain and offset as in the linear response model. To check whether the second order term c_{ijk} provides significant refinements to the model, the hypothesis test

$$H_0: c_{ijk} = 0$$

$$H_a: c_{ijk} \neq 0$$

was used. Here, H_0 and H_a represent the null and the alternative hypothesis respectively. The null hypothesis states that the second order term in the model is not significant. The alternative hypothesis states the opposite. To obtain the coefficients of the second order term model, the quadratic function that better fits the input reference data points was obtained. The method used to obtain the quadratic model coefficients (see section 4.6) was the Moore-Penrose pseudoinverse for the overdetermined case (Moore 1920; Penrose 1955). However, the matrix setup was modified to include the second order term component as follows

$$\boldsymbol{\varphi_{ijk}} = \begin{bmatrix} \widehat{c_{ijk}} \\ \widehat{gain}_{ijk} \\ \widehat{bias}_{ijk} \end{bmatrix}, \boldsymbol{\Phi_{ijk}} = \begin{bmatrix} {x^{drk\ crnt}}_{ijk}^{\ 2} & {x^{drk\ crnt}}_{ijk} & 1 \\ \vdots & \vdots & \vdots \\ {x^{99\%}}_{ijk}^{\ 2} & {x^{99\%}}_{ijk} & 1 \end{bmatrix}, \quad \boldsymbol{y_{ijk}} = \begin{bmatrix} {y^{0,drk\ crnt}}_{ijk} \\ \vdots \\ {y^{12,99\%}}_{ijk} \end{bmatrix}$$

Where $\widehat{c_{ijk}}$, $\widehat{gain}_{ijk}$ and $\widehat{bias}_{ijk}$ are estimates for the curvature, slope and offset coefficients, respectively, ${x^s}_{ijk}$ represents the input reflectance in percent, s for s = {dark cur-

rent, 2%, 50%, 75%, 99%} is a reference index and $y^{l,s}{}_{ijk}$ is the l^{th} measurement (for l = {1, 2...,12}) in A/D counts of reference standard s at indices i, j and k. The squared norm

$$V(\boldsymbol{\varphi}_{ijk}) = \|\boldsymbol{y}_{ijk} - \boldsymbol{\Phi}_{ijk}\,\boldsymbol{\varphi}_{ijk}\|^2 \quad (23)$$

was minimized in the same way as described in section 4.6. The resulting elements of φ_{ijk} were separated and rearranged into three HS data cubes corresponding each to the quadratic effect term, the gain and the bias coefficients.

To test the two hypotheses, the residuals between the observation and the fitted value were obtained for each reference, sensor location, wavelength and model. For each model, sensor location and wavelength, their corresponding residuals are squared and added to obtain a HS data matrix containing the SSE at each entry. This is done only for the region previously classified as sensitive. After obtaining the SSE for each sensor location and wavelength, the hypothesis alternatives were tested using a hierarchical test described in Kutner et al. (2005). The test consists in using the partial F test statistic given by

$$F^* = \frac{MSR(x^2|x)}{MSE} \qquad (24)$$

Here, the *MSE* in the denominator represents the mean sum of squared errors obtained from the model including the second order term. The numerator $MSR(x^2|x)$ represents the mean regression sum of squares of adding x^2 given that x was already included in the model. In short, the numerator is given by (Kutner et al. 2005)

$$MSR(Px^2|x) = \frac{SSE(x) - SSE(x^2,x)}{1} \quad (25)$$

Note that the degree of freedom for the numerator is one. This is obtained by subtracting the degree of freedom of $SSE(x)$ from the degree of freedom in $SSE(x^2, x)$ that is 58

and 57, respectively. The degree of freedom in the denominator corresponds to the SSE of the second order model. Once all the SSEs where obtained, the F* statistic ratio is obtained for the sensitive region. The resulting HS data cube contains entries where each entry represents the F* statistic value at the respective sensor location and wavelength.

The F* statistics HS cube values were then checked against the percentiles of the F distribution. Here, the confidence level or coefficient α was chosen as 0.01. This stringent value was chosen such that only large deviations from the linear fitted value are considered as the alternative hypothesis. Thus, the F distribution threshold is given by the critical value $F(0.99, 1,2) = 98.5$. F* statistic values higher than the critical value are considered as sensors requiring the refinement introduced by the second order term. With F* values lower than the critical value, the second order term in the response of the sensor at the wavelength under test are considered as insignificant. The F* statistics HS data cube was classified in Matlab using the critical value as a threshold. The result was an HS matrix with values one and zero and dimensions equal to the specified settings for HS images (i.e. $477 \times 640 \times 72$). Sensor locations with a value of one correspond to sensors with a significant second order term. Values of zero correspond to the null hypothesis. An example is shown in figure 24 sliced at the 1360 nm wavelength.

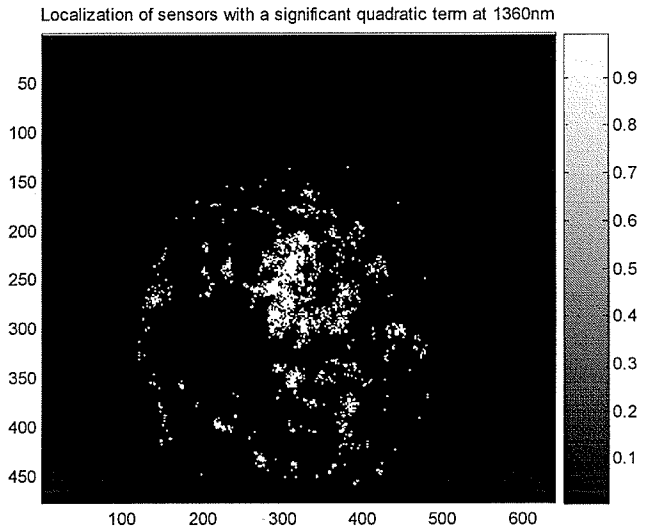

Figure 24: Localization of sensors with a significant second power term at 1360 nm

In figure 24, the sensors with a significant curvature at the 1360 nm wavelength are located all along the sensitive region with some clustered around the center of the image. The total number of sensors within the sensitive region with a significant second order refinement is 5461 out of 111,409 (i.e., 4.9 percent). For other wavelengths, the density and location of sensors with a significant second order refinement varies randomly. To illustrate how these sensors vary in density, the total number of sensors with a significant second order term were counted and plotted as a function of wavelength. The resulting plot is given in figure 25.

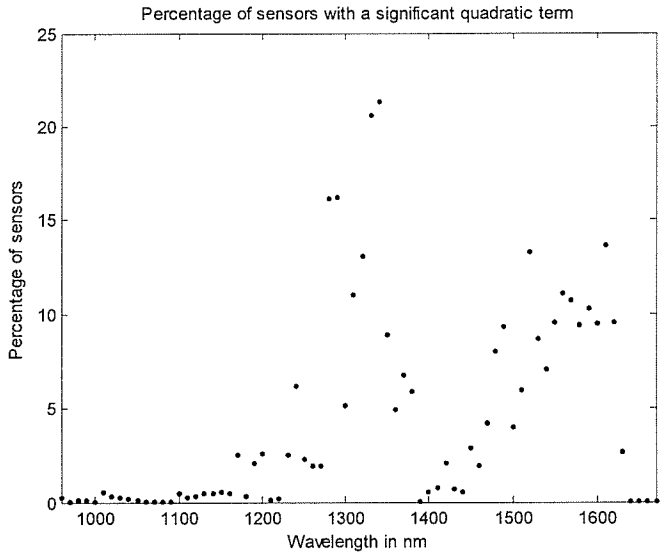

Figure 25: Percentage of sensors with a significant quadratic term, $\alpha = 0.01$.

Here, the vertical axis represents the percentage of sensors with a significant second order term. The normalization was carried out by dividing the total number of sensors in the sensitive region with a significant second order term by the total number of sensors in the whole sensitive region. Note in figure 25 that the number of sensors with a significant second order term appears to have some correlation with the corresponding sensitivity of the wavelength. The higher number of sensors with a significant second order term occurs around wavelengths with high spectral sensitivity (e.g., 1360 nm, 1560 nm). This can be confirmed by comparing figure 25 with figure 9. Note, in figure 25, that the number of sensors with a significant second order response is low in general.

In figures 24 and 25, the reason that the second order term provides a refinement to the fit of the data has two possible reasons. First, the response of the system may contain a real curvature effect. The second possibility is that the nonlinearities are caused by the random nature of sensor noise. This noise could be amplified thereby corrupting the sig-

nal by an amount larger than in other sensors. The noise may also be misclassified by the test as curvature due to the confidence level used. To clarify this, a plot of the dynamic range is shown in figure 26a together with the linear and quadratic fits. The plot shows a single sensor with one of the highest F* numbers at the 1360 nm wavelength (F* = 497.49).

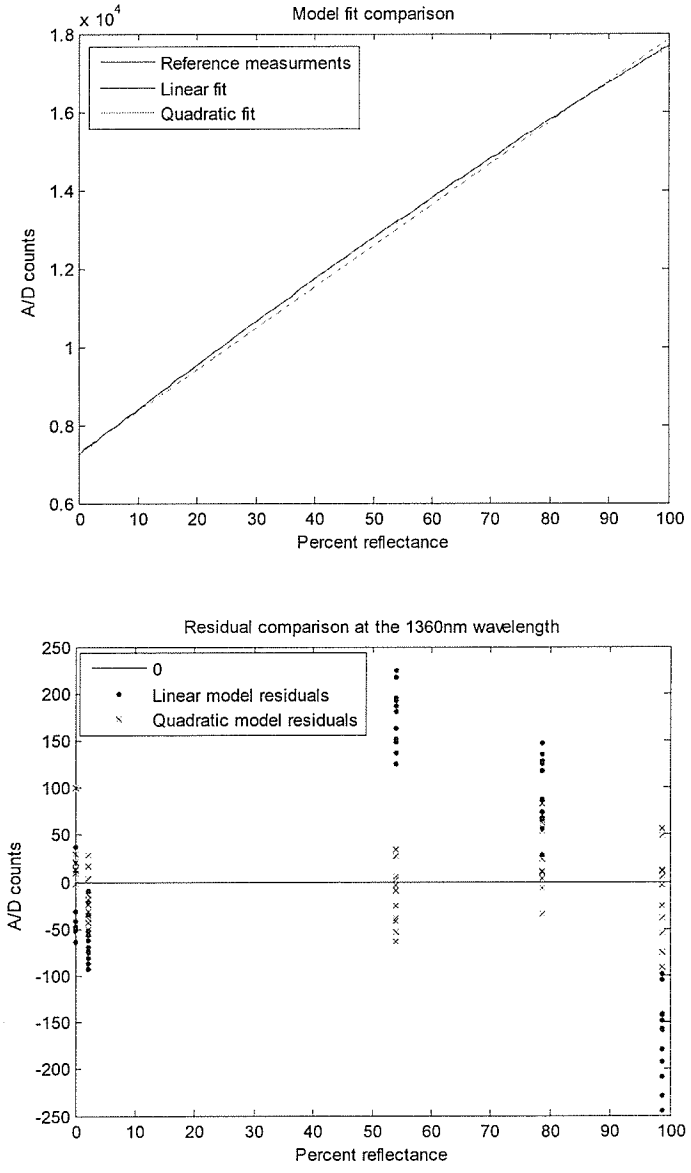

Figure 26: Sensor with a significant second order term a) Dynamic range b) Residuals

In figure 26a, note that the data points are located along a line. Also note that both the first order model and second order model are very near to each other. The refinement provided by the second order model is to curve the line closer to all reference measurements. Figure 26b shows the residuals between the two models and the reference standards for the same sensor and wavelength. It is clear why the second order term provides refinements to fitting. The SSE of the linear model is significantly larger than the SSE of the quadratic model because of the residual level. However, the errors are not high considering the range of the output level in A/D counts. In fact, the RMSE of the linear model in this case is of 125.95 A/D counts per percent reflectance. Considering that the slope of the sensor is of 105.27. The error introduced by the linear model is of approximately 1.19 percent reflectance. The reason why a significant second order refinement was detected by the test involves the statistical problem of the sensitivity and reference set sample size.

5.1.2 Linear and Quadratic Validation Comparison

In the previous section, an F statistics test on the residuals showed that some sensors present a significant second order refinement at specific wavelengths. However, the application of a second order term model for the response and calibration of the system requires proper model validation. In our case this is a problem since the number of reference standards we have available is five. Typically, problems arise in the extrapolation of higher degree polynomials especially at edges. For this reason, the PRESS criterion previously used for model validation is higher in comparison to the PRESS of the linear model. To illustrate this, the transformed SSE and PRESS comparison (the transformation consists

of dividing by sixty and square rooting the data individually for each sensor location and wavelength) between the linear and quadratic model is shown in figure 27 for the 1260 nm wavelength.

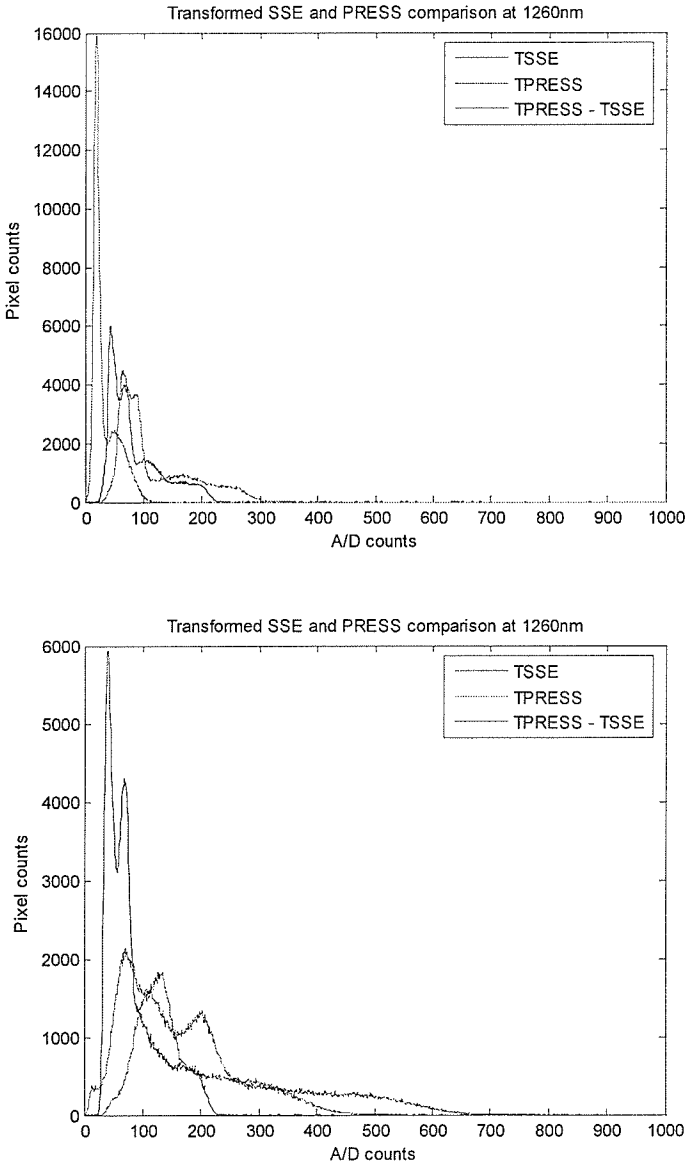

Figure 27: Model validation comparison a) Linear model b) Quadratic model

Figure 27a and 27b corresponds to the SSE and PRESS comparison using the linear and quadratic models respectively. In the linear case, the PRESS distribution is very close

to the SSE distribution. This, similarity serves as the criterion for both model validation and the use of the MSE as an indicator of the predictive capability of the model. The SSE in figure 27b is more skewed towards lower transformed errors than in the linear model. This is because a model with a higher order term and fewer degrees of freedom will always fit the data better. This might indicate that a second order term model would describe more accurately the system response. However, note that the PRESS distribution in figure 28b is spread over a higher range of transformed errors in comparison to that of the linear model. Moreover, the differences between the PRESS and SSE in the second order term model are much higher than those for the linear model. This means that the validity of the linear model describing the response of the system is higher than that for the quadratic model.

In general, the use of the second order term model to characterize the response of sensors is problematic. One of the problems in using the quadratic model is that the model is not well validated. Proper validation of the model requires the use of more reference standards to increase the degrees of freedom. Another problem is that the refinement provided by the quadratic model on the sensors with significant second order terms might be just a better fit to the noise included in the reference measurements. Moreover, the number of sensors with a significant second order term shown in figure 25 is very low in comparison to all other sensors accurately described by the linear model. Finally, a quadratic model involves estimation of three parameters: the curvature, slope and offset. This results in three HS data cubes corresponding to each of the coefficients. Considering the size of HS images, this compromises the memory space required to store the coefficients of the model.

5.2 Building Model Data Set

In the last chapter, the response and calibration of the system was approximated with a linear model. This model was obtained using a data set consisting of a set of twelve measurements for each of the five available input references (i.e., the 0, 2, 50, 75 and 99 percent reflectance standards). Certainly, acquiring, managing and storing this data set are tedious tasks which in turn result in important limitations. However, these limitations are necessary to obtain a more accurate model of the response and calibration functions of the system. This is important because the accuracy of the model directly impacts the quality of the subsequent chemical analysis of the sample under study.

The use of one measurement per available reference as described in the paper by Geladi et al. (2004) is insufficient due to the temporal noise affecting the system (see figure 10). In his paper, Geladi et al. suggests using more references to improve the model approximation. Certainly, using a significant number of references allows for estimation of the noise statistics. Unfortunately, reference reflectance standards of specific reflectance are hard to manufacture and expensive to fabricate for the NIR region which imposes a limitation on the available data. For this reason, using a set of repeated measurements of the available references for model construction gives the capability to readily extract the noise statistics for modeling.

To illustrate the possible magnitude of this issue, the performance of a linear model obtained with a full reference data set is compared with that obtained using a single measurement reference data set. The single reference set was obtained from the fourth and fifth acquisitions in the sequence corresponding to the 115 and 120 minute measure-

ments. In this set, the dark current is obtained from the fourth acquisition, the 2 percent reference from the fifth, the 50 percent from the fourth and so forth. These two acquisitions were selected because the highest drift occurs in between these two batches and so the RMSE reflects the worst possible calibration error of the whole data set. For this reason the model building set is labelled as the worst single. The performance comparison of the linear model using these two sets is made using the validated RMSE. The RMSE for each method was obtained at each sensor and wavelength by summing all the squared residuals between the observations and the fitted values. This summation was then root squared and divided by the corresponding degree of freedom to obtain the RMSE at each sensor and wavelength. The resulting calibration RMSE distributions are shown in figures 28a and 28b for the 960 nm and 1360 nm wavelengths, respectively.

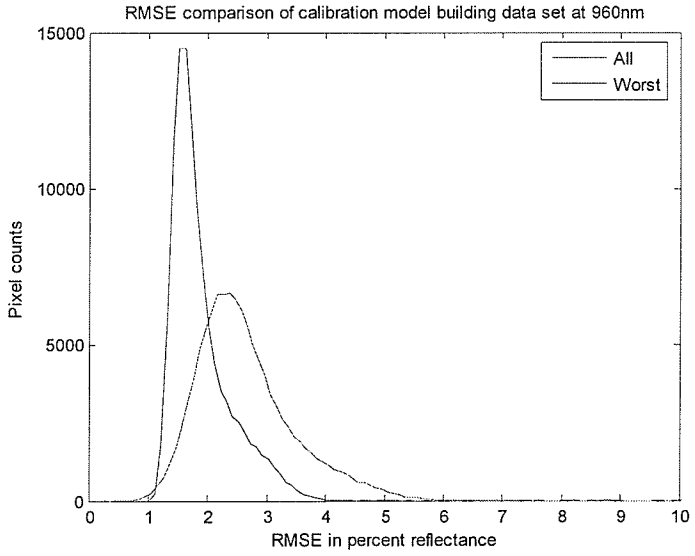

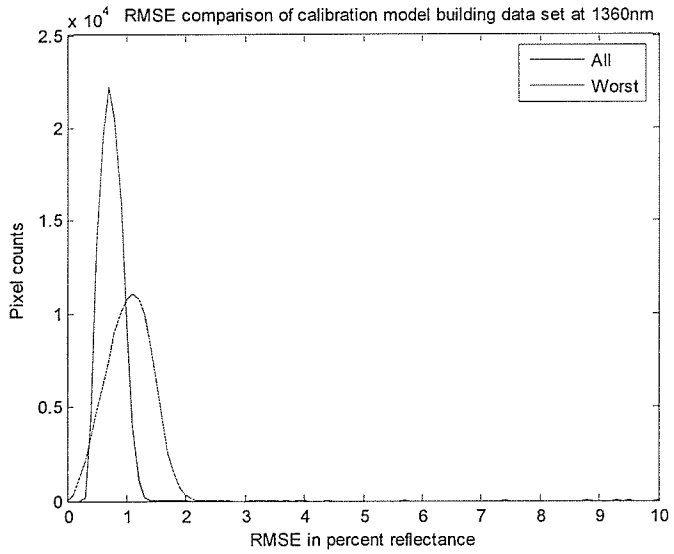

Figure 28: RMSE Histogram comparison a) 960 nm b) 1360 nm

In figure 28a the RMSE corresponding to the full data set building model is lower than the two single sets. Here the differences relative to the RMSE of the full data set model and the singles are approximately of one percent for the worst single. In figure 28b the RMSE corresponding to the full data set is also better than the single. However, the difference is now smaller because the sensitivity at the 1360 nm is greater and noise drifts are smaller.

To show the performance comparison of the two model building reference sets for all wavelengths, the average of the RMSE was used. The average RMSE was obtained by computing the average RMSE over all sensors inside the sensitive region at each individual wavelength. The average RMSE comparison is shown as a function of wavelength in figure 29.

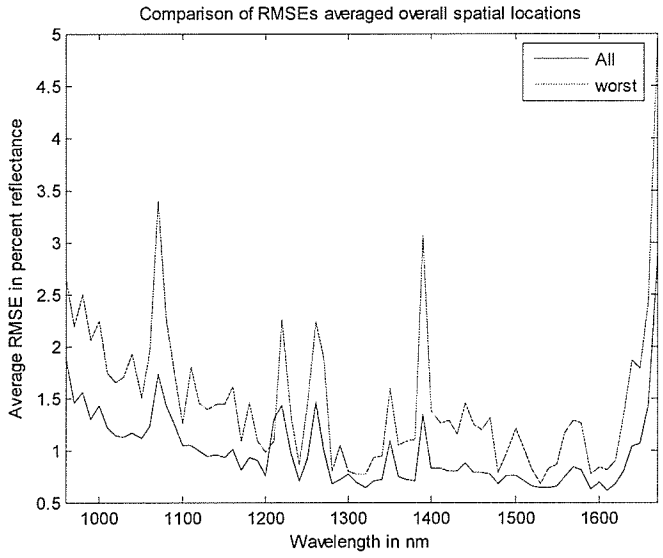

Figure 29: Comparison of mean RMSE as a function of wavelength

Figure 29 shows that the performance of the full reference building model set is better than the worst single at all wavelengths. The performance comparison shown in figures 28 and 29 implies that a better estimate of the coefficients was obtained by using the full set of repeated reference measurements. In the case of the worst single, the noise drift between the fourth and fifth acquisitions is higher than in any other acquisition combination. This results in higher deviations from the fit resulting in a higher RMSE. This set was chosen to show the impact of the building model data set in the accuracy of the model approximation.

This thesis discusses the significance of the results in addressing and correcting some of the issues present in NIR HSI systems. In particular, the problems addressed are defective sensors (saturated or dead), sensors with low sensitivity, spatial and spectral nonuniformities in the system, the time drift and dark current noise in the system and finally sensor calibration. These problems are addressed by constructing a linear model for each

sensor location and wavelength of operation. Defective sensors and sensors with low sensitivity where masked out using a classification based on the slope of the linear model (a parameter like sensitivity). And finally the calibration is addressed using the inverse relationship of the response model (i.e., the linear model).

This chapter we discussed the significance of a higher order model for the response and calibration of the system. It was found that the quadratic model does indeed provide some refinement to the model of just a few sensors within the FPA with the data at hand. However, the approximation resulting from the linear model is sufficient in average for the actual response and calibration functions. Moreover, the linear model is a better estimator when comparing the prediction accuracy of each model (i.e., the linear and quadratic) by means of the PRESS criterion. The reason behind this result is that extrapolation of polynomials of higher degree polynomials causes a larger error when predicting points outside the training set.

Finally, this chapter discusses the issue of using a data set containing information reflecting the spatial and spectral nonuniformity as well as the time drift in the system. In general, this information is helpful in order to obtain more accurate approximations of the actual response and calibration functions. Although, obtaining this large data set is time and space consuming, this thesis suggests that it is a sacrifice worth considering if accurate measures are a priority. Moreover, the procedure described is not intended to be repeated every time the spectra of a sample are collected for analysis. Instead, the full data set can be obtained once the characteristic noise drift and sensor sensitivity changes significantly.

Chapter 6

Conclusion

Near infrared hyperspectral imaging has established as powerful non-destructive tool for the chemical analysis of heterogeneous samples. This tool is capable of analyzing multiple chemical constituents simultaneously without damaging the sample under study. These and other benefits such as the fast acquisition of information from a sample and the feasible cost of the instrumentation have in turn motivated its use in applications such as food and agrochemical quality and safety inspection (Wang and Paliwal 2007), pharmaceutics and medicine (Ciurczak and Drennen 2002), textile production, combustion research, etc.

However, NIR HSI instrumentation is not free from problems. This thesis deals with some of the problems attributed to the illumination source, electronic tunable filters, optics and the FPA in a NIR HSI system. A review of literature revealed that the problems commonly encountered in these types of systems are the spatial non-uniform response of the system, the spectral variance, the time drift in the sensors within the FPA, defective sensors showing saturation or no response at all. The fact that the acquired raw data needs

to be converted into percent reflectance for subsequent chemical analysis poses additional problems.

The methodology used in this thesis for the correction and calibration of NIR HSI is based on image processing. The first step consisted of obtaining twelve repeated HS measurements of a set of five references of known reflectance (i.e., 0, 2, 50, 75 and 99 percent). This data set was then used to establish the input and output relationship of the system and to illustrate the effects of the problems in the resulting HS images. The results showed that the HS images are indeed corrupted by the spatial non-uniformity, the spectral variance, the time drift, the presence of defective sensors in the FPA and the optics of the system. For this reason, a technique that addresses each of the issues as sub-objectives was proposed.

The first sub-objective was addressed by computing linear approximations for each of the sensor's response at a wavelength independently. The advantage of this method is that it allows for correction of spatial non-uniformities and spectral variances automatically. The parameters of the linear model were obtained by setting the problem in terms of matrices and solving the system of equations using the Moore-Penrose pseudoinverse. To validate the model, the prediction ability of the model was verified using a comparison between the PRESS and SSE criterions. The results showed that the PRESS and SSE are relatively close to each other which indicate that the linear model is a good estimator of the system response.

For the second sub-objective, it was found that the parameters obtained from the linear model can be used as descriptors to characterize the response of each sensor at each individual wavelength. Further analyses revealed that the offset parameter contains in-

formation about the dark current noise in each sensor at a specific wavelength. It was also found that this parameter does not change significantly as a function of input reference and operating wavelength. In contrast, the slope parameter changes as a function of input and wavelength. In other words, these parameters contain sufficient information about the sensitivity of the sensor.

The third sub-objective was accomplished by using the slope parameters as features to identify defective sensors and sensors limited by the aperture of the system. Each sensor in the FPA was classified using a k-means algorithm with k=2 into a sensitive region or to an insensitive region. The feature vector for each sensor consisted of a vector containing entries for each slope corresponding to a wavelength. The final result is a mask that can be used to spot the sensors of the system that are not working properly and to mask out the regions of the HS image corresponding to areas in the FOV with insufficient sensitivity.

For the last sub-objective, the calibration of the system was achieved by using the inverse relationship of the system response. To obtain the parameters of the calibration model the same steps for obtaining the response model were followed with the only exception that the error was now minimized in terms of percent reflectance. The performance of the calibration was shown using histograms of the validated RMSE for all sensors and wavelengths. With this sub-objective accomplished the data could be accurately converted to percent reflectance units.

The use of a quadratic model to describe the system response and calibration functions was also explored. It was demonstrated that the second order term of a quadratic model does indeed provide some refinement to the model. However, this refinement is

significant only to a low portion of sensors within the sensitive region of the FPA. Moreover, the validation of this quadratic model presents the problem of extrapolation commonly encountered in higher order models. This problem results in a validation that is not as good as the linear model. In other words, the RMSE corresponding to the linear model is a better estimator of the true standard deviation than the RMSE estimator of the quadratic model.

Finally, a performance comparison of the linear models constructed using two distinct data sets was shown: the first one, our proposed set which includes information about the time drift of the system versus a data set including a single measurement for each of the available references. It was found using the RMSE that the performance of the linear model constructed using our proposed set is much better than the second set mainly because it contains more information to account for the time drift occurring in the system.

This thesis proposes a method for the correction and calibration of NIR HSI systems. In future research, calibration and correction methods that are more efficient in the use of computer memory and computation time are expected. For example, finding correlations between slopes corresponding to distinct wavelengths could aid in reducing the number of slope parameters required for describing the whole wavelength range of the system save computer memory and time. Moreover, we expect on seeing methods using more input references to address the issue of validating higher order models. Finally, we expect future scene based correction and calibration techniques exploring the spatial, spectral and time of acquisition correlations.

Bibliography

Alexay, C. 2008. Working in the infrared bands. *Advanced Imaging Magazine*. February 2008.

Brown P. J. 1993. *Measurement, Regression and Calibration*. Oxford: Clarendon Press.

Baldridge, A. M., S.J. Hook, C.I. Grove and G. Rivera. 2008. The ASTER Spectral Li brary Version 2.0. In press Remote Sensing of Environment.

Ciurczak, E. and J. Drennen. 2002. *Near infrared spectroscopy in pharmaceutical and medical applications*. New York: Marcel-Dekker.

Forrest, S. 1981. Performance of $In_xGa_{1-x}As_yP_{1-y}$ Photodiodes with dark current limited by diffusion, generation recombination, and tunnelling. *IEEE Journal of Quantum Electronics* 17(2): 217-226.

Gat, N. 2000. Imaging spectroscopy using tunable filters: A review. *Proceedings of the SPIE – The International Society for Optical Engineering* vol. 4056: 50-64.

Geladi, P. 2003. Chemometrics in spectroscopy. Part 1. Classical chemometrics. *Spectro-chimica Acta Part B* 58: 767-782.

Geladi, P., J. Burger and T. Lestander. 2004. Hyperspectral Imaging: Calibration prob lems and solutions. *Chemometrics and Intelligent Laboratory Systems* 72: 209-217.

Gonzales, R.C. and R.E. Woods. 2001. *Digital Image Processing* 2nd ed. Upper Saddle River, NJ: Prentice Hall.

Jain, A.K., M.N. Murty and P.J. Flynn. 1999. Data clustering: A review. ACM Computing Surveys 31(3): 264-323.

Kutner, M.H., C.J. Nachtsheim, J. Neter and W. Li. 2005. *Applied Linear Statistical Models* 5th ed. New York, NY: McGraw-Hill/Irwin.

Mark, H. and J. Workman. 2003. *Statistics in spectroscopy* 2nd ed. Amsterdam: Elsevier.

Mark, H. and J. Workman. 2007. *Chemometrics in Spectroscopy*. Oxford, UK: Academic Press.

McClure, W.F. 2001. *Near infrared Technology in the Agricultural and Food industries* 2nd. St. Paul, MN: AACC.

Norton, P. 2003. Detector focal plane array technology. *Encyclopedia of Optical Engineering*. New York, NY: Marcel-Dekker 320 – 348.

Osborne, B.G., T. Fearn and P.H. Hindle. 1993. *Practical NIR Spectroscopy: with Appli cations in Food and Beverage Analysis* 2nd ed. Essex, England: Longman Scientific and Technical.

Olsen, G.H. and V.S. Ban. 1987. InGaAsP: The next generation in Photonics Materials. *Solid State Technology* 30: February,pp 99-105.

O'Shea D.C. 1985. *Elements of Modern Optical Design*. New York: John Wiley & Sons.

Pedrotti, F.L., L.S. Pedrotti and L.M. Pedrotti. 2007. *Introduction to optics*. 3rd ed. Pren tice Hall. Upper Saddle River, NJ.

Perry, D.L. and E.L. Dereniak. 1993. Linear theory of nonuniformity correction in near infrared staring sensors. *Optical Engineering* 32(8): 1854-1859.

Proakis, J.G. and D.G. Manolakis. 2007. *Digital Signal Processing* 4th ed. Upper Saddle River, NJ: Prentice Hall.

Ren, D. 2003. Lens design. *Encyclopedia of Optical Engineering.* New York, NY: Marcel-Dekker 1057 – 1067.

Rogalski, A. 2003. Infrared detectors: status and trends. *Progress in Quantum Electronics* 27: 59-210.

Shaw R.A. and H.H. Mantsch. 1999. Vibrational biospectroscopy: from plants to animals to humans. A historical perspective. *Journal of Molecular Structure* 480-481: 1-13.

Schowengerdt, R.A. 1997. *Remote Sensing Models and Methods for Image Processing.* 2nd ed. San Diego: Academic press.

Schulz, M. And L. Caldwell. 1995. Nonuniformity correction and correctability of infrared focal plane arrays. *Infrared Physics and Technology* 36: 763-777.

Torres, S.N and M.M. Hayat. 2003. Kalman filtering for adaptive nonuniformity correction in infrared focal-plane arrays. *Journal of Optical Society of America A* 20(3): 470-480.

Wang, W. and J. Paliwal. 2007. Near infrared spectroscopy and imaging in food quality and safety. *Sensing and Instrumentation for Food Quality and Safety* 1: 193-207.

Wilson, A. 2005. IR lenses maximize detector potential. *Vision System Design Magazine*. May 2005.

Appendix A

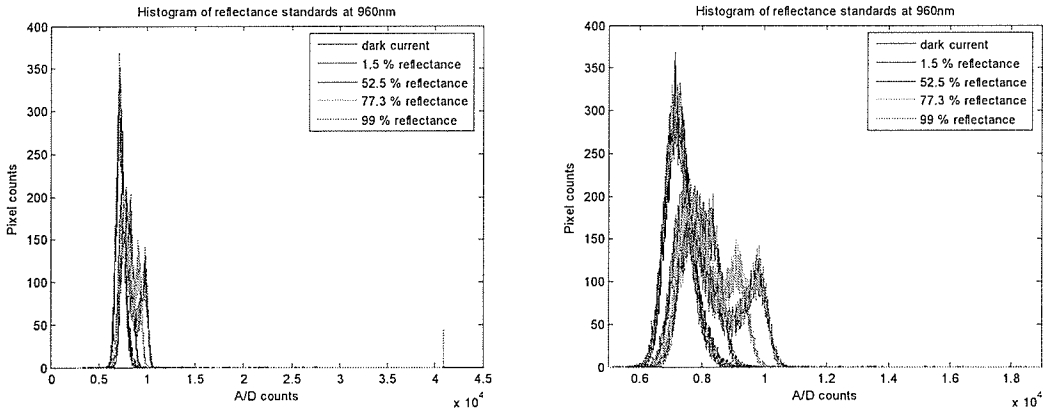

Figure A. 1: Spatial response variation at 960 nm a) Histogram, b) Zoomed histogram

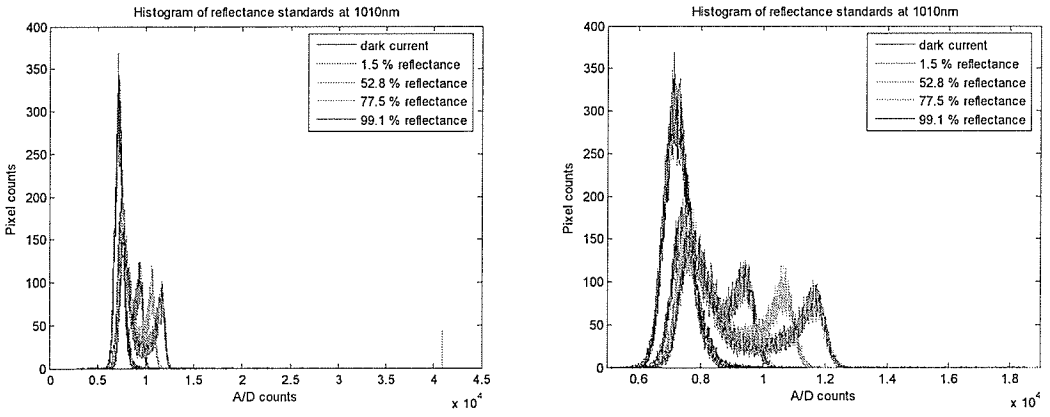

Figure A. 2: Spatial response variation at 1010 nm a) Histogram, b) Zoomed histogram

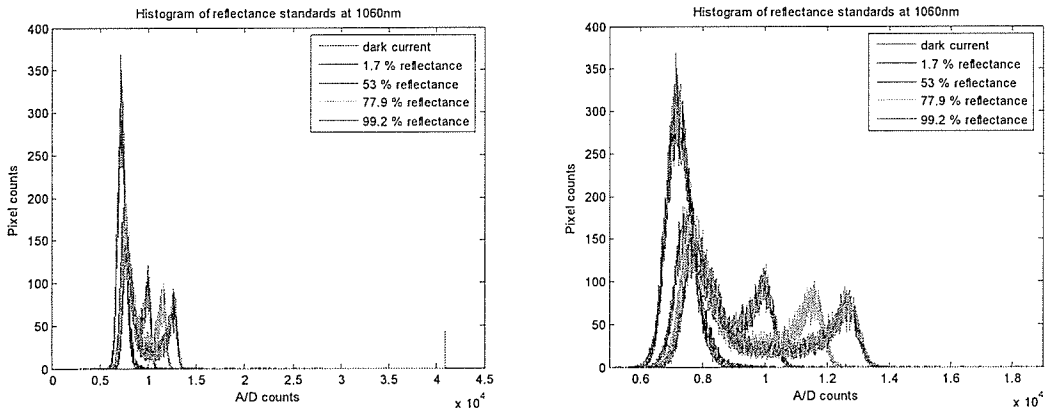

Figure A. 3: Spatial response variation at 1060 nm a) Histogram, b) Zoomed histogram

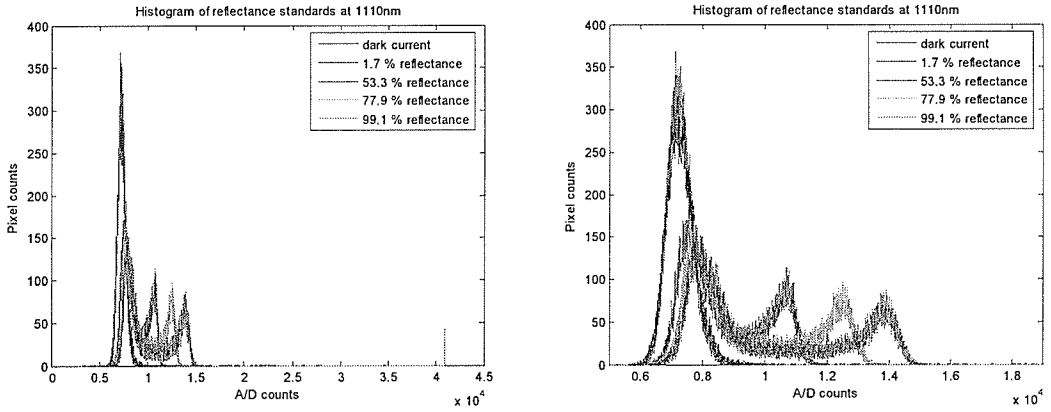

Figure A. 4: Spatial response variation at 1110 nm a) Histogram, b) Zoomed histogram

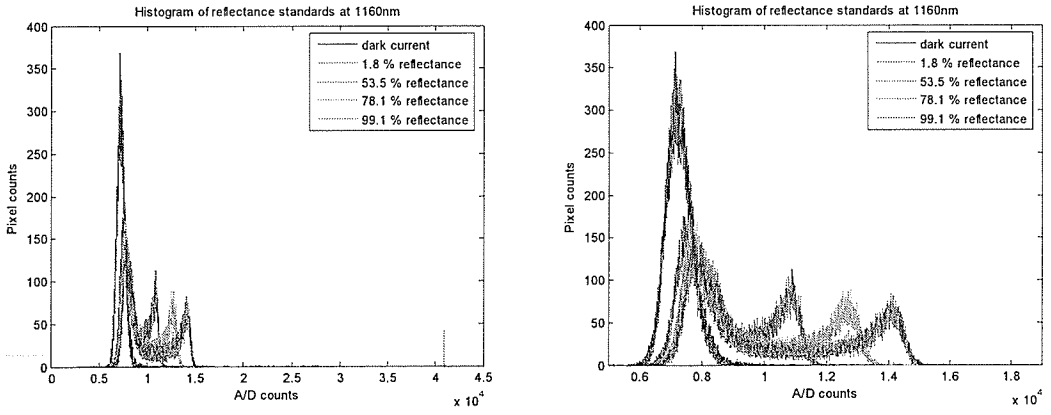

Figure A. 5: Spatial response variation at 1160 nm a) Histogram, b) Zoomed histogram

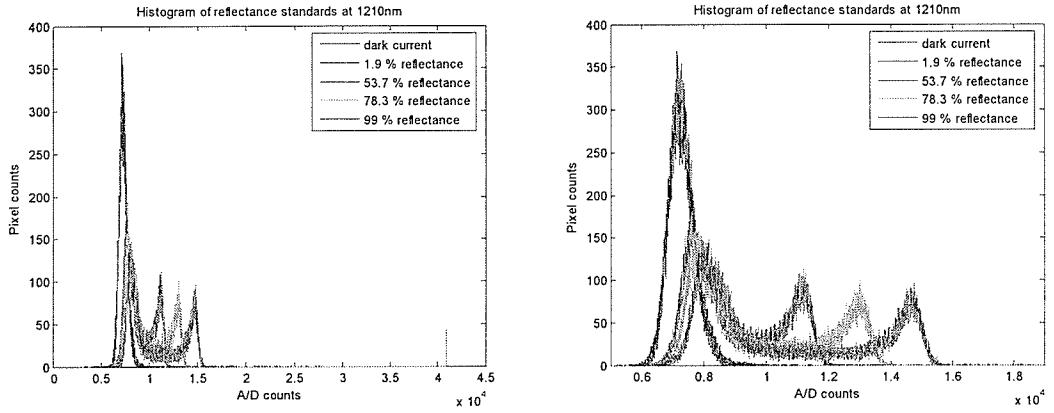

Figure A. 6: Spatial response variation at 1210 nm a) Histogram, b) Zoomed histogram

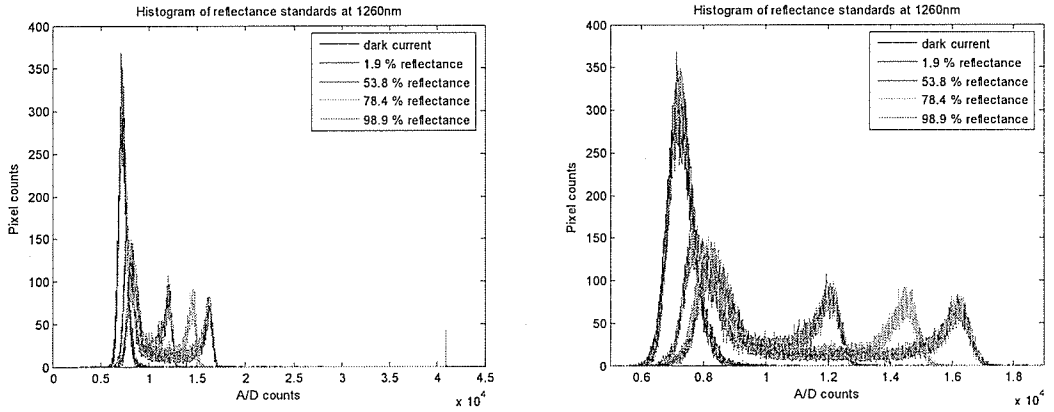

Figure A. 7: Spatial response variation at 1260 nm a) Histogram, b) Zoomed histogram

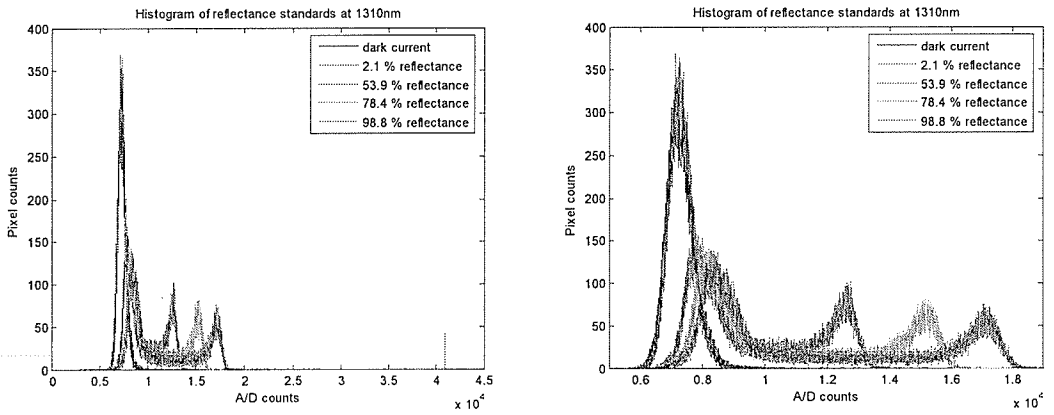

Figure A. 8: Spatial response variation at 1310 nm a) Histogram, b) Zoomed histogram

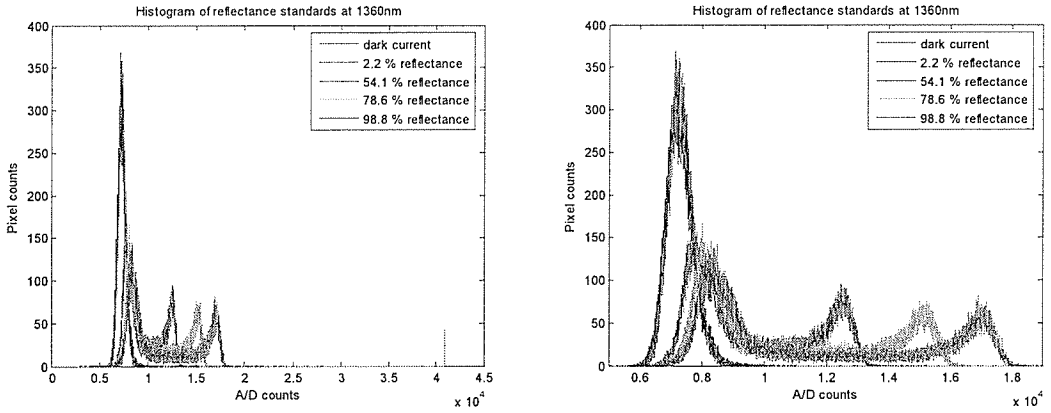

Figure A. 9: Spatial response variation at 1360 nm a) Histogram, b) Zoomed histogram

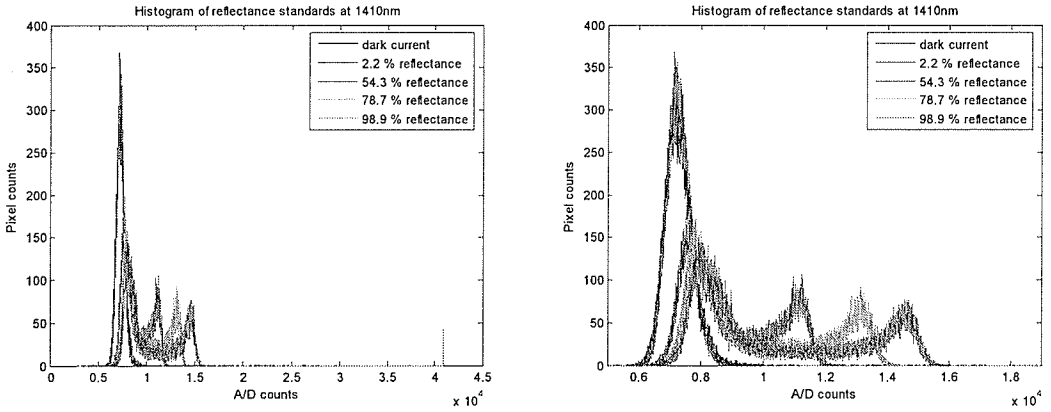

Figure A. 10: Spatial response variation at 1410 nm a) Histogram, b) Zoomed histogram

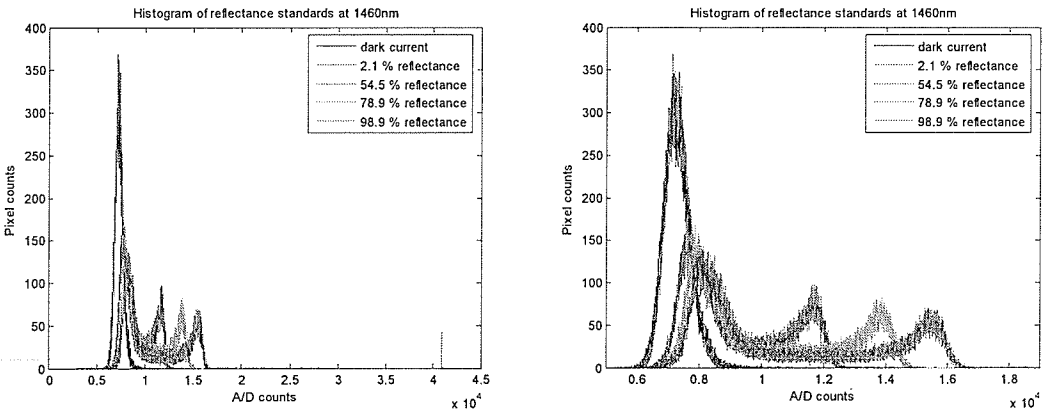

Figure A. 11: Spatial response variation at 1460 nm a) Histogram, b) Zoomed histogram

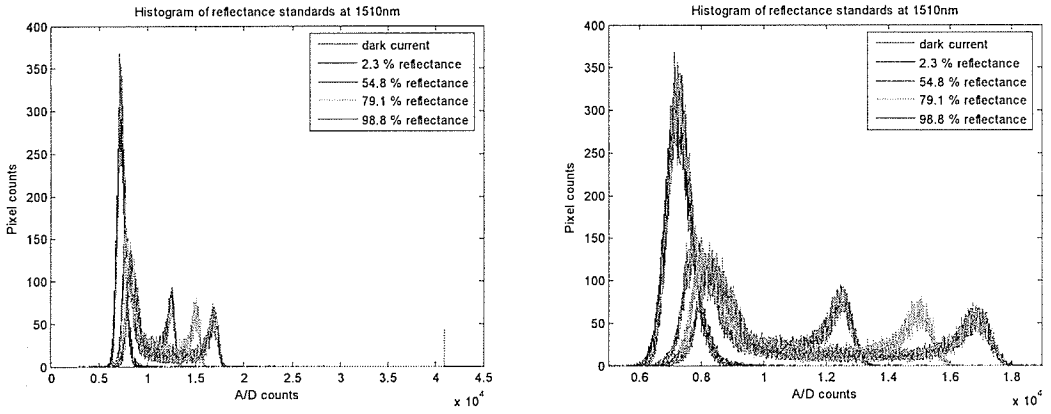

Figure A. 12: Spatial response variation at 1510 nm a) Histogram, b) Zoomed histogram

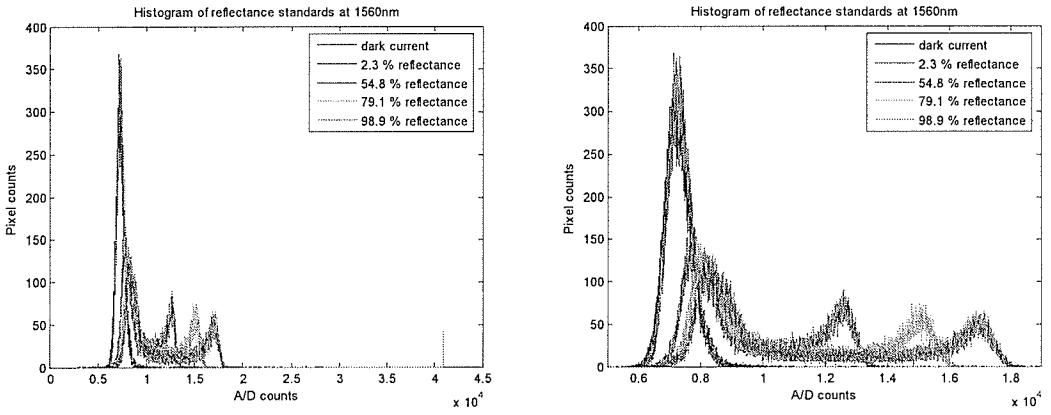

Figure A. 13: Spatial response variation at 1560 nm a) Histogram, b) Zoomed histogram

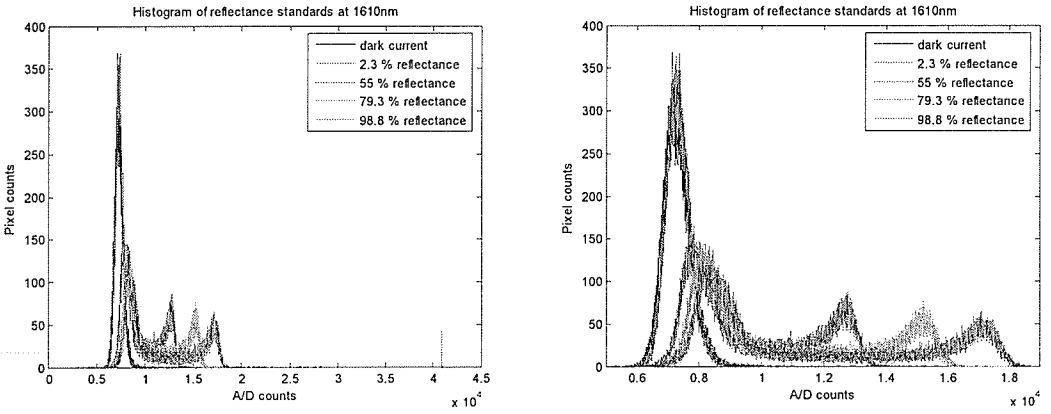

Figure A. 14: Spatial response variation at 1610 nm a) Histogram, b) Zoomed histogram

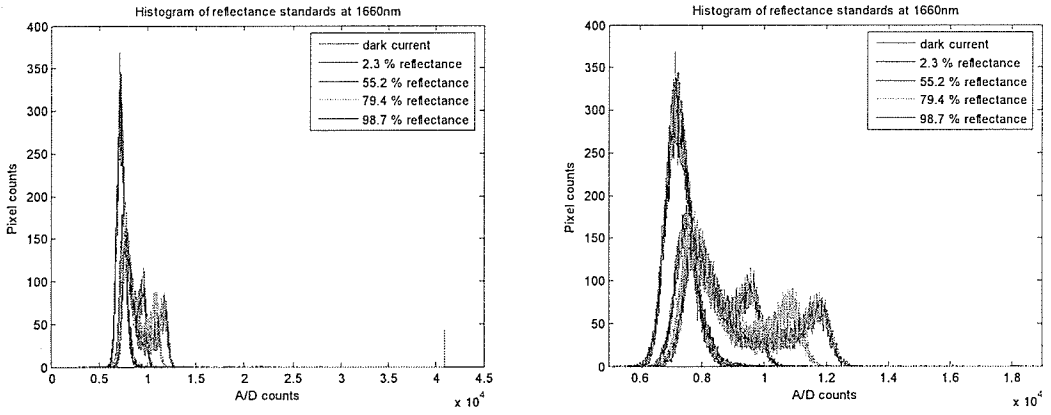

Figure A. 15: Spatial response variation at 1660 nm a) Histogram, b) Zoomed histogram

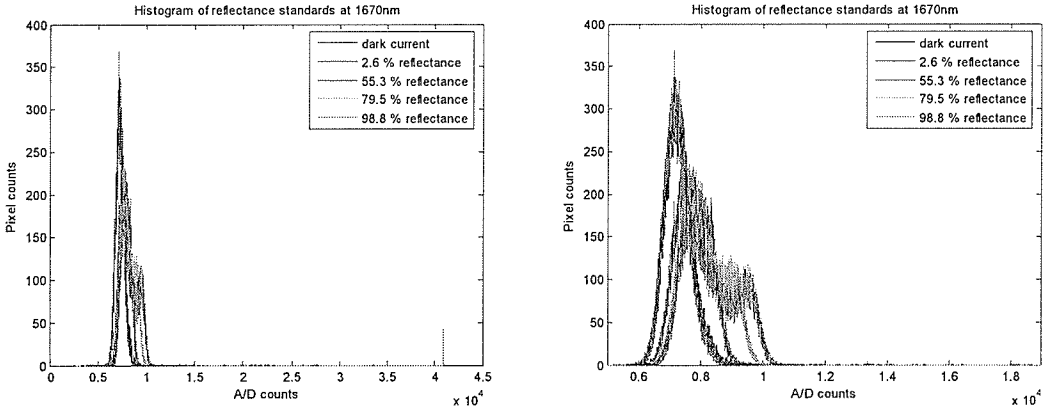

Figure A. 16: Spatial response variation at 1670 nm a) Histogram, b) Zoomed histogram

Note: In figures A17-34 graphs in black, yellow, green, red and blue correspond to the dark current, 2, 50, 75 and 99 percent references, respectively.

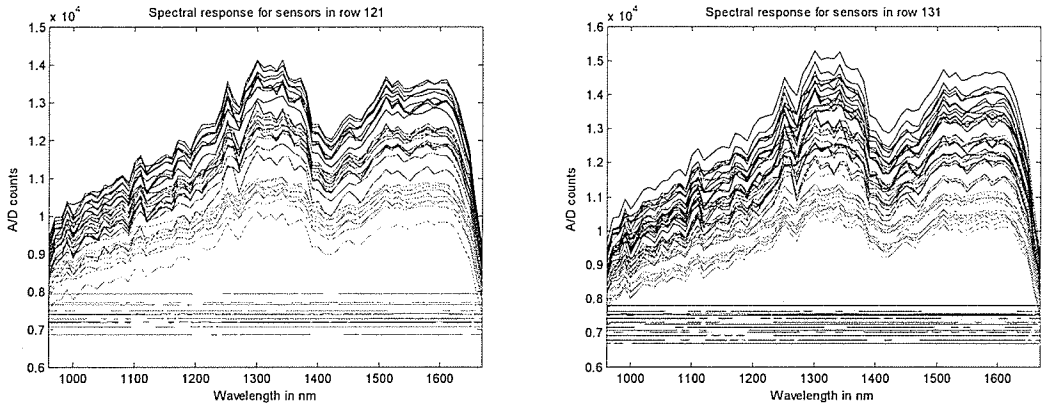

Figure A. 17: Spectral response of sensors at a) Row 121, b) Row 131

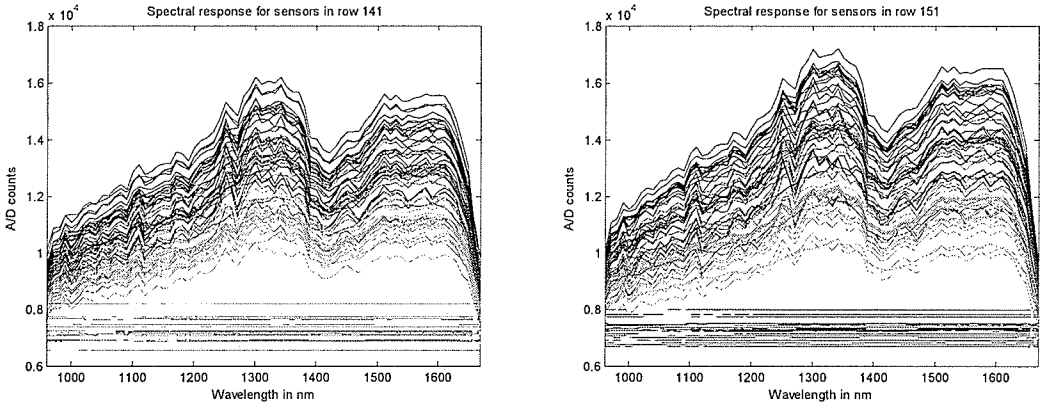

Figure A. 18: Spectral response of sensors at a) Row 141, b) Row 151

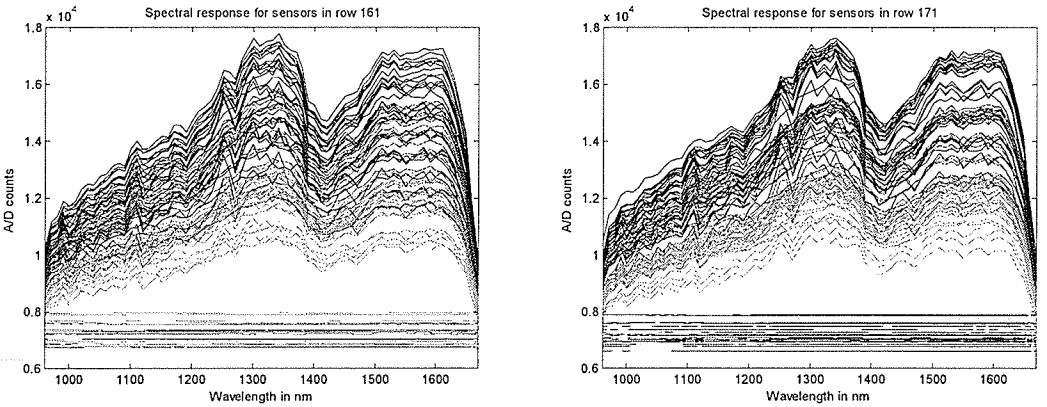

Figure A. 19: Spectral response of sensors at a) Row 161, b) Row 171

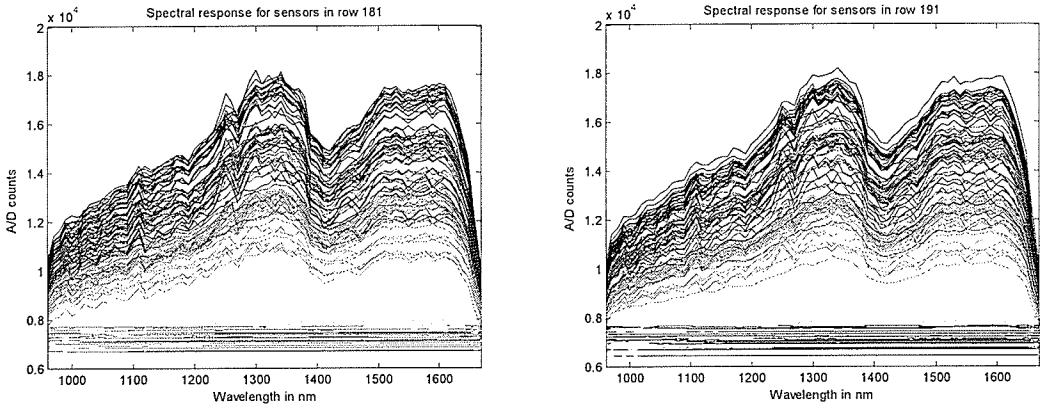

Figure A. 20: Spectral response of sensors at a) Row 181, b) Row 191

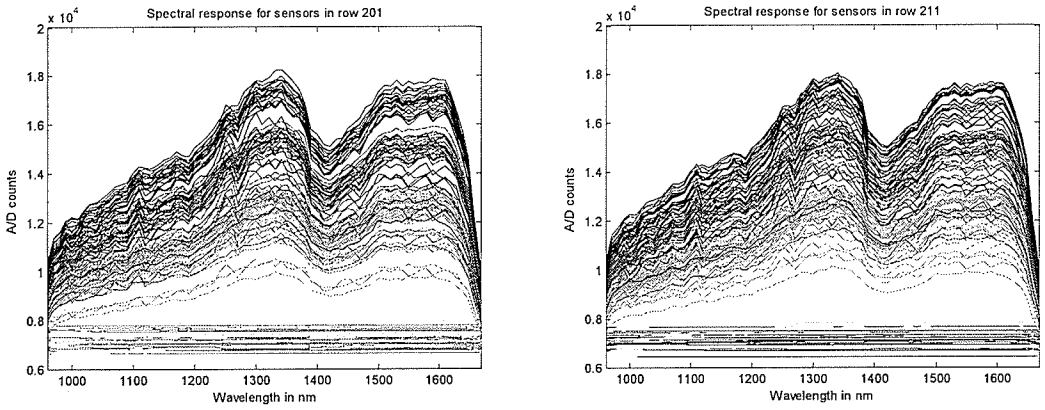

Figure A. 21: Spectral response of sensors at a) Row 201, b) Row 211

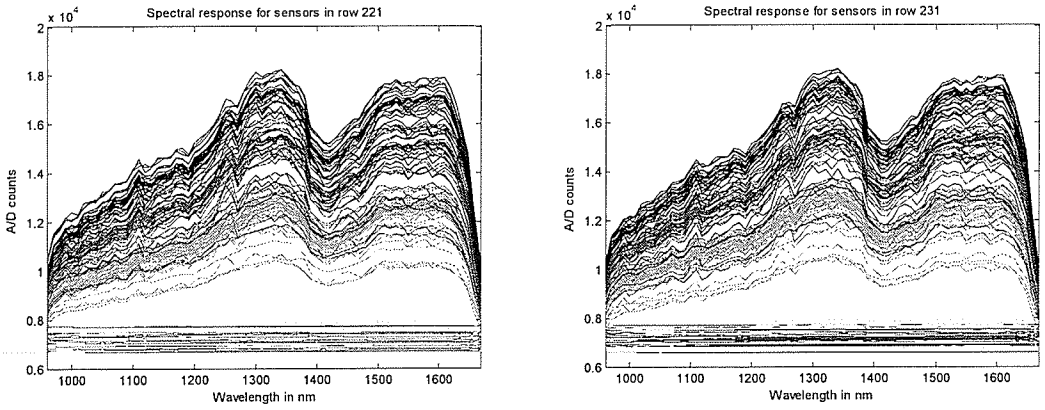

Figure A. 22: Spectral response of sensors at a) Row 221, b) Row 231

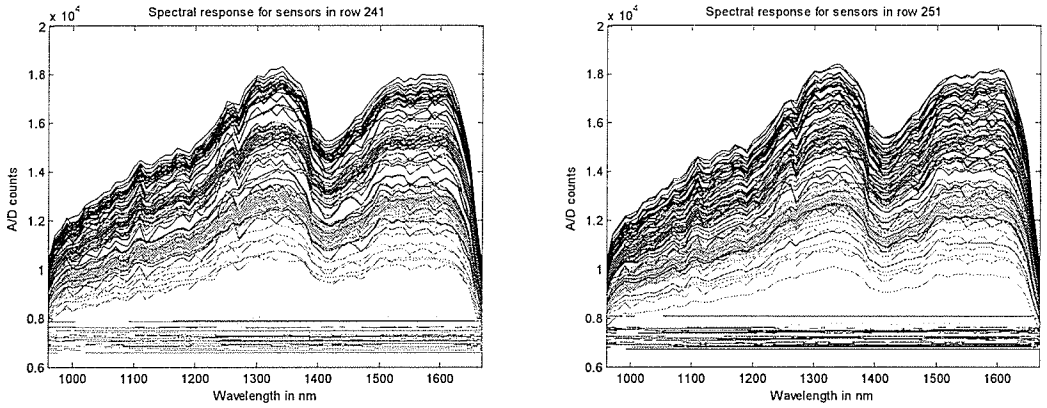

Figure A. 23: Spectral response of sensors at a) Row 241, b) Row 251

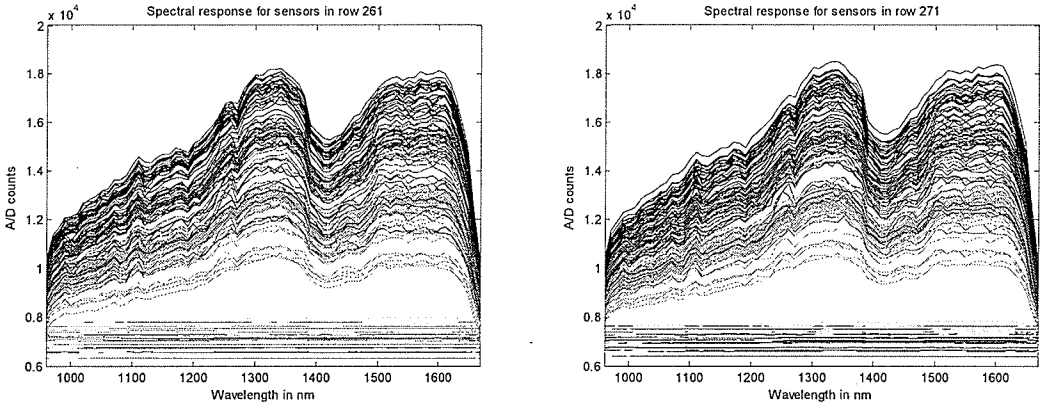

Figure A. 24: Spectral response of sensors at a) Row 261, b) Row 271

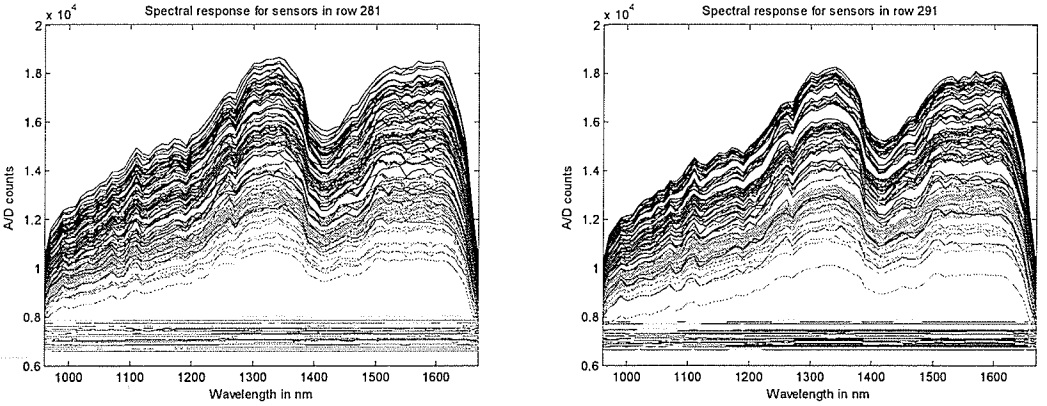

Figure A. 25: Spectral response of sensors at a) Row 281, b) Row 291

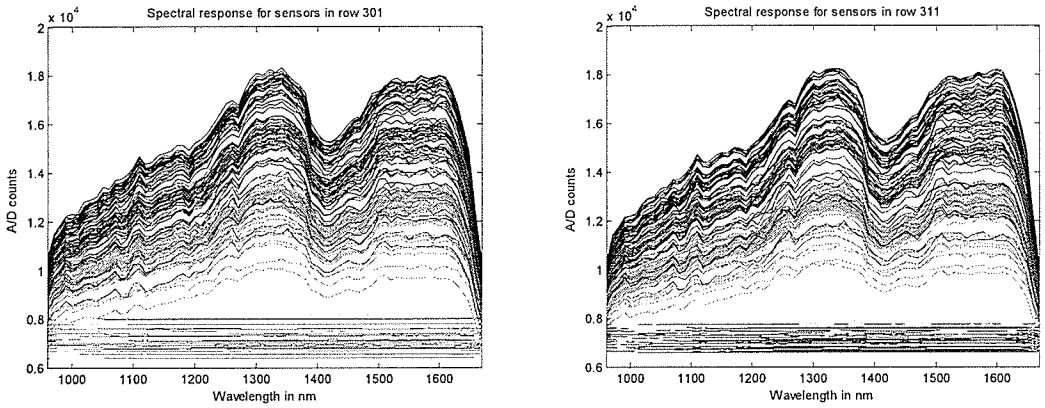

Figure A. 26: Spectral response of sensors at a) Row 301, b) Row 311

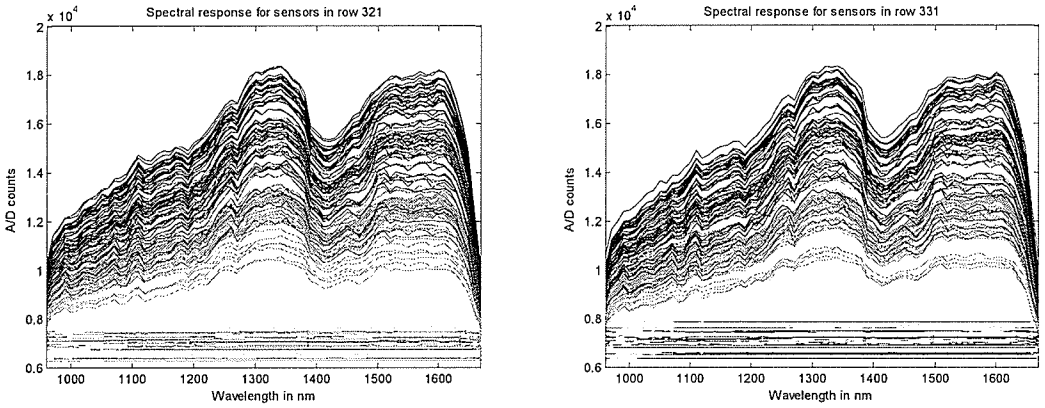

Figure A. 27: Spectral response of sensors at a) Row 321, b) Row 331

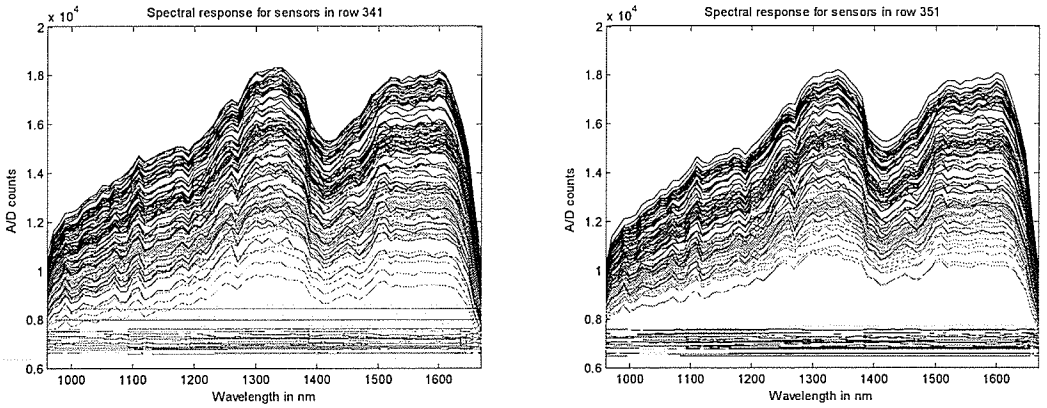

Figure A. 28: Spectral response of sensors at a) Row 341, b) Row 351

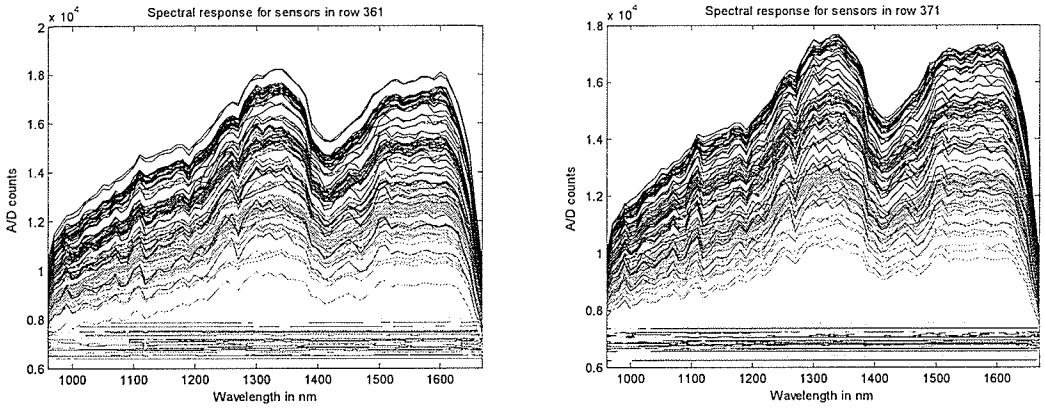

Figure A. 29: Spectral response of sensors at a) Row 361, b) Row 371

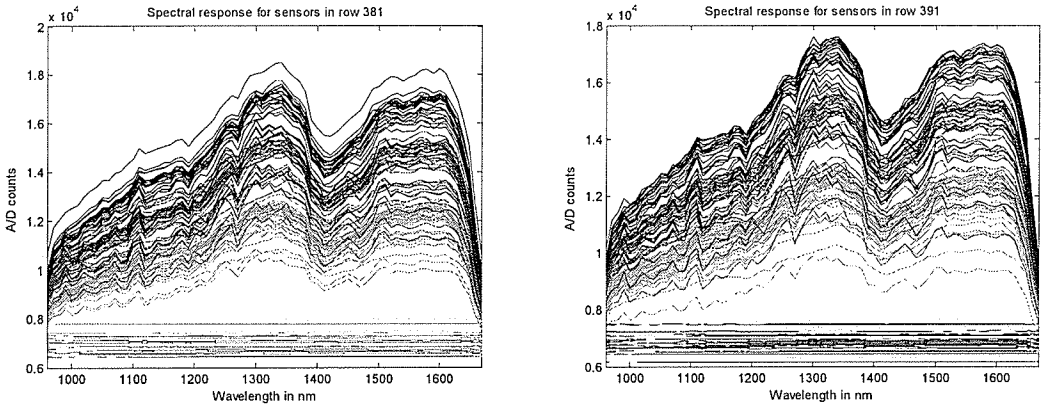

Figure A. 30: Spectral response of sensors at a) Row 381, b) Row 391

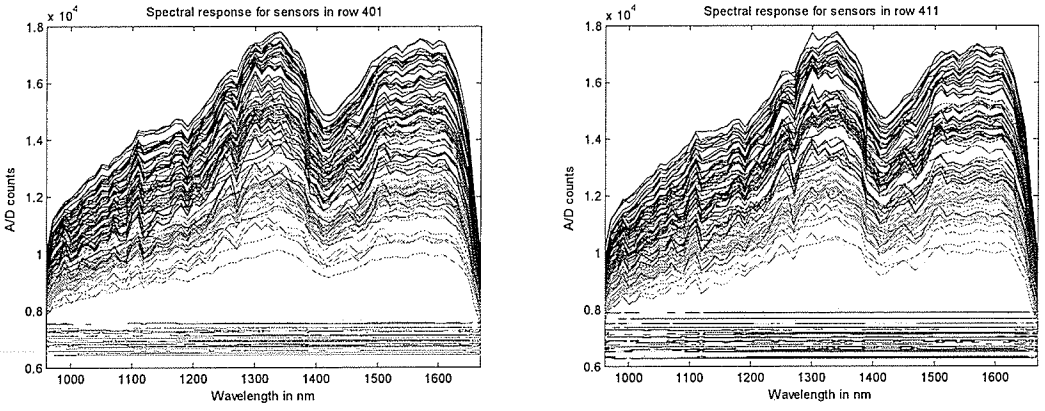

Figure A. 31: Spectral response of sensors at a) Row 401, b) Row 411

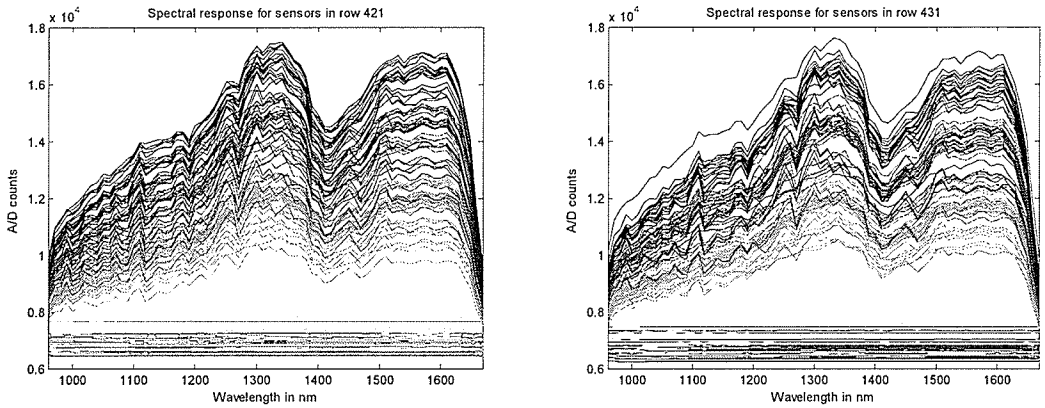

Figure A. 32: Spectral response of sensors at a) Row 421, b) Row 431

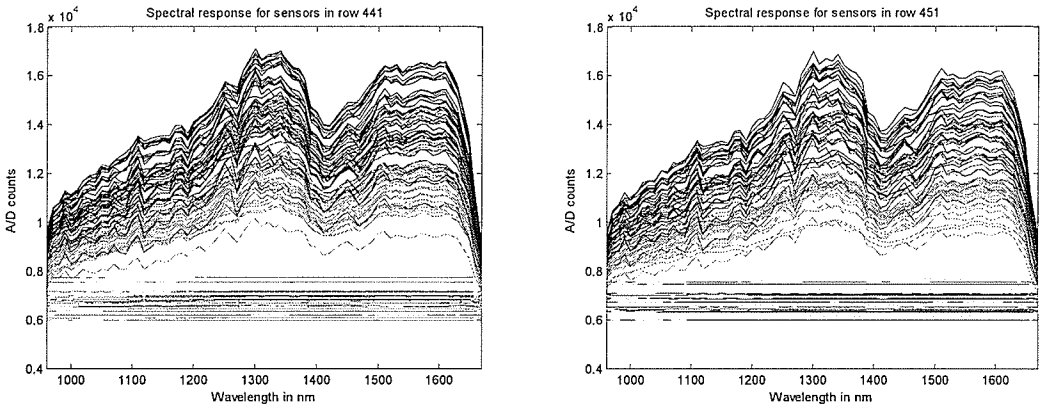

Figure A. 33: Spectral response of sensors at a) Row 441, b) Row 451

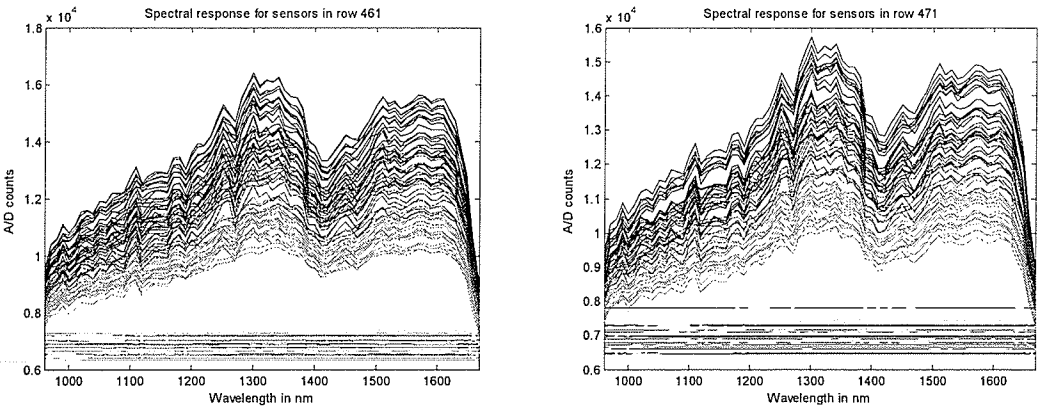

Figure A. 34: Spectral response of sensors at a) Row 461, b) Row 471

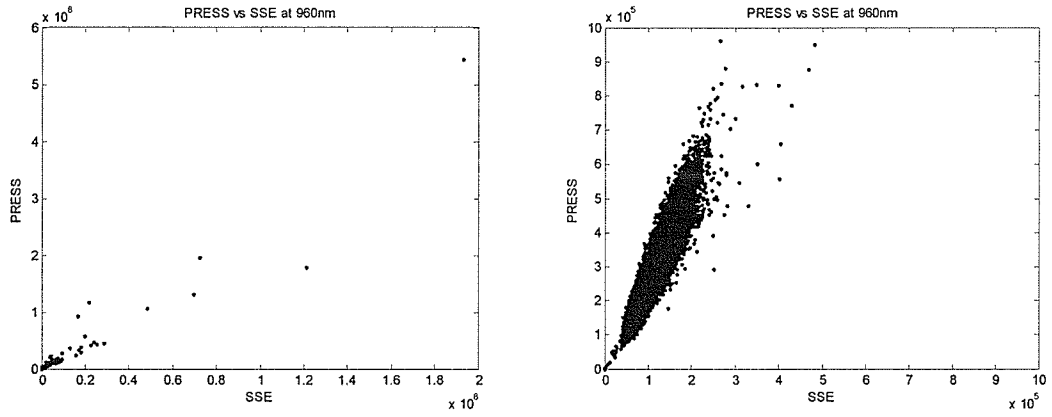

Figure A. 35: SSE vs. PRESS at the 960 nm wavelength a) Full domain and range b) Zoomed plot

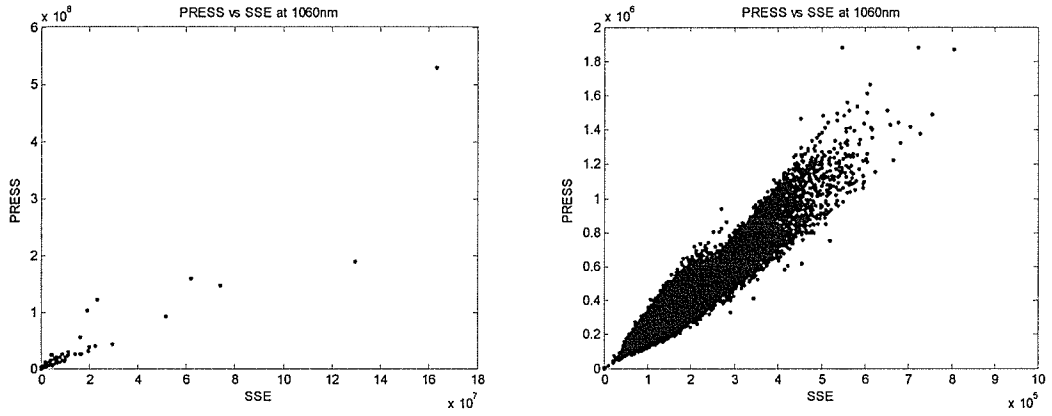

Figure A. 36: SSE vs. PRESS at the 1060 nm wavelength a) Full domain and range b) Zoomed plot

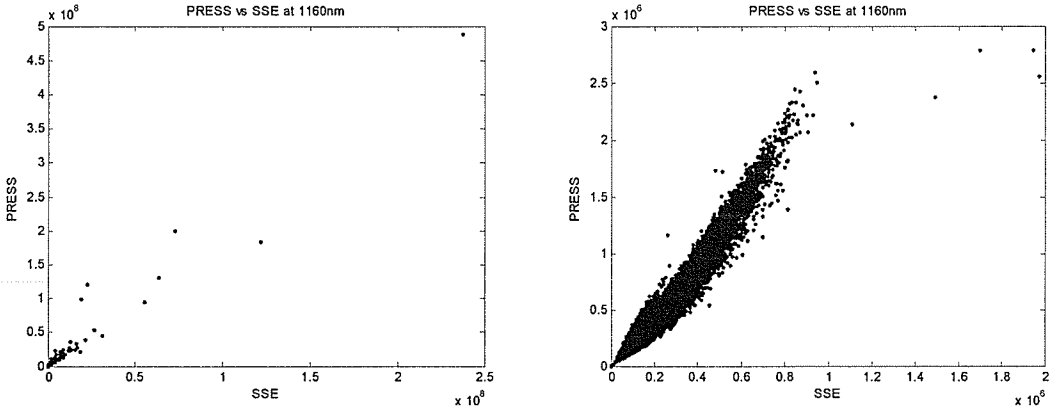

Figure A. 37: SSE vs. PRESS at the 1160 nm wavelength a) Full domain and range b) Zoomed plot

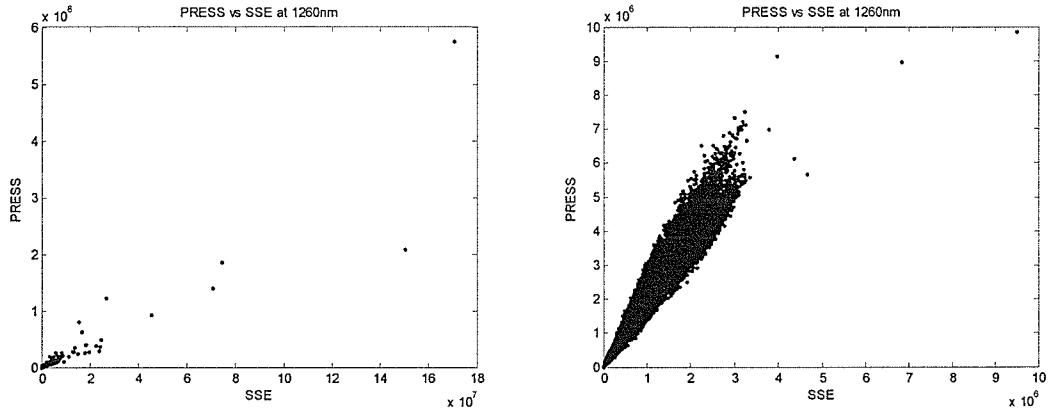

Figure A. 38: SSE vs. PRESS at the 1260 nm wavelength a) Full domain and range b) Zoomed plot

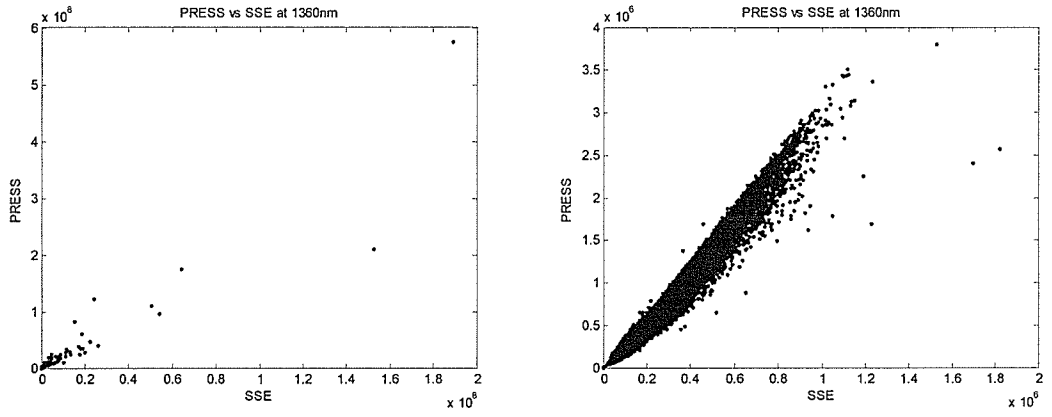

Figure A. 39: SSE vs. PRESS at the 1360 nm wavelength a) Full domain and range b) Zoomed plot

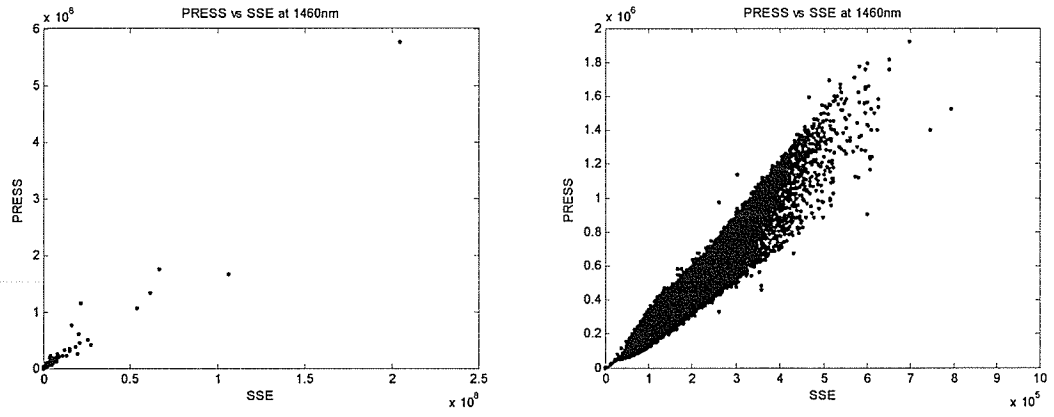

Figure A. 40: SSE vs. PRESS at the 1460 nm wavelength a) Full domain and range b) Zoomed plot

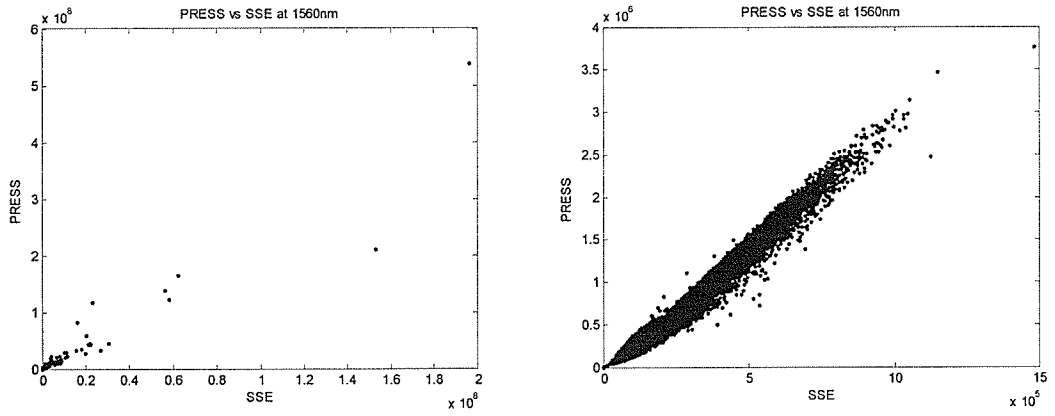

Figure A. 41: SSE vs. PRESS at the 1560 nm wavelength a) Full domain and range b) Zoomed plot

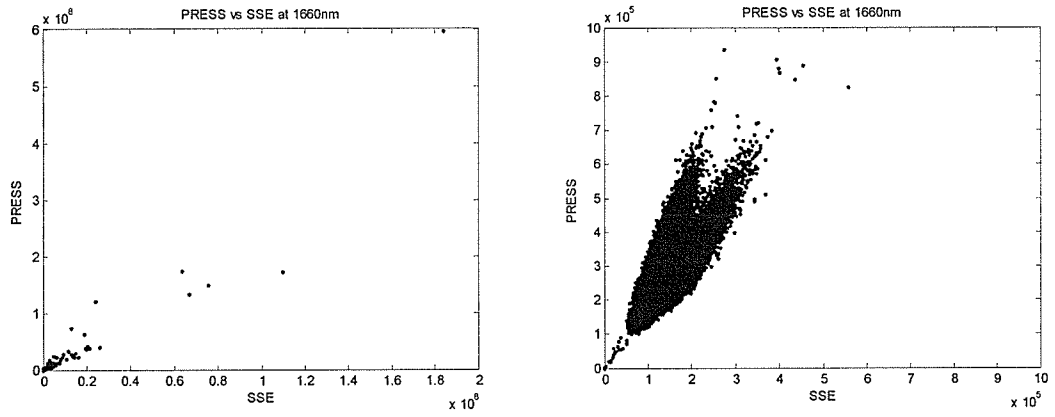

Figure A. 42: SSE vs. PRESS at the 1660 nm wavelength a) Full domain and range b) Zoomed plot

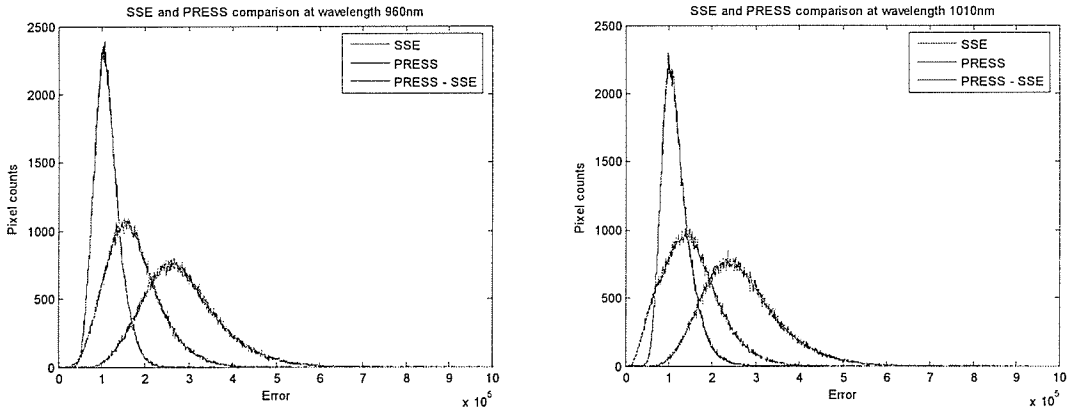

Figure A. 43: SSE and PRESS comparison a) 960 nm b) 1010 nm

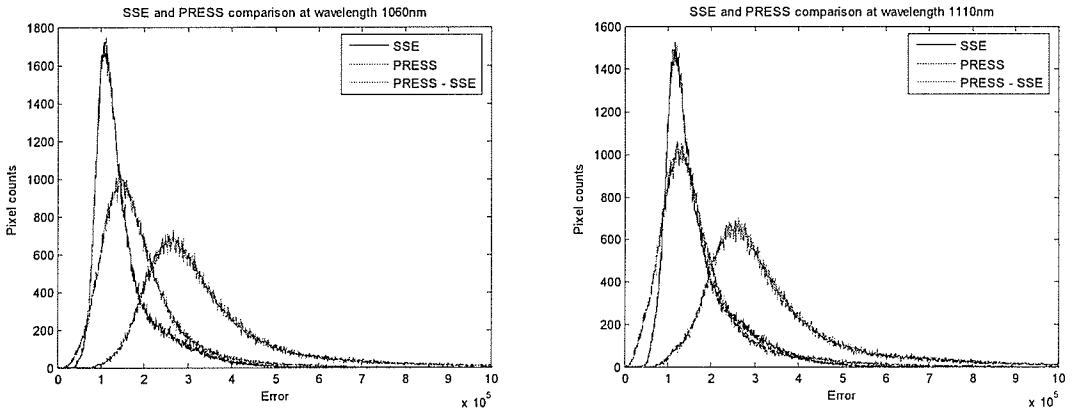

Figure A. 44: SSE and PRESS comparison a) 1060 nm b) 1110 nm

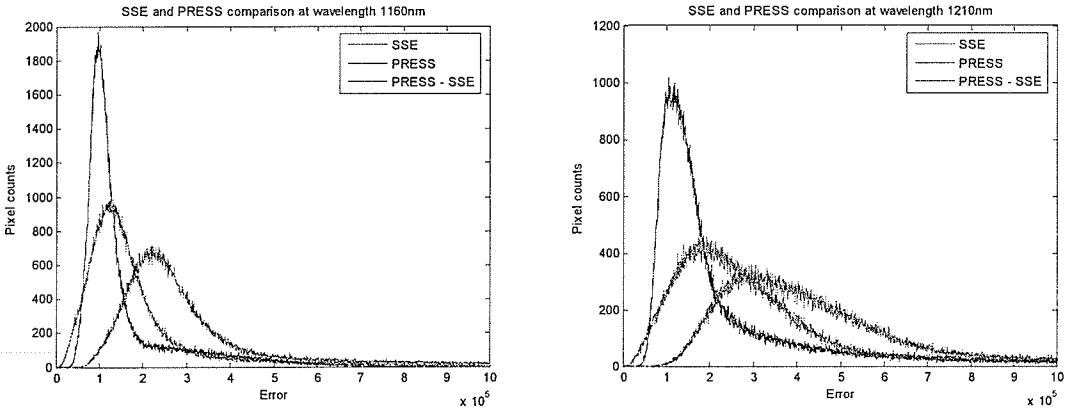

Figure A. 45: SSE and PRESS comparison a) 1160 nm b) 1210 nm

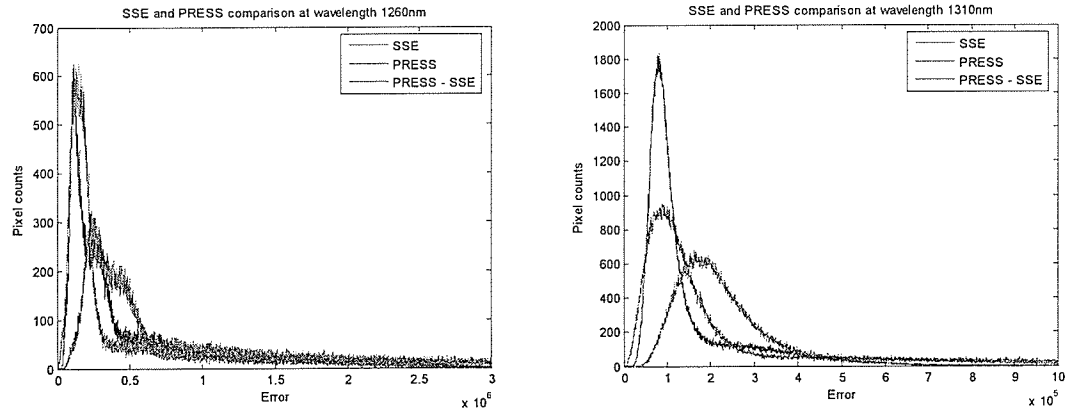

Figure A. 46: SSE and PRESS comparison a) 1260 nm b) 1310 nm

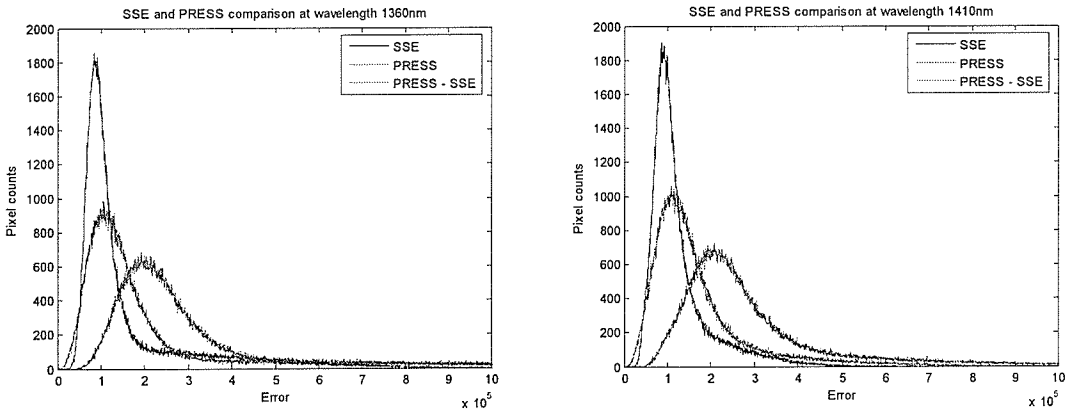

Figure A. 47: SSE and PRESS comparison a) 1360 nm b) 1410 nm

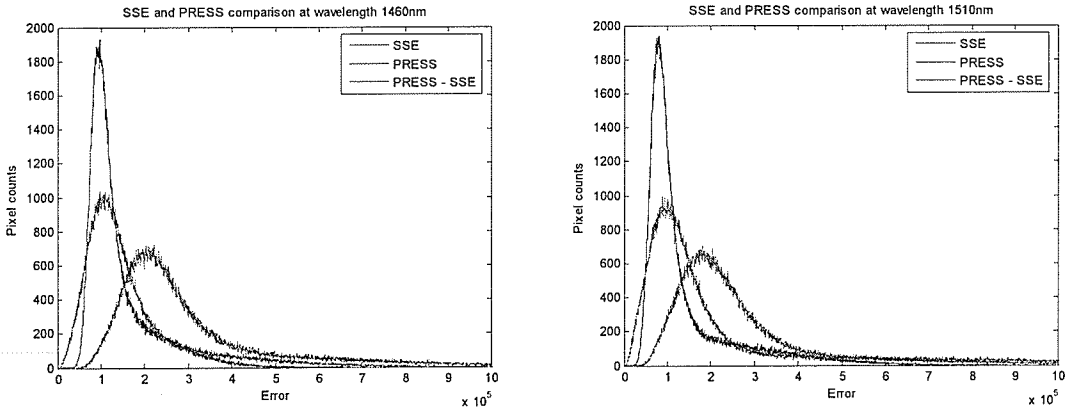

Figure A. 48: SSE and PRESS comparison a) 1460 nm b) 1510 nm

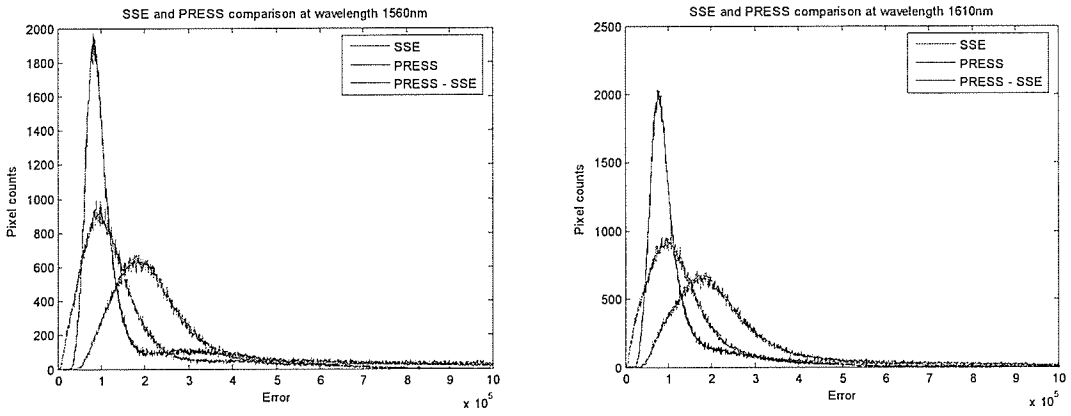

Figure A. 49: SSE and PRESS comparison a) 1560 nm b) 1610 nm

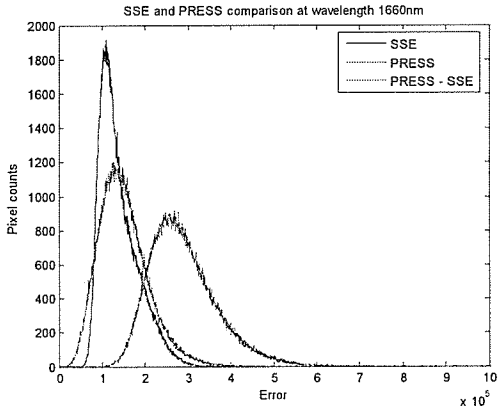

Figure A. 50: SSE and PRESS comparison at 1660 nm

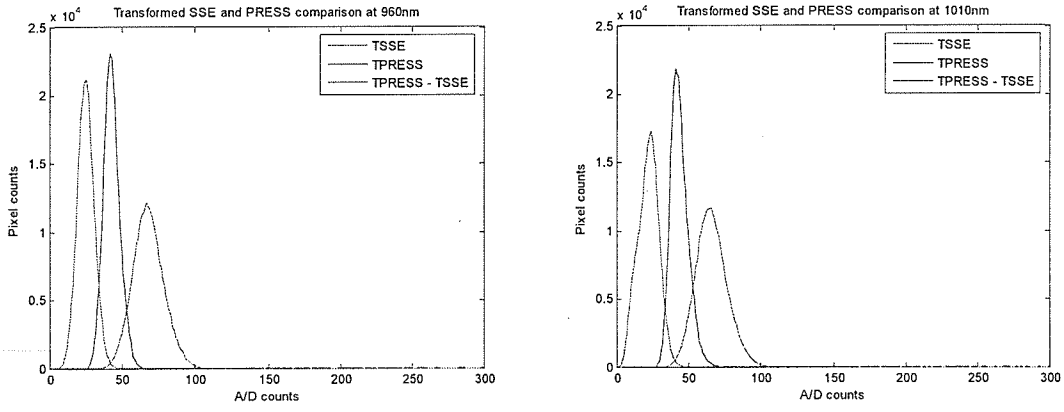

Figure A. 51: Transformed SSE and PRESS comparison a) 960 nm b) 1010 nm

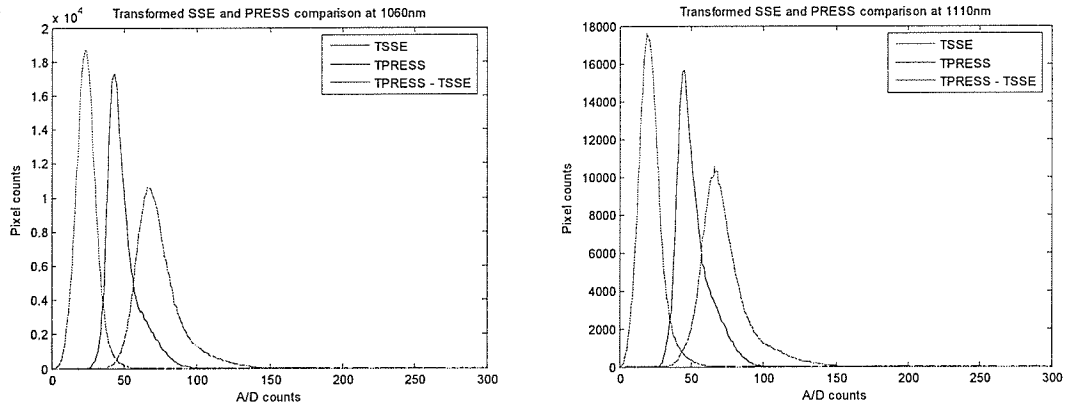

Figure A. 52: Transformed SSE and PRESS comparison a) 1060 nm b) 1110 nm

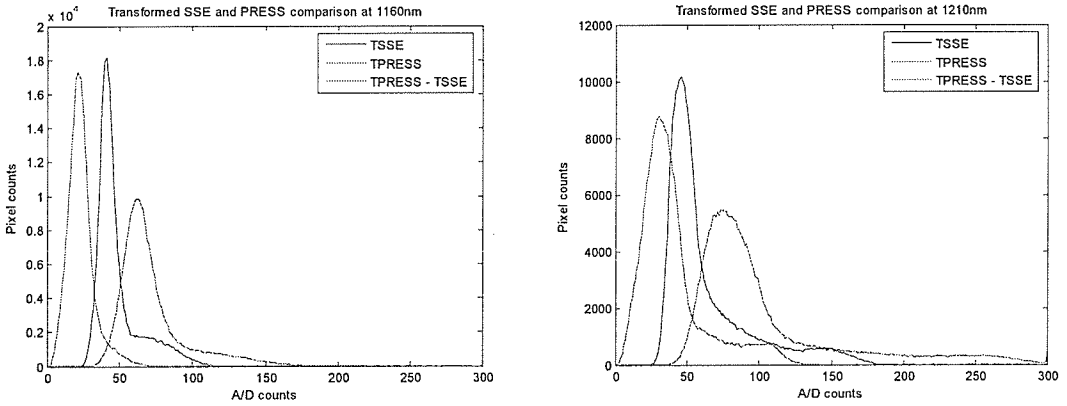

Figure A. 53: Transformed SSE and PRESS comparison a) 1160 nm b) 1210 nm

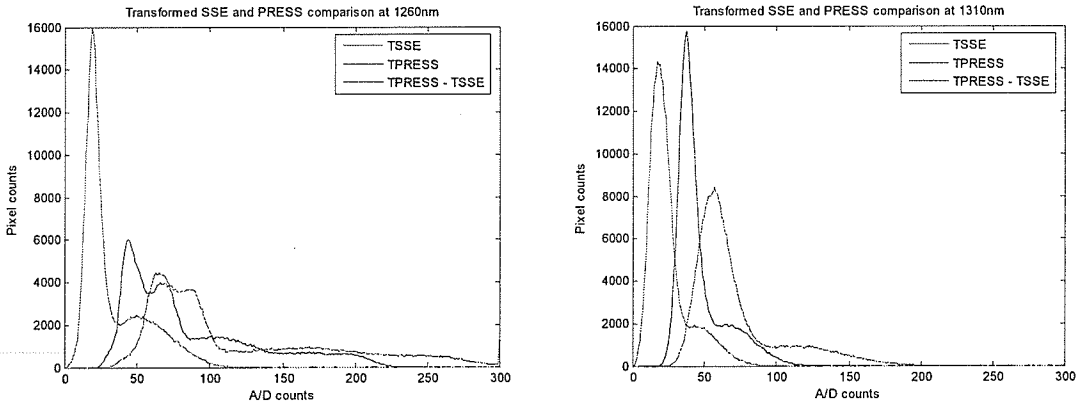

Figure A. 54: Transformed SSE and PRESS comparison a) 1260 nm b) 1310 nm

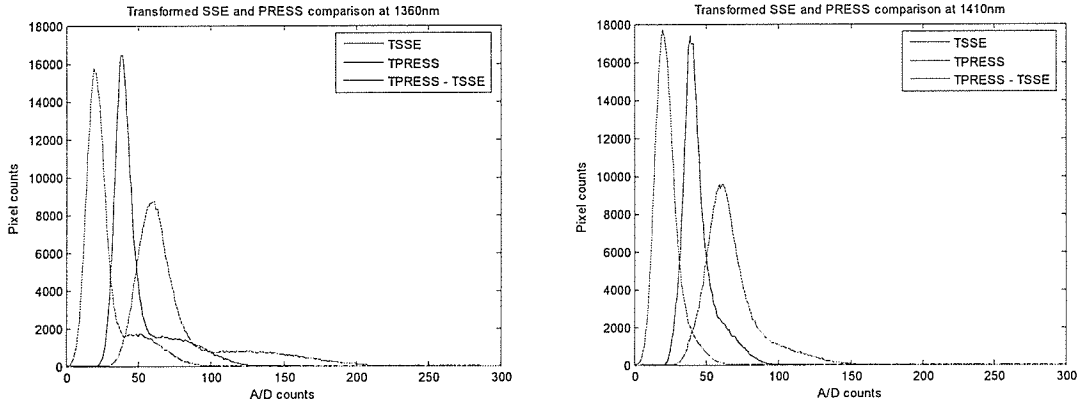

Figure A. 55: Transformed SSE and PRESS comparison a) 1360 nm b) 1410 nm

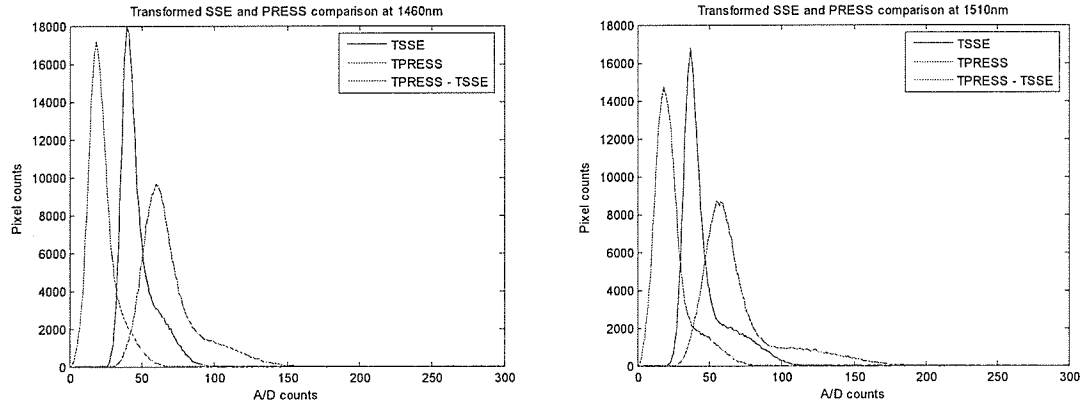

Figure A. 56: Transformed SSE and PRESS comparison a) 1460 nm b) 1510 nm

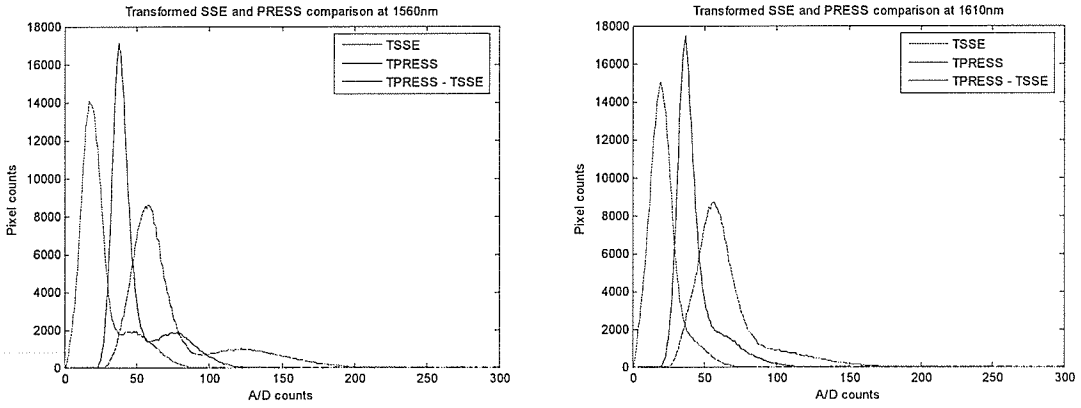

Figure A. 57: Transformed SSE and PRESS comparison a) 1560 nm b) 1610 nm

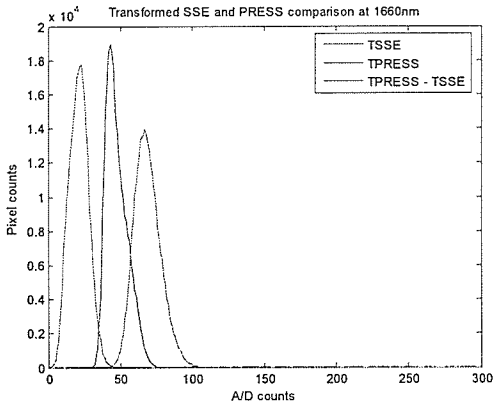

Figure A. 58: Transformed SSE and PRESS comparison at 1660 nm